Prepared for:

DG Rijkswaterstaat

Rijksinstituut voor Kust en Zee/RIKZ

Numerical simulation of wave-current driven sand transport

Theoretical background of the beta-release of the POINT-SAND MODEL

Report

November 1999

WL | delft hydraulics

Z2733.41

Numerical simulation of wave-current driven sand transport

Theoretical background of the beta-release of the POINT-SAND MODEL

Rob Uittenbogaard
Judith Bosboom
Thijs van Kessel

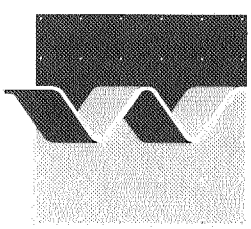

WL | delft hydraulics

WL | delft hydraulics

CLIENT:	DG Rijkswaterstaat Rijksinstituut voor Kust en Zee/RIKZ Kortenaerkade 1 2500 EX Den Haag
TITLE:	Numerical simulation of wave-current driven sand transport Theoretical background of the point sand beta-release

ABSTRACT:

This report describes the theoretical background of the beta-release of the POINT-SAND model an extended version of the Directional Point Model (DPM) that solves the horizontal velocity vector as a function of depth for free-surface flows. The purpose of the extension concerns mainly the inclusion of orbital motions for simulating more aspects of wave-current interaction (WCI), streaming, wave-turbulence interaction, all this in the context of simulating suspended sand transport under sheet-flow conditions. The flow along the entire water depth is simulated for a correct estimation of WCI. The selection of a non-equidistant vertical grid, however, allows for resolving details of the wave boundary layer. The most far-reaching changes to the model structure result from taking into account the non-linear convective terms in momentum equations for the orbital velocity vector and the consistent coupling with a sand transport module. In order to establish this, two time loops are made, an *inner intra-wave time loop* and and *outer wave-averaged time loop*. A major assumption underlying the model is the assumption of spatially periodic wave motions. The latter assumption excludes sloping beds and strong decay or growth of wave properties. In principle, each harmonic component of a multi-directional wave spectrum is simulated although simulating many harmonics reduces the computation speed proportionally. The loading of the flow with suspended sediment is considered to yield damping of turbulence equivalent to salt-stratified or thermally-stratified flows.

The extended model described in this report can be found on the accompanying floppy disc. This beta-release, in combination with the present report serving as a theoretical reference document, is thought to provide a concrete basis for further discussion and development on a multitude of aspects ranging from process description, numerical treatment and model structure to in- and output requirements. It therewith aims at putting an important step forward in the process-based descriptions of sediment transport.

REFERENCES: Contract RIKZ-725 RIKZ/OS 996415
SEDMOC MAS3-CT97-0115

VER.	ORIGINATOR	DATE	REMARKS	REVIEW	APPROVED BY
1	J. Bosboom	5-11-1999		M.J.F Stive	T. Schilperoort

PROJECT IDENTIFICATION:	Z2733.41							
KEYWORDS:	Numerical simulation/Wave-current interaction/Sand transport/DV models							
CONTENTS:	TEXT PAGES	49	TABLES	3	FIGURES	20	APPENDICES	4
STATUS:	☐ PRELIMINARY		☐ DRAFT		☒ FINAL			

Contents

1 Introduction

1.1 Aim and scope of present study

1DV unsteady models resolve the time- and depth-dependency of the velocity and concentration fields. The development and refinement of 1DV unsteady models provides us with further information about the complex processes of sediment suspension enabling a further improvement of engineering transport models. As such the 1DV unsteady models not only increase our knowledge about the sediment transport processes but provide us with a way of improving transport descriptions in morphological models by: 1) parameterization of the unsteady 1DV models, 2) by making an initial effort of tabulating the results of the intra-wave model for a specific situation, after which the morphodynamic model is run at relatively low costs, or 3) by finding analytical approximations to the governing equations (Bosboom, 1999).

In Bosboom and Cloin (1998) the development of an intra-wave sediment transport model is proposed. In the latter report, on the one hand, the presently available 1DV models are described focusing on the underlying physics and their merits and shortcomings as found in previously performed validation studies. On the other hand, necessary future developments are identified and a sediment transport model is proposed including many of these features and with a structure which facilitates cooperation on validation and future developments in an NCK framework. As such it could be considered as a "national sand transport model" acting as a 'knowledge carrier' ('kennisdrager'). Besides, an important aspect of the proposed model as compared to presently available models is the extension to field situations by including e.g. irregular waves, wave-induced streaming (and thus the treatment of vertical velocities) and the treatment of the complete water column.

Whereas the latter study can be seen as a first step by identifying the preferred developments, the present study is a follow-up aiming at the actual development of a first version of the intra-wave model (POINT-SAND model). The beta-release, on the floppy disk attached to this report, is thought to be a first version serving as a base for discussion, future extension and improvement. It does not pretend to be complete in the sense that all the processes to be modelled as identified in Bosboom and Cloin (1998) are taken into account. Also some numerical aspects can be improved in the future, especially regarding the sediment transport module. Although this module functions well when solving horizontal velocities only (as suffices for comparison with wave tunnel experiments), it does not yet work well when solving vertical velocities (as is needed when considering orbital motions generated by surface waves). In addition, calculated sediment concentrations still depend on the chosen grid schematization.

A limited number of wave-current interaction and sediment transport experiments were selected to compare with the model. The aim of this comparison was a first model diagnosis rather than an extensive model validation.

The beta-release however, in combination with the present report serving as a theoretical reference document is thought to provide a concrete basis for discussion in NCK-framework on a multitude of aspects ranging from process description, numerical treatment and model structure to in- and output requirements. It therewith aims at materializing the cooperation in NCK-framework with the ultimate aim to put an important step forward in the process-based descriptions of sediment transport.

1.2 Process description

The POINT-SAND model version described in this report has the following characteristics:

POINT-SAND model
2 horizontal velocity components (and 1 vertical)
vertical velocities and wave-induced streaming
irregular waves with vertical structure based on integral spectral parameters
turbulence closure using $k-L$ and $k-\varepsilon$ model including stratification
complete water column (including wave boundary layer) via boundary conditions at water surface and depth-dependent pressure gradient
hindered settling
2 (independent) sediment fractions, percentage of occurrence not taken into account in boundary condition at reference level
reference concentration at grain level according to Zyserman and Fredsøe (1994)
boundary conditions at water surface (harmonic components of surface elevation) or
possibility to reduce the description to wave tunnel situation (no vertical velocities and input above wave boundary layer; in that case (depth-averaged) velocity (time-series or harmonic components) is prescribed.

The directional point model (DPM/POINT-MUD; Winterwerp and Uittenbogaard, 1997) developed by joint funding of WL|Delft Hydraulics and Rijkswaterstaat RIKZ is used as a basis for the development of an intra-wave sand transport model (POINT-SAND model). The most far-reaching changes to the model structure result from taking into account the non-linear convective terms in momentum equations for the orbital velocity vector and the consistent coupling with a sand transport module.

1.3 Outline of report and floppy disk

In Chapter 2 an overview is given of some concepts and assumptions underlying the model. Also the solution procedure, using an inner and outer time loop, is outlined here. Chapter 3 describes the solution to the orbital velocity vector in the inner time loop. Chapter 4 deals with the turbulence closure model. In Chapter 5, the mean flow equations, solved in the outer time loop are given. The equations for the sediment are given in Chapter 6 . Chapter 7 gives a short description of some exercises focussing on diagnosis of the model. Section 7.3 describes a comparison with two wave tunnel experiments. One of the tests described here can also be found on the accompanying floppy disk which also contains the model executable. The input and output of the model are discussed here. Appendix A presents schematically the various loops as well as the most important subroutines; this appendix

serves as a rough guideline of the code. The essential assumption underlying the POINTSAND model is related to the treatment of horizontal variations. Appendix B investigates an additional approximation made in that respect, viz. that the horizontal part of the velocity-amplitude vector $\underline{\hat{u}}(z)$ is parallel with the corresponding wave number vector $\underline{k}$. In Appendix C we present details of the implementation of the partial slip condition for the turbulent flow along a bed in the fully-rough regime. Appendix D contains a listing of the input files of one of the wave-tunnel tests of which the results are reported on in Section 7.3.

1.4 Acknowledgements

This work is jointly funded by the MAST-3 SEDMOC project, in the framework of the EU-sponsored Marine Science and Technology Programme (MAST-III), under contractno. MAS3-CT97-0115 and the Dutch Ministry of Transport and Public Works (Rijkswaterstaat) under contractno. RKZ-725 part I, and WL | DELFT HYDRAULICS.

2 Overview of concepts and solution procedure

2.1 Introduction

This report describes an extended version of what we call the Directional Point Model (DPM) that solves the horizontal velocity vector as a function of depth for free-surface flows. Results with the DPM and its predecessor, the 1DV model (one velocity component only), are presented in (Kester et al., 1997) for simulating thermally-stratified tidal flows. In (Uittenbogaard et al., 1996) and (Winterwerp and Uittenbogaard, 1997) mud transport is simulated for steady as well as tidal flows and with the effect of surface waves parameterised by an increased bed roughness only. These existing 1DV and DPM codes were in principle already suitable for simulating sand transport in wave-tunnel experiments because these experiments do not induce a mean or orbital vertical velocity.

The purpose of the extension presented in this report, concerns mainly the inclusion of orbital motions for simulating more aspects of wave-current interaction (WCI), streaming, wave-turbulence interaction, all this in the context of simulating suspended sand transport under sheet-flow conditions. The flow along the entire water depth is simulated for a correct estimation of WCI. The selection of a non-equidistant vertical grid, however, allows for resolving details of the wave boundary layer.

The loading of the flow with suspended sediment is considered to yield damping of turbulence equivalent to salt-stratified or thermally-stratified flows. This stratified-flow analogy, however, requires modification to large particle densities. For the time being, the stratified-flow analogy is adopted in the implemented k-L and k-ε turbulence models through the usual buoyancy flux that represents the conversion of TKE into potential energy.

The extended DPM can be regarded as a spectral code. Per spectral component, it solves the orbital motions as a function of depth and mean flow profile. The direction of wave propagation as well as (tidal) flow is arbitrary and we assume spatially periodic wave motions. The latter assumption excludes sloping beds, strong decay or growth of wave properties. In principle, each harmonic component of a multi-directional wave spectrum is simulated although simulating many harmonics reduces the computation speed proportionally.

The waves are assumed to have infinitesimal wave height, while surface tension is neglected. There are no limitations on angular frequency, water depth, depth-averaged velocity or velocity shear rates, provided the latter do not induce wave blocking or a critical layer i.e. conditions where phase speed equals mean velocity.

2.2 Outline of concepts and solution procedure

By way of introduction, the solution strategy is presented here but the subsequent chapters describe the mathematical details.

The original DPM solves partial differential equations for flow, constituents (sediment, salt, heat etc.) and turbulence as a function of depth co-ordinate z and time t for a steady or slowly-varying (tidal) flow for a given depth-averaged horizontal velocity and using a hydrostatic pressure. In the original DPM, the momentum equation for one of the two horizontal velocity components reads

$$\frac{\partial U}{\partial t}+\frac{\partial P}{\partial x}=\frac{\partial}{\partial z}\left\{\left(\upsilon+\upsilon_T\right)\frac{\partial U}{\partial z}\right\}-T_x \tag{2.1}$$

with turbulence-averaged horizontal velocity U(z,t), turbulence-averaged pressure P, kinematic viscosity υ, eddy viscosity $\upsilon_T(z,t)$, horizontal co-ordinate x and vertical co-ordinate z. The DPM includes the Coriolis force but this contribution is not of importance here but included in the (extended) code. In this report, pressure is always divided by constant fluid density i.e. Boussinesq's approximation is applied. In (2.1), P is z-independent and $\partial P/\partial x$ is adjusted such that the depth-average of U(z,t) satisfies a user-defined temporal function or constant (time series or harmonic components on input). This is the original and satisfactory approach with the DPM, see (Uittenbogaard et al., 1996) and (Van Kester et al., 1997) for tests and applications.

The extension of the DPM for WCI involves the solution of the depth-dependent momentum equation for the orbital velocity vector of each spectral component as well as the dynamic and kinematic influence (Stokes drift) on mean flow and on turbulence. For the dynamic influence, the depth-dependent wave-current-interaction force T_x in (2.1) is essential. In the following, these influences are described briefly.

In the DPM, the WCI problem is formulated in Eulerian co-ordinates and for infinitesimal waves propagating on a non-uniform flow. In vector notation, the following equations for orbital momentum are added to the DPM:

$$\frac{\partial \underline{\tilde{u}}}{\partial t}+\left(\underline{U}+\underline{\tilde{u}}\right)\cdot\nabla\left(\underline{U}+\underline{\tilde{u}}\right)-\underline{U}\cdot\nabla\underline{U}+\nabla\tilde{p}=\nabla.\underline{\underline{\tilde{\sigma}}}+\underline{T}\quad;\quad\underline{U}\cdot\nabla\underline{U}=\underline{0}\quad, \tag{2.2}$$

with $\tilde{p}$ the hydrodynamic pressure driving the orbital velocity vector $\underline{\tilde{u}}$; the mean flow is horizontal and has just a vertical profile. For arbitrary wave and current direction, the WCI force $\underline{T}$ is a horizontal vector. Not all horizontal advection terms are implemented, but this will be presented later. Per spectral component, the hydrodynamic pressure $\tilde{p}$ is solved by its Poisson equation, linearized in terms of orbital motions. In (2.2), $\underline{\underline{\tilde{\sigma}}}$ is the stress tensor due to molecular as well as turbulent motions (Reynolds stress tensor $\underline{\underline{R}}$) and $\underline{\underline{\tilde{\sigma}}}$ is the oscillatory component of the stress tensor.

In the extended DPM, one of the WCI effects is the communication between (2.1) and (2.2) through the wave-averaged force $\underline{T}$. The separate solution in (2.1) and (2.2) of mean and orbital motions respectively allows a detailed study of orbital motions. If orbital motions would develop a non-zero mean Eulerian velocity then this mean value is considered to be an adjustment of the original mean-flow profile U(z). To that purpose (2.2) is corrected dynamically, through $\underline{T}$, for maintaining just a small wave-averaged horizontal Eulerian orbital velocity and (2.1) is affected by the opposite force $-\underline{T}$. In principle, the precise formulation of force $\underline{T}$ is irrelevant in this numerical approach, provided it is able to keep the wave-averaged horizontal Eulerian orbital velocity so small that this mean value can be neglected in (2.2). Note that just the sum of the momentum equation (2.1) for the mean horizontal velocity and the horizontal part of (2.2) for orbital motions matters. In this summation, $\underline{T}$ is eliminated and the total wave-averaged horizontal Eulerian velocity is the sum of U(z) and the wave-average of $\widetilde{u}$.

An additional wave-current force is introduced automatically through a change in turbulence conditions, and thus a change in υ_T in (2.1), by orbital shear rates and, of course, the state of turbulence changes through variations in $\partial\underline{U}/\partial z$ proper. These are all dynamic wave-current influences.

Another subject is estimating the Reynolds stresses in (2.2) as well as the turbulence production by orbital shear rates and this is done as follows. The momentum equations (2.2) are obtained after phase-averaging the Navier-Stokes equations with respect to the period of a spectral component. This phase-averaging leaves the orbital motions intact but removes random turbulent pressure fluctuations and the phase-averaging averages the random turbulent advection. The net effect of the latter, with the inclusion of molecular effects, yields in terms of momentum exchange the stress tensor $\underline{\underline{\widetilde{\sigma}}}$ in (2.2). The turbulence contribution $\underline{\underline{\widetilde{R}}}$ to $\underline{\underline{\widetilde{\sigma}}}$ is estimated by noting that just sufficiently-fast turbulent motions respond to the rapidly varying orbital shear rates (Kitaigorodskii and Lumley, 1983). In other words, just the high-pass filtered turbulent motions induce Reynolds stresses in $\underline{\underline{\widetilde{R}}}$, this high-pass filtering commences at the given angular frequency of the spectral component as well as the wave number of a spectral wave component.

Chapter 4 explains the closure for $\underline{\underline{\widetilde{R}}}$ but, for clarity, some introductory remarks are included here. Some researchers apply the following decomposition of the deviatoric part of the Reynolds stress tensor *after the application* of the Boussinesq hypothesis that introduces eddy viscosity υ_T

$$\underline{\underline{\widetilde{R}}} - \tfrac{1}{3} trace\left(\underline{\underline{\widetilde{R}}}\right)\underline{\underline{I}} = 2\widetilde{\upsilon}_T \underline{\underline{D}} + 2\overline{\upsilon}_T \underline{\underline{\widetilde{d}}} + 2\widetilde{\upsilon}_T \underline{\underline{\widetilde{d}}} \quad ; \quad \overline{\widetilde{\upsilon}}_T = 0 \quad ,$$

with the deviatoric stress tensor in the left-hand side, $\underline{\underline{I}}$ is the unit tensor, $\underline{\underline{D}}$ the strain-rate tensor of the mean flow and $\underline{\underline{\widetilde{d}}}$ the strain-rate tensor due to just the orbital motions. The problem is estimating the oscillatory eddy viscosity $\widetilde{\upsilon}_T$ that must have negative values during a wave period and these negative values complicate the numerical solution procedure.

Rather than using the previous formal approach, the following hydrodynamic argument is applied *prior to the application* of the Boussinesq hypothesis. The argument reads: just sufficiently fast as well as sufficiently small turbulent motions respond to the orbital strain rate $\underline{\underline{\tilde{d}}}$. From this physical argument a high-pass filter function f_{hp} ($0 \le f_{hp} \le 1$) is estimated and our closure for the Reynolds stress deviator then reads

$$\underline{\underline{\tilde{R}}} - \tfrac{1}{3} trace\left(\underline{\underline{\tilde{R}}}\right)\underline{\underline{I}} = 2 f_{hp} \upsilon_T \underline{\underline{\tilde{d}}}$$

where υ_T is based on a turbulence model wherein the time-dependent production of small-scale turbulence by the orbital motions is included. Near the free surface as well as near the bed, practically all energetic turbulent motions are confined to small scales as well as to rapid motions so that f_{hp} tends to unity at these levels. In the central part of the water column, however, turbulence usually is significantly slower than the orbital motions and there f_{hp} tends to zero. The layer near the bed with significant f_{hp} thus defines the wave-induced turbulent boundary layer.

Further, it is essential to recognise the causality of turbulent motions namely the turbulent motions respond to sufficiently slow and long orbital motions. Conversely, the mixing of sediment by turbulence responds to all turbulent motions so that the high-pass filter function is not applied to eddy diffusivity being the turbulence mixing coefficient for dissolved matter and sufficiently small sediment particles.

Finally, the kinematic influence of Stokes drift is incorporated in the given flow rate. The latter is obtained by adjustment of $\partial P/\partial x$ in (2.1), similar to the original DPM. The Stokes drift is estimated for waves on a non-uniform flow, see (Van Kester et al., 1996).

Note that the sum of (2.1) and (2.2) yields the dynamic equations for the total velocity, excluding turbulence fluctuations, after phase-averaging with respect to individual spectral components. Rather than solving the total momentum equations, the decomposed set (2.1) and (2.2) allows for splitting the turbulence response due to orbital motions or due to mean flow only.

In the DPM two time loops are made. In the *inner time loop*, orbital motions in (2.2) for each spectral component (input) and contributions of orbital motions to turbulence are solved. In the *inner time loop*, the orbital motions are solved by starting with the slowest motions and including non-linear coupling by advection of all spectral components. Per time step of the *inner time loop*, all orbital shear rates are collected and high-pass filtered. These filtered shear rates form the turbulence production term in the k-L or k-ε turbulence model that is solved at each *inner-loop* time step. Notice that the *inner time loop* contains another *spectral loop* namely solving each spectral component separately. The latter loop slows down the computation because the *spectral loop* is inside the *inner time loop* which, of course, is inside the *outer time loop*. In the *outer time loop*, subsequently, the wave-averaged forces and Stokes drifts of all spectral components are collected and the bed friction is low-pass filtered to solve the mean flow momentum equation (2.1), extended to arbitrary flow direction. In this *outer time loop*, a single and usually larger time step is

made. In a new cycle of the *inner time loop*, the adapted mean-flow profile is used to estimate the wave numbers for given angular frequencies and for estimating the advection of waves by a non-uniform current. This alternating solution procedure for (2.1) and (2.2) is repeated until end. Appendix A presents schematically the various loops as well as the most important subroutines; this appendix serves as a rough guideline of the code.

2.3 Simplifications

Compared with a 3D wave-current simulation, the essential simplification for using the DPM concerns horizontal variations. Steady harmonic oscillations at given angular frequency ω with flow-dependent wave number vector $\underline{k}$=(k, ℓ) with component k in x-direction and ℓ in y-direction are assumed i.e.

$$\tilde{\psi} = \hat{\psi}\,\mathrm{Re}\left\{\exp\left(i\,\underline{k}\cdot\underline{x} - i\,\omega t\right)\right\} \quad ; \quad i = \sqrt{-1} \quad , \tag{2.3}$$

with $\tilde{\psi}$ any wave-related variable with zero mean and with constant and real amplitude. The amplitude $\hat{\psi}(z)$ of any oscillatory variable may depend on the depth co-ordinate z. Accordingly, the following transform (2.4) is applied to all wave-related fluctuations:

$$\frac{\partial..}{\partial x} = -\frac{k(\omega)}{\omega}\frac{\partial..}{\partial t} \quad ; \quad \frac{\partial..}{\partial y} = -\frac{\ell(\omega)}{\omega}\frac{\partial..}{\partial t} \quad . \tag{2.4}$$

The wave-related surface elevation, with zero mean, is prescribed by

$$\tilde{\zeta} = \hat{\zeta}\sin\left[\underline{k}(\omega)\cdot\underline{x} - \omega t + \phi(\omega)\right] \tag{2.5}$$

with user-defined amplitude $\hat{\zeta}$ for each angular frequency ω as well as user-defined direction of propagation and user-defined phase shift ϕ. In the DPM, the wave number $\underline{k}$ is a horizontal vector and its magnitude follows from solving the dispersion relation; this is explained in Section 3.1.

Appendix B derives that, to a good approximation, the horizontal part of the velocity-amplitude vector $\underline{\hat{u}}(z)$ is parallel with the corresponding wave number vector $\underline{k}$.

3 Solving the orbital velocity vector

3.1 One-dimensional Poisson solver for pressure by surface waves on a non-uniform flow

In the *inner time loop* and per spectral component (*spectral loop*), first the orbital velocity vector is solved by (2.2) for each spectral component. For simplifying the notation, we shall not include the dependence of orbital variables on angular frequency ω explicitly unless ambiguity arises.

Per spectral component, pressure $\tilde{p}$ drives the momentum equations (2.2) for orbital velocity; in general $\tilde{p}$ is non-hydrostatic. Pressure $\tilde{p}$ is formulated in a Poisson equation that is derived from

$$\frac{\partial \underline{\tilde{u}}}{\partial t} + \left(\underline{U} + \underline{\tilde{u}}\right) \cdot \nabla \left(\underline{U} + \underline{\tilde{u}}\right) - \underline{U} \cdot \nabla \underline{U} + \nabla \tilde{p} = \underline{0} \quad ; \quad \underline{U} = \underline{U}(z)\, \underline{\hat{e}}_x \quad ; \quad \nabla \cdot \underline{\tilde{u}} = 0$$

for surface waves on a z-dependent mean flow and with the neglect of molecular, turbulence as well as neglecting all quadratic orbital-velocity terms (advection). These equations then yield the following linearized Poisson equation

$$\nabla^2 \tilde{p} = -2 \frac{\partial \underline{U}}{\partial z} \cdot \nabla \tilde{w} \quad . \tag{3.1}$$

Note that (3.1) includes waves relative to a vertically non-uniform flow at arbitrary angle of propagation. Substitution of (2.4) as well as of the linearized momentum equation for vertical velocity in (3.1) yields the following equivalent to the well-known Rayleigh equation:

$$\frac{d^2 \hat{p}}{dz^2} + 2B \frac{d\hat{p}}{dz} - |\underline{k}|^2 \hat{p} = 0 \quad ; \quad B = \frac{1}{\Omega} \cdot \frac{\partial \underline{U} \cdot \underline{k}}{\partial z} \quad ; \quad \Omega(z) = \omega - \underline{k} \cdot \underline{U}(z) \quad . \tag{3.2}$$

This ordinary differential equation for the pressure amplitude is discretized on the vertical grid of the DPM with pressure defined in cell centres and its vertical gradient at cell interfaces. The surface cell has number *m=1* and the bed cell *m=kmax*, the cell height is Δz_m. Typically 100-500 cells are used which may also be non-equidistant. Variables defined on the lower cell interface obtain the subscript of the cell above it and the variable at the mean water surface has subscript *m=0*.

The Poisson equation (3.2), equivalent to (3.1), is solved with vertical gradient $d\hat{p}/dz$ as principle unknown, see (Peyret and Taylor, 1983, Section 4.1), and by using quadratic splines for expressing pressure into its vertical gradient through:

$$\hat{p}_m - \hat{p}_{m+1} = \alpha_m \left(\frac{d\hat{p}}{dz}\right)_{m-1} + \beta_m \left(\frac{d\hat{p}}{dz}\right)_m + \gamma_m \left(\frac{d\hat{p}}{dz}\right)_{m+1} \quad , \tag{3.3}$$

with weight factors:

$$\beta_m = \tfrac{3}{8}\left(\Delta z_m + \Delta z_{m+1}\right) \quad ; \quad \alpha_m \equiv \gamma_m = \tfrac{1}{6}\beta_m \quad . \tag{3.4}$$

The exact boundary condition for pressure at the bed reads

$$\left.\frac{\partial \tilde{p}}{\partial z}\right|_{bed} = \frac{\partial}{\partial z}\left\{2(\upsilon + \upsilon_T)\frac{\partial \tilde{w}}{\partial z}\right\}_{bed} \quad ,$$

but Kraichnan (1956) showed that the gradient of normal stresses due to molecular and turbulent motions is negligible and thus the previous boundary condition can be simplified into

$$\left(\frac{d\hat{p}}{dz}\right)_{k\max} = 0 \quad . \tag{3.5}$$

Further, in Eulerian co-ordinates and at the mean water level, per spectral component the pressure is prescribed as

$$\tilde{p} = g\tilde{\zeta} \tag{3.6}$$

but numerically this conditions is now imposed on the pressure defined in the centre of the first cell (*m=1*) below the mean water level whence

$$\hat{p}_1 = g\hat{\zeta} - \tfrac{1}{8}\Delta z_1 \left\{3\left(\frac{d\hat{p}}{dz}\right)_0 + \left(\frac{d\hat{p}}{dz}\right)_1\right\} \tag{3.7}$$

holds after integrating a quadratic pressure profile over the top half of cell *m=1*. With (3.5) and (3.7), the Poisson equation (3.2) is solvable but for a yet unknown wave number magnitude $|\underline{k}|$. The latter is determined by the so-called dispersion relation. This relation follows from replacing $\tilde{w}$, in its linearized vertical momentum equation without viscous or turbulence stresses, by the linearized material derivative of ζ, yielding for sufficiently-small wave amplitude:

$$\left(\frac{\partial}{\partial t}+\underline{U}(z)\cdot\nabla\right)^2\tilde{\zeta}+\left(\frac{\partial\tilde{p}}{\partial z}\right)_{\bar{\zeta}}=0 \quad . \tag{3.8}$$

The angular frequency $\Omega(z)=\omega-\underline{k}.\underline{U}(z)$ in (3.2), as recorded by a co-moving observer at level z, then should satisfy at the mean water level:

$$\Omega^2\left(\bar{\zeta}\right)=\left(\frac{\partial^2\hat{p}}{\partial z\,\partial\hat{\zeta}}\right)_{\bar{\zeta}} \quad . \tag{3.9}$$

Starting with a potential-flow estimate for wave number magnitude $|\underline{k}|$, Ω is obtained from a finite difference version of (3.9) by solving (3.2) twice: for zero and for unit wave amplitude. The difference in vertical pressure gradient at the surface $z=\bar{\zeta}$ then yields Ω^2. By Picard iteration the new estimate for the wave number follows from

$$|\underline{k}|^{(n+1)}=\frac{\omega}{sign\left(\hat{\underline{k}}\cdot\underline{U}\left(\bar{\zeta}\right)\right)+\Omega^{(n)}/|\underline{k}|^{(n)}} \quad \text{for fixed } \frac{\ell}{|\underline{k}|} \quad ; \quad |\underline{k}|=\sqrt{k^2+\ell^2} \tag{3.10}$$

with iteration counter n=1,2,3... The Froude number is assumed subcritical so that no wave blocking or critical layer is formed i.e. $\Omega(z)$ is non-zero everywhere and thus B remains regular. Velthuizen and Van Wijngaarden (1969) consider the case of critical-layer formation at the level where $\Omega(z)=0$ holds. Initially, five to seven iterations are required for 1% relative accuracy. The dispersion relation is solved at the start of each *inner time loop*, using a new estimate of the mean flow profile in (3.2) and for subsequent starts of the inner loop just a single iteration appears sufficient.

Of course, the converged solution of (3.2) and dispersion relation (3.9) yields also the vertical profile of $d\hat{p}/dz$, normalised by the wave amplitude. From this pressure gradient follows the pressure proper and also, through (2.4), its horizontal gradient for all subsequent time steps in the *inner time loop*. Note that the harmonic function (2.5) for surface elevation is the single user-controlled input to the Poisson solver.

Per spectral component, the pressure gradients drive the momentum equations (2.2) for the horizontal and vertical velocity components. Section 3.2 starts with the latter because the vertical orbital velocity is used subsequently for vertical advection in the horizontal orbital velocity as treated in Section 3.3.

3.2 Solving the vertical orbital velocity per spectral component

The solution procedure for the vertical orbital velocity per spectral component is motivated as follows. In a 3D shallow-water solver in which the pressure is approximated by the hydrostatic pressure, the vertical velocity is obtained by vertically integrating, from the bed (z=0) upward, the divergence of the horizontal velocity vector:

$$w(\zeta) - w(0) = \int_0^{\zeta} \left. \frac{\partial u}{\partial x} \right|_z + \left. \frac{\partial v}{\partial y} \right|_z dz \quad . \tag{3.11}$$

This integration yields the vertical velocity at the free surface and, in virtue of mass conservation, this vertical velocity must be compatible with the material derivative of the surface elevation ζ i.e.

$$\frac{\partial \zeta}{\partial t} + u(\zeta)\frac{\partial \zeta}{\partial x} + v(\zeta)\frac{\partial \zeta}{\partial y} = w(\zeta) \quad . \tag{3.12}$$

This compatibility condition couples the (depth-integrated) horizontal momentum equations to the depth-integrated incompressibility condition $\nabla \cdot \underline{u} = 0$ which yields an equation in term of the horizontal velocity components (u,v) as well as the yet unknown ζ and with the vertical velocity eliminated. Once this coupled set is solved, the vertical profile of the vertical velocity follows from (3.11) without using the vertical momentum equation and this is what yields the passive or reactive response of vertical velocity. In this solution strategy, the vertical velocity component is the passive or reactive consequence of perturbations imposed on or through just the horizontal velocity vector such as flow rates on open boundaries, wind forcing, horizontal pressure gradients due to density differences etc.. Extensive experience with this solution procedure learns that the passive response of the vertical velocity does not yield the correct vertical motion of, for instance, a heavy or light blob of water. Instead, the hydrodynamic solver (Casulli and Stelling, 1998) can solve this problem correctly because the first estimate for the vertical velocity is derived from its momentum equation in which vertical forces and hydrodynamic pressure gradients are included.

For the purpose of investigating which terms are significant in wave-current interaction, therefore the vertical velocity is solved here first by its simplified momentum equation and this equation is driven by the vertical hydrodynamic pressure gradient. This solution procedure allows for the application of the compatibility condition (3.12) but it does not guarantee the incompressibility condition (3.11). Tests with the extended DPM, however, show that the deviations from (3.12) appear small although a distinct criterion for approximating (3.12) is lacking. A dedicated proof of approximating (3.12) is implementing a transport equation for a conserved scalar and checking the temporal deviations from an initially uniformly-distributed constituent.

Thus the vertical orbital velocity is solved through a simplified momentum equation. As announced in Section 3.1, not all advection terms in (2.2) are included in the simulation and most of them are removed for solving the vertical orbital velocity. The following linearized momentum equation for the vertical orbital-velocity component is adopted:

$$\frac{\partial \tilde{w}}{\partial t} + \underline{U}(z) \cdot \nabla \tilde{w} + \frac{\partial \tilde{p}}{\partial z} = \frac{\partial}{\partial z}\left\{ 2\left(\upsilon + f_{hp}\upsilon_T\right)\frac{\partial \tilde{w}}{\partial z} \right\} \quad . \tag{3.13}$$

Note that inconsistent with the Poisson equation (3.1) and its boundary condition (3.5), the vertical momentum equation (3.13) is extended with the influence of turbulence on the vertical orbital velocity component. The inclusion of vertical advection has been tested but it overestimates the vertical velocity near the bed, probably because the solution procedure for the vertical pressure gradient does not account for this non-linearity but more analysis is recommended.

In (3.13), υ is the kinematic viscosity and υ_T the eddy viscosity for vertical exchange of mean horizontal momentum. In (3.13),

$$\frac{\partial}{\partial x}\left\{2\left(\upsilon + f_{hp}\upsilon_T\right)\left(\frac{\partial \tilde{u}}{\partial z} + \frac{\partial \tilde{w}}{\partial x}\right)\right\} \quad ; \quad \frac{\partial}{\partial y}\left\{2\left(\upsilon + f_{hp}\upsilon_T\right)\left(\frac{\partial \tilde{v}}{\partial z} + \frac{\partial \tilde{w}}{\partial y}\right)\right\}$$

being the horizontal gradient of the Reynolds shear stress is neglected as it would involve complicated estimates for horizontal gradients of $\partial\tilde{u}/\partial z$ and $\partial\tilde{w}/\partial x$, the latter yielding second-order temporal derivatives of $\tilde{w}$. The eddy viscosity υ_T, however, is reduced by a (high-pass) filter-function f_{hp} depending on wave angular frequency. The product of this filter function and the total eddy viscosity represents the reduced eddy viscosity due to turbulent motions that respond sufficiently fast to the orbital shear rates; see Chapter 4 for more details.

On the impermeable bed we have

$$\tilde{w} = 0 \tag{3.14}$$

The surface condition needs more elaboration for both orbital velocity components as well as for the mean flow and therefore the stress balance at the surface is considered first. Continuity of pressure as well as zero tangential shear stresses on the water surface demand, in absence of wind:

$$z = \bar{\zeta}: \quad \sigma_{xx} n_x + \sigma_{xz} n_z = 0 \quad ; \quad \sigma_{xz} n_x + \sigma_{zz} n_z = 0 \quad \text{with} \quad \frac{n_x}{n_z} = -\frac{\partial \tilde{\zeta}}{\partial x} \quad . \tag{3.15}$$

This is the simplest approximation to the free-surface condition at it is of zero order accuracy neglecting the surface elevation. In (3.15), σ_{ij} (i,j=1,2,3 or x,y,z) are the deviatoric stress components and (n_x,n_z) are the components of the upward-directed normal to the water surface of which its mean inclination, due to mean horizontal pressure gradient, is neglected. The stresses are due to molecular motions as well as due to Reynolds stresses which are closed by introducing an isotropic eddy viscosity. Combining the two stress balances in (3.15) yields:

$$z = \bar{\zeta}: \quad \sigma_{zz} = \left(\frac{n_x}{n_z}\right)^2 \sigma_{xx} \tag{3.16}$$

and thus σ_{zz} is of third-order in wave amplitude so that at least to first-order, the boundary condition for vertical orbital velocity reads:

$$z = \bar{\zeta}: \quad \frac{\partial \tilde{w}}{\partial z} = 0 \quad . \tag{3.17}$$

Further, from the first condition in (3.15) as well as the stress closures follows:

$$z = \bar{\zeta}: \quad \frac{\partial U}{\partial z} + \frac{\partial \tilde{u}}{\partial z} + \frac{\partial \tilde{w}}{\partial x} = 2\frac{\partial \tilde{u}}{\partial x}\frac{\partial \tilde{\zeta}}{\partial x} \tag{3.18}$$

so that to first-order in wave amplitude, for the horizontal orbital velocity:

$$z = \bar{\zeta}: \quad \frac{\partial \tilde{u}}{\partial z} = -\frac{\partial \tilde{w}}{\partial x} \tag{3.19}$$

holds because the mean of (3.18) demands for the mean vertical shear rate:

$$z = \bar{\zeta}: \quad \frac{\partial U}{\partial z} = 2\overline{\frac{\partial \tilde{u}}{\partial x}\frac{\partial \tilde{\zeta}}{\partial x}} \quad . \tag{3.20}$$

The horizontal gradient in the linearized material derivative is converted through (2.4) into a temporal derivative i.e.

$$\frac{\partial \tilde{w}}{\partial t} + U(z)\frac{\partial \tilde{w}}{\partial x} + V(z)\frac{\partial \tilde{w}}{\partial y} \equiv \left(1 - \frac{\underline{k}.\underline{U}(z)}{\omega}\right)\frac{\partial \tilde{w}}{\partial t} \quad . \tag{3.21}$$

The momentum equation (3.13) for the vertical orbital-velocity component and its boundary conditions (3.14) and (3.19) are solved on the same grid as the wave-related pressure. The vertical velocity is defined at vertical cell interfaces where also the vertical pressure gradient has been defined. In this staggered mesh, condition (3.14) can be imposed on the bed and the zero normal-stress condition (3.16) closes diffusion in (3.13) at the free surface.

Equation (3.13) is solved with $\tilde{w}$ as principle unknown and diffusion is integrated with Euler implicit. The pressure gradient in (3.13) is time centred.

Notice that first the surface elevation is prescribed in (3.7) and then the hydrodynamic pressure is solved and subsequently (3.13) is solved for the vertical orbital velocity which appears to be essential for creating the wave-current force that affects the vertical profile of the mean horizontal velocity. In the next section, this role of the vertical orbital velocity will become more apparent.

3.3 Solving the horizontal orbital velocity of a single spectral component

Our numerical simulations have shown that the vertical advection, by orbital velocity $\tilde{w}$, of horizontal orbital momentum is responsible for creating the major contribution to the wave-induced force that affects the vertical profile of the mean horizontal velocity. Rather than modelling this momentum transfer, the creation of this force is simulated directly by solving the non-linear momentum equation for the horizontal orbital velocity.

The equation for the horizontal orbital velocity is arranged such that it allows for the simulation of the orbital motions as part of a given wave number spectrum of surface elevations. Therefore, we start with (2.2) for a horizontal mean flow. Initially, we neglect the RHS of (2.2) but later we include the unbalance of turbulence stresses. For the purpose of solving orbital motions for a given spectrum, the orbital velocity in (2.2) is replaced by the sum

$$\underline{\tilde{u}} \rightarrow \underline{\tilde{u}} + \underline{\tilde{v}} \tag{3.22}$$

where $\underline{\tilde{v}}$ represents all other contributions at wave numbers that differ from wave number $\underline{k}$ belonging to $\underline{\tilde{u}}$. Formally we thus define

$$\underline{\tilde{u}} = \underline{\tilde{u}}(\omega_s) \quad ; \quad \underline{\tilde{v}} = \sum_{n \neq s} \underline{\tilde{u}}(\omega_n) \tag{3.23}$$

with ω_n (n=1,2,3,...) the angular frequencies of the spectral components defined by the user. The previous decomposition is applied to (2.2) and it reads

$$\frac{\partial \underline{\tilde{u}} + \underline{\tilde{v}}}{\partial t} + \left(\underline{U} + \underline{\tilde{u}} + \underline{\tilde{v}}\right) \cdot \nabla \left(\underline{\tilde{u}} + \underline{\tilde{v}}\right) + \left(\underline{\tilde{u}} + \underline{\tilde{v}}\right) \cdot \nabla \underline{U} + \nabla \left(\tilde{p}_u + \tilde{p}_v\right) = \underline{0} \tag{3.24}$$

where p_u is the pressure related to the orbital velocity $\underline{\tilde{u}}$ and likewise p_v is related to $\underline{\tilde{v}}$. An obvious decomposition of (3.24) are the following momentum equations for $\underline{\tilde{u}}$ and $\underline{\tilde{v}}$ separately:

$$\frac{\partial \underline{\tilde{u}}}{\partial t} + \left(\underline{U} + \underline{\tilde{u}} + \underline{\tilde{v}}\right) \cdot \nabla \underline{\tilde{u}} + \underline{\tilde{u}} \cdot \nabla \underline{U} + \nabla \tilde{p}_u = \underline{0} \tag{3.25}$$

$$\frac{\partial \underline{\tilde{v}}}{\partial t} + \left(\underline{U} + \underline{\tilde{u}} + \underline{\tilde{v}}\right) \cdot \nabla \underline{\tilde{v}} + \underline{\tilde{v}} \cdot \nabla \underline{U} + \nabla \tilde{p}_v = \underline{0} \tag{3.26}$$

The sum of (3.25) and (3.26) equals (3.24). Of course, (3.26) can be decomposed further into other wave number components.

Next, a convenient simplification is introduced that allows for solving just one horizontal momentum equation per wave number or angular frequency rather than solving two

equations for the two horizontal orbital velocity components. This simplification is based on the linearized version

$$\frac{\partial \underline{\tilde{u}}}{\partial t} + \underline{U} \cdot \nabla \underline{\tilde{u}} + \underline{\tilde{u}} \cdot \nabla \underline{U} + \nabla \tilde{p}_u = \underline{0} \tag{3.27}$$

of the non-linear momentum equation (3.25). Appendix B shows that the orbital velocity vector can be decomposed as:

$$\underline{\tilde{u}} = \tilde{u}\,\underline{\hat{k}} + \tilde{w}\,\underline{\hat{m}} \quad ; \quad \underline{\hat{k}} = \frac{\underline{k}}{|\underline{k}|} \quad ; \quad |\underline{\hat{m}}| = 1 \quad ; \quad \underline{\hat{m}} \cdot \underline{\hat{k}} = 0 \tag{3.28}$$

In (3.28), $\underline{\hat{k}}$ is the unit vector parallel to the (horizontal) wave number $\underline{k}$ and the unit vector $\underline{\hat{m}}$ is directed against gravity. The essential aspect of (3.28) is that the horizontal part of the orbital velocity vector is parallel to its wave number vector $\underline{k}$. For surface waves propagating with some angle to a flow having vertical velocity profile, the latter is not obvious. Nevertheless, Appendix B shows that this parallelism is approximated excellently. The convenient consequence of this parallelism becomes apparent after the scalar multiplication of (3.25) with the horizontal unit vector $\underline{\hat{k}}$ yielding:

$$\frac{\partial \tilde{u}}{\partial t} + \left\{ \left(\underline{U} + \underline{\tilde{v}} \right) \cdot \underline{\hat{k}} + \tilde{u} \right\} \frac{\partial \tilde{u}}{\partial x_k} + \tilde{w}_u \frac{\partial \tilde{u}}{\partial z} + \tilde{w}_u \frac{\partial \underline{U} \cdot \underline{\hat{k}}}{\partial z} + \frac{\partial \tilde{p}_u}{\partial x_k} = 0 \tag{3.29}$$

with x_k the horizontal co-ordinate in positive $\underline{k}$ direction and $\tilde{w}_u$ the vertical component of $\underline{\tilde{u}}$ all related to a single spectral component. Thus (3.29) is a single horizontal momentum equation obtained by projection of the "external" flow field $\left(\underline{U} + \underline{\tilde{v}} \right)$ on the direction $\underline{k}$ rather than splitting the horizontal part of $\underline{\tilde{u}}$ with respect to horizontal directions parallel and normal to e.g. $\underline{U}$. The horizontal momentum equation (3.29) shows that the vertical gradient of the mean horizontal velocity vector is significant only if it has a component parallel to $\underline{k}$. Likewise, there is advection by $\left(\underline{U} + \underline{\tilde{v}} \right)$ provided $\left(\underline{U} + \underline{\tilde{v}} \right)$ has a component in the direction $\underline{k}$ of wave propagation.

Note that (3.29) for the horizontal vector $\underline{\tilde{u}}$ contains the following linear and non-linear (wave-wave) interaction terms:

	$\underline{U}$	$\underline{\tilde{v}}$	$\underline{\tilde{u}}$
$\underline{U}$	$\underline{U} \cdot \nabla \underline{U}$	$\underline{U} \cdot \nabla \underline{\tilde{v}}$	$\underline{U} \cdot \nabla \underline{\tilde{u}}$
$\underline{\tilde{v}}$	$\underline{\tilde{v}} \cdot \nabla \underline{U}$	$\underline{\tilde{v}} \cdot \nabla \underline{\tilde{v}}$	$\underline{\tilde{v}} \cdot \nabla \underline{\tilde{u}}$
$\underline{\tilde{u}}$	$\underline{\tilde{u}} \cdot \nabla \underline{U}$	$\underline{\tilde{u}} \cdot \nabla \underline{\tilde{v}}$	$\underline{\tilde{u}} \cdot \nabla \underline{\tilde{u}}$

Table 1 Overview of linear and non-linear (wave-wave) interaction terms in (3.29)

In the following the reference to wave number $\underline{k}$ in the horizontal co-ordinate x_k is omitted. Instead, x_k is replaced by co-ordinate x parallel to the direction of wave propagation. Likewise, $\tilde{w}$ is written in place of $\tilde{w}_u$ and also $\tilde{p}$ in place of $\tilde{p}_u$. We believe these notational simplifications do not create ambiguity because they all relate to the horizontal velocity subject of the equation in which they appear. Consequently (3.29), extended with the RHS of (3.1), reads:

$$\begin{aligned} &\frac{\partial \tilde{u}}{\partial t} + \left\{\left(\underline{U} + \underline{\tilde{v}}\right)\cdot \underline{\hat{k}} + \tilde{u}\right\}\frac{\partial \tilde{u}}{\partial x} + \tilde{w}\frac{\partial \tilde{u}}{\partial z} + \tilde{w}\frac{\partial \underline{U}\cdot \underline{\hat{k}}}{\partial z} + \frac{\partial \tilde{p}}{\partial x} = \\ &\frac{\partial}{\partial x}\left\{2\left(\upsilon + f_{hp}\upsilon_T\right)\frac{\partial \tilde{u}}{\partial x}\right\} + \frac{\partial}{\partial z}\left\{\left(\upsilon + f_{hp}\upsilon_T\right)\left(\frac{\partial \tilde{u}}{\partial z} + \frac{\partial \tilde{w}}{\partial x}\right)\right\} + T_x \end{aligned} \tag{3.30}$$

In (3.30) the spatial derivative in the transverse (y) direction as well as the corresponding transverse velocity component are omitted by the approximation presented in Appendix B. Further, the x-direction in (3.30) is parallel to the direction $\underline{k}$ of wave propagation.

The terms

$$\tilde{u}\frac{\partial \tilde{u}}{\partial x} + \underline{\tilde{v}}\cdot\underline{\hat{k}}\frac{\partial \tilde{u}}{\partial y} + \tilde{w}\frac{\partial \tilde{u}}{\partial z} \quad , \tag{3.31}$$

see also Table 1, represent the *non-linear advection terms* in the DPM of which

$$\tilde{w}\frac{\partial \tilde{u}}{\partial z} \tag{3.32}$$

appears to be the most prominent one for the experiments of Klopman (1994).

The horizontal orbital pressure gradient that drives (3.22) follows from the hydrodynamic pressure (Section 3.1) as well as from (2.4) for expressing the horizontal derivative into temporal derivative which is defined time centred.

Note that, except T_x, all terms in the RHS of (3.30) are due to the molecular and the turbulence stresses that we neglected upon deriving the linearized Poisson equation (3.1). The x-component F_x of the divergence of the Reynolds and viscous stress tensor is simplified as follows. First define F_x according to the RHS of (3.30), excluding the WCI force T_x, as:

$$F_x = \frac{\partial}{\partial x}\left\{2\left(\upsilon + f_{hp}\upsilon_T\right)\frac{\partial \tilde{u}}{\partial x}\right\} + \frac{\partial}{\partial z}\left\{\left(\upsilon + f_{hp}\upsilon_T\right)\frac{\partial \tilde{u}}{\partial z}\right\} + \frac{\partial}{\partial z}\left\{\left(\upsilon + f_{hp}\upsilon_T\right)\frac{\partial \tilde{w}}{\partial x}\right\} \quad . \tag{3.33}$$

Subsequently, the horizontal variations in eddy viscosity and filter function are neglected. Further, the first order horizontal derivative is replaced by the temporal derivative, see (2.4) and the second-order derivative by using (2.3) so that F_x reads

$$F_x = 2k^2\left(\upsilon + f_{hp}\upsilon_T\right)\tilde{u} + \frac{\partial}{\partial z}\left\{\left(\upsilon + f_{hp}\upsilon_T\right)\frac{\partial \tilde{u}}{\partial z}\right\} - \frac{k}{\omega}\frac{\partial}{\partial z}\left\{\left(\upsilon + f_{hp}\upsilon_T\right)\frac{\partial \tilde{w}}{\partial t}\right\} \quad . \tag{3.34}$$

The formulation (3.34) is implemented in the DPM.

We continue with the implementation of the temporal derivative and horizontal advection terms in (3.30). The horizontal advection terms are approximated by

$$\frac{\partial \tilde{u}}{\partial t} + \left\{\left(\underline{U} + \underline{\tilde{v}}\right)\cdot\underline{\hat{k}} + \tilde{u}\right\}\frac{\partial \tilde{u}}{\partial x} = \left\{1 - \frac{k}{\omega}\left[\left(\underline{U} + \underline{\tilde{v}}\right)\cdot\underline{\hat{k}} + \tilde{u}\right]\right\}\left.\frac{\partial \tilde{u}}{\partial t}\right|_{t+\frac{1}{2}\Delta t} \tag{3.35}$$

with $\Delta t^{(orb)}$ the time step applied in the *inner time loop*. For more than one spectral components, the advection (3.35) is solved in a *spectral loop* that starts with the lowest angular frequency such that holds

$$\underline{\hat{k}}\cdot\underline{\tilde{v}} = \underline{\hat{k}}\cdot\underline{\tilde{u}}^{(-)} + \underline{\hat{k}}\cdot\underline{\tilde{u}}^{(+)} \tag{3.36}$$

with

$$\underline{\tilde{u}}^{(-)}\left(t + \tfrac{1}{2}\Delta t^{(orb)}\right) = \sum_{n<s}\underline{\tilde{u}}\left(t + \tfrac{1}{2}\Delta t^{(orb)}; \omega_n\right) \quad ; \quad \underline{\tilde{u}}^{(+)}(t) = \sum_{s<n}\underline{\tilde{u}}\left(t; \omega_n\right) \tag{3.37}$$

with ω_s the angular frequency implicitly referred to in (3.30) and using the orbital velocity $\tilde{u}(t)$ of the previous inner-loop time step for the faster spectral components. In principle, a return *sweep* in the *spectral loop* starting at the highest angular frequency can be included, similar to Gauss-Seidel elimination procedure in solving matrix equations. Here we assume that $\Delta t^{(orb)}$ is sufficiently small and short waves are affected mostly by longer waves than vice versa and we neglect the return sweep.

The approximation (3.35)) and the solution sequence defined by (3.36) and (3.37) in the spectral loop are implemented in the DPM.

The vertical advection (3.32) of horizontal orbital momentum is defined in the centre of the m^{th} cell and it is discretized by

$$\left.\tilde{w}\frac{\partial \tilde{u}}{\partial z}\right|_m = \left\{\tfrac{1}{2} - \theta\, sign\left(\tilde{w}_{m+\frac{1}{2}}\right)\right\}\left.\tilde{w}\frac{\partial \tilde{u}}{\partial z}\right|_{m-1} + \left\{\tfrac{1}{2} + \theta\, sign\left(\tilde{w}_{m+\frac{1}{2}}\right)\right\}\left.\tilde{w}\frac{\partial \tilde{u}}{\partial z}\right|_m \tag{3.38}$$

with θ for weighting central (θ=0) and first-order upwind (θ=0.5) schemes. For simulating the wave-current experiments of (Klopman, 1994) with 100 equidistant layers and 100 time

steps per wave period, the central scheme does not wiggle but for safety we set θ=0.1. Because the vertical orbital velocity is also known at the new time level, the LHS of (3.38) is time-centred and the gradient $\partial\tilde{u}/\partial z$ at the new time level is treated implicitly.
The discrete representation of the horizontal-momentum equation (3.30) is formulated with $\partial\tilde{u}/\partial z$ as principle unknown and using Hermite interpolation similar to (3.3):

$$\tilde{u}_m - \tilde{u}_{m+1} = \alpha_m \left(\frac{\partial \tilde{u}}{\partial z}\right)_{m-1} + \beta_m \left(\frac{\partial \tilde{u}}{\partial z}\right)_m + \gamma_m \left(\frac{\partial \tilde{u}}{\partial z}\right)_{m+1} \quad , \tag{3.39}$$

with weight factors: $\beta_m = \frac{1}{2}\left(\Delta z_m + \Delta z_{m+1}\right)$; $\alpha_m \equiv \gamma_m = 0$.

The Hermite interpolation (3.39), however, allows for a weighting matched to a strongly non-equidistant grid such as a logarithmic distribution can be used without loss of accuracy. The latter requires weight factors different from those in (3.4) and these are not implemented yet.

Finally, our definition of the depth-dependent WCI force per the orbital motions with angular frequency ω_s reads

$$\begin{aligned} &T_x\left(z,(l+\tfrac{1}{2})T;\omega_s\right) = \frac{\overline{\tilde{u}(z;\omega_s)}}{T} \quad ; \quad \overline{\tilde{u}(z;\omega_s)} = \frac{1}{T}\int_{lT}^{(l+1)T} \tilde{u}(z,t;\omega_s)\,dt \quad ; \\ &T = \frac{2\pi}{\omega_s} \quad ; \quad l = 0,1,2,3,\ldots \quad . \end{aligned} \tag{3.40}$$

In (3.40), l is the time step counter for the *outer time loop*. This numerical formulation of wave-current force T_x follows from averaging the horizontal orbital velocity over the *previously-simulated wave period* and dividing it by the wave period. This force represents an acceleration meant for obtaining a sufficiently-small and steady wave-averaged Eulerian orbital velocity in (3.30) and, inversely, it is a force exerted by the orbital motions on the mean flow. Therefore, with the opposite sign, T_x appears in the momentum equation (2.1) for the mean or wave-averaged horizontal velocity. As outlined in Section 2.2, the formulation of T_x by (3.40) is a purely numerical and the formulation does not reflect an analytical solution. The mere role of (3.40) is yielding a sufficiently small wave-averaged Eulerian orbital velocity and closing the force balance with the mean-flow momentum equation. After summation of (3.30) to the mean-flow momentum equation, the WCI force T_x vanishes.

The formulation (3.40) is implemented in the DPM. In a separate subroutine, the time integration in (3.40) is ended and re-initialised at every second zero crossing of $\tilde{\zeta}(t;\omega_s)$. Note that there is a time lag in the WCI force per spectral component depending on the time step in the *outer time loop* as well as the period of the particular spectral component. Moreover, after completion of a wave cycle, the WCI force is updated and this creates a jump in WCI force in the mean-momentum equation. For a monochromatic wave this jump is not serious as it disappears upon convergence to stationary conditions. For multi-

component waves, however, the wave-wave interactions create ongoing oscillations in the respective WCI forces and the sum of these forces perturb the mean momentum and this sum can create e.g. subharmonic quite faithfully. In the latter case, however, the jumps in WCI force create a non-convergence in the mean flow solution, irrespective of the time step in the *outer time loop*. For obtaining convergence therefore the WCI forces are adjusted gradually over the respective wave period by the following procedure. Consider the following differential equation

$$\frac{d\eta}{d\tau} = \alpha\,\tau(\eta_0 - \eta) \tag{3.41}$$

with the solution: $\eta = \eta_0\left\{1 - \exp\left(-\tfrac{1}{2}\alpha\,\tau^2\right)\right\}$ that changes gradually from η=0 to $\eta=\eta_0$.

Based on (3.41), the change in WCI force after a wave cycle is gradually adjusted by the finite difference scheme

$$\eta^{(n+1)} = \eta^{(n)} + \frac{n\alpha}{N^2}\left(\eta_0 - \eta^{(n)}\right) \quad ; \quad n = 1,2,\ldots,N \quad , \tag{3.42}$$

where N is the number of time steps in the inner time loop covering one wave period and integer n is the counter which is reset to n=0 after every second zero crossing of the surface elevation. In (3.42), α is taken so that $\eta^{(N)}=r.\eta_0$ which requires $\alpha=-\ln\{(1-r)^2\}$ and η represents the WCI force and for η_0 a prediction is substituted. This prediction is based on (3.40) and it reads $\eta_0=2.T_x(\text{new})-T_x(\text{old})$ with T_x(new) defined by the latest evaluation of (3.42) and T_x(old) the result of (3.42) at this evaluation. For bichromatic waves this approach yields converged solutions.

As derived in the previous section, see (3.19), the conditions for a stress-free surface demand to zero order in wave amplitude:

$$z = \bar{\zeta}: \quad \frac{\partial \tilde{u}}{\partial z} = -\frac{\partial \tilde{w}}{\partial x} = \frac{k}{\omega}\frac{\partial \tilde{w}}{\partial t} \quad . \tag{3.43}$$

In case of a free surface subjected to wind shear stress, the condition (3.43) still holds when the wind shear stress does not vary in the rhythm of the surface waves.

The bed condition for orbital motions can be based on a turbulent boundary layer i.e. a partial slip condition or viscous sublayer i.e. the no-slip condition.

The partial slip condition for a turbulent over a hydraulically rough bed requires subtle definition for obtaining results independent of the thickness $\Delta z(kmax)$ of the computational bed boundary layer. In literature on 1DV models for orbital motions we found insufficient details for reference and therefore we present our procedure in detail (see also Appendix C).

Therefore, the well-known quadratic friction law is applied for the bed shear stress:

$$\left(\upsilon + \upsilon_T\right)\left(\frac{\partial \underline{U}}{\partial z} + \frac{\partial \underline{\widetilde{u}}}{\partial z}\right)\Bigg|_{z=z_0} = \frac{\left|\underline{\overline{u}} + \underline{\widetilde{u}}\right|\left(\underline{\overline{u}} + \underline{\widetilde{u}}\right)}{S^2}\Bigg|_{z=\frac{1}{2}\Delta z_{k\max}} \tag{3.44}$$

with

$$S = \frac{1}{\kappa}\log\left(1 + \frac{\frac{1}{2}\Delta z_{k\max}}{z_0}\right) \quad ; \quad \kappa = 0.41 \quad , \tag{3.45}$$

for a quasi-steady log-layer with roughness length z_0 1/30 of the Nikuradse length scale k_s. In (3.44), the filter function f_{hp} has been set to unity because in the bed boundary layer, turbulence is sufficiently fast for responding in a quasi-steady fashion to the imposed orbital shear rates. The latter is substantiated in Chapter 4. In (3.45), the level $\frac{1}{2}\Delta z_{k\max}$ refers to the first computational velocity point above the bed.

According to the standard procedure for solving the mean momentum equation in the original DPM, (3.22) is discretized on a staggered grid with velocity $\widetilde{u}$ in cell centre and its vertical gradient on cell interfaces. The principle unknown is $\partial\widetilde{u}/\partial z$ and Hermite interpolation similar to (3.3) is applied with diffusion Euler implicit. Further, the bed boundary condition using the quadratic bed friction is solved semi-implicitly by products of flow variables at old and new time levels. To that purpose, the vertical velocity gradient is coupled to the near-bed velocity at the new time level through

From (3.44) follows the wave-induced part of the bed shear stress vector which has zero mean:

$$\underline{\widetilde{\tau}}_b = \left(\upsilon + f_{hp}\upsilon_T\right)\frac{\partial \underline{\widetilde{u}}}{\partial z}\Bigg|_{z_0} = S^{-2}\left(\left|\underline{u}\right|\underline{u} - \overline{\left|\underline{u}\right|\underline{u}}\right)_{\frac{1}{2}\Delta z_{k\max}} \tag{3.46}$$

Decomposed into mean and orbital motions the previous equation reads

$$\underline{\widetilde{\tau}}_b = \left(\upsilon + f_{hp}\upsilon_T\right)\frac{\partial \underline{\widetilde{u}}}{\partial z}\Bigg|_{z_0} = S^{-2}\left(\left|\underline{U} + \underline{\widetilde{u}}\right|\underline{U} + \left|\underline{U} + \underline{\widetilde{u}}\right|\underline{\widetilde{u}} - \overline{\left|\underline{u}\right|\underline{u}}\right)_{\frac{1}{2}\Delta z_{k\max}} \tag{3.47}$$

For the purpose of Hermite interpolation a connection between orbital velocity and its vertical gradient is desired and this relation follows from re-arranging the previous equation into:

$$S^{-2}\left(\left|\underline{U} + \underline{\widetilde{u}}\right|\underline{\widetilde{u}}\right)_{\frac{1}{2}\Delta z_{k\max}} - \left(\upsilon + f_{hp}\upsilon_T\right)\frac{\partial \underline{\widetilde{u}}}{\partial z}\Bigg|_{z_0} = S^{-2}\left(\overline{\left|\underline{u}\right|\underline{u}} - \left|\underline{U} + \underline{\widetilde{u}}\right|\underline{U}\right)_{\frac{1}{2}\Delta z_{k\max}} \tag{3.48}$$

or after division by $S^{-2}\left|\underline{U}+\underline{\tilde{u}}\right|_{\frac{1}{2}\Delta z_{k\max}}$:

$$\underline{\tilde{u}}\left(\tfrac{1}{2}\Delta z_{k\max}\right)-\left(\upsilon+f_{hp}\upsilon_T\right)\left.\frac{\partial\underline{\tilde{u}}}{\partial z}\right|_{z_0}=\left.\frac{\overline{|\underline{u}|\underline{u}}}{\left|\underline{U}+\underline{\tilde{u}}\right|}\right|_{\frac{1}{2}\Delta z_{k\max}}-\underline{U}\left(\tfrac{1}{2}\Delta z_{k\max}\right) \tag{3.49}$$

At the bed al turbulent motions are smaller as well as faster than the orbital motions so that f_{hp}=1. Further, the time levels are considered for implicit integration so that the previous equation yields:

$$\begin{aligned}\underline{\tilde{u}}\left(\tfrac{1}{2}\Delta z_{k\max},t+\Delta t\right)-\frac{\left[\upsilon+\upsilon_T\left(z_0,t\right)\right]S^2}{\left|\underline{U}+\underline{\tilde{u}}\left(\tfrac{1}{2}\Delta z_{k\max},t\right)\right|}\left.\frac{\partial\underline{\tilde{u}}\left(z,t+\Delta t\right)}{\partial z}\right|_{z_0}=\\ \left.\frac{\overline{\left|\underline{U}+\underline{\tilde{u}}\right|\left(\underline{U}+\underline{\tilde{u}}\right)}}{\left|\underline{U}+\underline{\tilde{u}}\left(\tfrac{1}{2}\Delta z_{k\max},t\right)\right|}\right|_{\frac{1}{2}\Delta z_{k\max}}-\underline{U}\left(\tfrac{1}{2}\Delta z_{k\max},t\right)\end{aligned} \tag{3.50}$$

The LHS of (3.50) contains the desired implicit coupling for the new time level in the inner time loop in which (3.22) is solved and all variables in the RHS of (3.50) are defined at previous time level(s).

Comments

Note that the definition (3.27) of T_x is not based on an analytic model for the wave-current force. The sole purpose of T_x is obtaining such a small mean horizontal orbital velocity that this mean value can be neglected in the horizontal orbital momentum equation (3.22).

This numerical role of T_x is similar to the role of the hydrodynamic pressure correction q in fractional-step methods such as applied in (Casulli and Stelling, 1998, eq. 21 to 24) using the velocity $\underline{u}_h$ of the hydrostatic pressure solution in

$$\frac{\partial\underline{u}-\underline{u}_h}{\partial t}+\nabla q=0\quad;\quad\nabla\cdot\underline{u}=0 \tag{3.51}$$

for the hydrodynamic pressure correction q rather than the complete Poisson equation. The principle purpose of T_x is that, once convergence is obtained, its precise formulation is irrelevant provided the horizontal orbital momentum equation is added to the mean horizontal momentum equation (2.1). This addition eliminates T_x but the true mean Eulerian velocity is $U(z)+\overline{\tilde{u}}(z)$ rather than just U(z).

4 Turbulence closure

4.1 High-pass filter function for wave-turbulence interaction

Laboratory experiments of Jiang et al. (1990) with wind-driven surface waves over a turbulent flow have shown marginal wave-turbulence interaction. Therefore, the inclusion of the full eddy viscosity in the closure for the stress tensor of (2.2) would overestimate significantly the orbital Reynolds stresses and likewise the turbulence production by orbital shear rates in most of the fluid volume. On the other hand, however, there is notable turbulence production in the boundary layer so that neglecting wave-turbulence interaction is not correct for the entire fluid volume.

Therefore, this section considers a simple model for determining the high-pass filter function f_{hp} that was introduced in (3.13) and (3.22). This function represents the response of sufficiently-fast turbulence to orbital shear rates with angular frequency ω. Note that in the experiments of Klopman (1994) the horizontal wave length is about five times the water depth. Therefore, all major energy containing turbulence wave lengths are sufficiently short for interacting with the imposed spatial variations in orbital shear rate. Consequently, in this particular case, the problem of wave-turbulence interaction reduces to modelling just the turbulence response in frequency domain and the corresponding high-pass filter is constructed as follows. In the more general case, the high-pass filter function should also include the separation of turbulent shear stress in wave number space.

First, the frequency spectrum of Lagrangian turbulent velocity is estimated. From this spectrum, the fraction of turbulent kinetic energy with minimal frequency ω is estimated and ω is the angular frequency of the surface wave. The formation of orbital Reynolds stresses is set proportional to this energy fraction as well as the reduced time scale and the product of the latter two defines the high-pass filter function f_{hp}.

The frequency spectrum of Lagrangian turbulent velocity is derived as follows. The (Lagrangian) position $\underline{X}$ of a fluid parcel, starting at Eulerian position $\underline{x}$ at time t is defined formally by

$$\underline{X}(0) = \underline{x}: \quad \frac{d\,\underline{X}(\tau)}{d\tau} = \underline{u}(\underline{X}, t+\tau) \quad , \tag{4.1}$$

with total derivative $d/d\tau$ with respect to flight time τ of the fluid parcel starting at $\underline{x}$ and $\underline{u}$ is the total velocity of the fluid. The Lagrangian autocorrelation coefficient ρ_{uu} for a single velocity component is then defined by (Tennekes and Lumley, 1972, eq. 7.1.4)

$$\rho_{uu}(\tau;\underline{x},t) = \frac{\left\langle u'(\underline{x},t)u'(\underline{X},t+\tau)\right\rangle}{\left\langle u'^2(\underline{x},t)\right\rangle} \quad . \tag{4.2}$$

The brackets <..> imply ensemble averaging over turbulence; the variables after the semicolon in (4.2) are considered as parameters. If turbulence is superimposed on a time-varying mean flow then the formalism of turbulence with stationary increments could be introduced, see (Monin and Yaglom, 1975, part II, sec. 13.1). For turbulence in a wave-affected flow, the procedure would be to define turbulence superimposed on a mean flow that is locally linearized in time, i.e. turbulence with stationary first increments, and by applying phase averaging as the appropriate ensemble-averaging operation. Nevertheless, the consequences for the design of the following simple model for the high-pass filter function f_{hp} are equivalent to the following considerations for stationary turbulence.

For stationary turbulence, the definition of the so-called integral Lagrangian time scale reads (Tennekes and Lumley, 1972, eq. 2.3.17):

$$\tau_L = \int_0^\infty \rho_{uu}(\tau)\, d\tau \quad . \tag{4.3}$$

The derivation of eddy diffusivity Γ_T then yields (Tennekes and Lumley, 1972, eq. 7.1.14):

$$\Gamma_T = \lim_{\tau\to\infty} \frac{d\,\frac{1}{2}\left\langle X'^2(\tau)\right\rangle}{d\,\tau} = \left\langle u'^2(\underline{x},t)\right\rangle \tau_L \tag{4.4}$$

and the usual closure assumption is that eddy viscosity is proportional to Γ_T, the coefficient of proportionality is about unity and it is called the turbulence Prandtl/Schmidt number, see e.g. (Rodi, 1984).

Here the interest is on eddy viscosity related to the orbital Reynolds stresses due to turbulence with angular frequency ω or larger. The high-pass filter function is now defined as:

$$f_{hp}(\omega) \equiv \frac{\Gamma_T(\omega)}{\Gamma_T(0)} \tag{4.5}$$

with $\Upsilon_T(\omega)$ the eddy diffusivity of turbulent motions responding to shear rates imposed at angular frequency ω. Consequently, according to (4.4) and (4.5), two estimates should be made for defining the high-pass function. The first estimate concerns the variance $\left\langle u'^2(\omega)\right\rangle$ of turbulent motions with angular frequency exceeding ω. The second and last estimate is the Lagrangian time scale of the high-pass filtered turbulent motions.

The first estimate thus concerns the ratio in velocity variances. Experiments by Kato and Yamamoto (1987) have shown the following approximation to the Lagrangian autocorrelation coefficient (4.2):

$$\rho_{uu}(\tau) = \exp(-\tau/\tau_L) \quad . \tag{4.6}$$

The corresponding (normalised) energy spectrum $E_{uu}(\omega')$ follows from the cosines transform (Hinze, 1975, eq. 1-95a) of (4.6) and it yields:

$$E_{uu}(\omega') = \frac{2}{\pi}\frac{\tau_L}{1+(\omega'\tau_L)^2} \quad ; \quad \int_0^\infty E_{uu}(\omega')\,d\omega' = 1 \tag{4.7}$$

so that the ratio of velocity variances becomes

$$\frac{\langle u'^2(\omega)\rangle}{\langle u'^2(0)\rangle} \equiv \int_\omega^\infty E_{uu}(\omega')\,d\omega' = 1 - \tfrac{2}{\pi}\arctan(\omega\,\tau_L) \tag{4.8}$$

and this defines the first estimate.

The second estimate concerns the equivalent time scale of the high-pass filtered turbulence with corrected Lagrangian correlation function:

$$\tau_L(\omega) = \int_0^\infty \rho_{uu}(\tau;\omega)\,d\tau \quad . \tag{4.9}$$

where ω after the semicolon of the autocorrelation coefficient refers to the high-pass filtering operation on turbulence. In (4.8) appears the product $(\omega\tau_L)$ i.e. ω is inversely connected to the integral time scale. This relation connects the inverse of angular frequency (or wave number) to integral time scale (or length scale) i.e. disregarding the 2π for conversion to period or wave length. The equivalency between integral time scale and the inverse of appropriate angular frequency is typical for turbulence processes, see (Hinze, 1975, chapter 3) for examples. Therefore, (4.9) is approximated by

$$\tau_L(\omega) = \int_0^{\omega^{-1}} \rho_{uu}(\tau)\,d\tau \quad , \tag{4.10}$$

where ω^{-1} represents the upper limit of time scales of turbulence that responds to oscillations with angular frequency ω. Consequently, the estimate for the ratio in integral time scales reads:

$$\frac{\tau_L(\omega)}{\tau_L(0)} = 1 - \exp\left\{-(\omega\,\tau_L)^{-1}\right\} \quad . \tag{4.11}$$

Combining (4.8) and (4.11) in (4.4) for determining the ratio (4.5) yields the high-pass filter function:

$$f_{hp} = \left\{1 - \tfrac{2}{\pi}\arctan(\omega\,\tau_L)\right\}\left\{1 - \exp\left[-(\omega\,\tau_L)^{-1}\right]\right\} \quad . \tag{4.12}$$

which, of course, becomes unity for vanishing integral time scale τ_L i.e. when the turbulence is very fast compared to the oscillations in the imposed shear rates. Figure 1

presents the properties of the previous functions and particularly the lower graph for f_{hp} can be used to estimated the thickness of the wave-induced turbulent boundary layer above a rough bed for an estimated profile of $\tau_L(z)$.

Finally, before closing this section, an estimate for the integral Lagrangian time scale proper should be made. As presented in the next section, an eddy viscosity/diffusivity model will be applied. Practically all such turbulence models are based on some analytical expression or transport equation for the turbulent kinetic energy q^2 ; note that q^2 is used here rather than k for avoiding confusion with wave number. Most eddy-viscosity type turbulence models are tuned for estimating the exchange of streamwise momentum or mass in the direction normal to the wall, in the present case that is the vertical direction. The relevant eddy diffusivity then is based on the vertical velocity variance, so from its definition (2.5.4), the integral time scale is expressed in turbulence model variables through

$$\tau_L = \frac{\Gamma_T}{|w'|^2} \quad ; \quad \Gamma_T = \frac{\upsilon_T}{\sigma_T} \quad ; \quad |w'|^2 = \alpha q^2 \quad ; \quad q^2 = \tfrac{1}{2}\langle \underline{u}' \cdot \underline{u}' \rangle \quad , \tag{4.13}$$

with empirical coefficient $\alpha \approx 0.25$ for turbulent channel flow, see e.g. (Nezu and Rodi, 1986, fig. 12 and 13) and turbulent Prandtl/Schmidt number $\sigma_T \approx 0.7$. Whether α is wave dependent is not investigated yet. With coefficient α and the turbulent kinetic energy q^2 estimated by the turbulence model, the integral time scale τ_L follows from (4.13) and with the given angular of the surface waves, the high-pass filter function is known at every level. Sufficiently close to a rigid wall, the eddy diffusivity is proportional with wall distance where q^2 is large and nearly constant, see e.g. (Nezu and Rodi, 1986). Consequently, the integral time scale τ_L is proportional with wall distance. The consequence is that practically all energy containing length scales of the fast near-wall turbulence respond to the imposed orbital shear rates with angular frequency ω and so f_{hp} tends to unity and that corresponds to $\tau_L \approx 0$ in (4.12). Therefore, $f_{hp}=1$ has been used in the boundary condition (3.44) for orbital horizontal velocity.

The simple high-pass filter function is devoted to the special case of simulating the experiments of Klopman (1994) i.e. with wave length of surface waves exceeding the water depth significantly. In case of short waves on deep water the truncation in wave number space should also be included in the filter function. The extension of f_{hp} for truncation of turbulence shear stress in wave number space is possible provided the form of the cross spectrum $G_{uw}(k)$ based on turbulent velocity components u' and w' as a function of horizontal wave number magnitude k is known. An estimate for $G_{uw}(k)$ could follow from on observations in wave-induced boundary layers and using the decomposition procedure of (Jiang et al., 1990).

Before presenting the turbulence model in the next section, the turbulence production by orbital motions is considered here. The turbulence production is a source term in the transport equation for turbulent kinetic energy. The exact expression for production P_k of turbulent kinetic energy reads:

$$P_k = r_{ij} d_{ij} \quad ; \quad r_{ij} = -\left\langle u_i' u_j' \right\rangle \quad ; \quad d_{ij} = \tfrac{1}{2}\left(\frac{\partial \left\langle u_i \right\rangle}{\partial x_j} + \frac{\partial \left\langle u_j \right\rangle}{\partial x_i} \right) \tag{4.14}$$

with Reynolds stress tensor r_{ij}, rate-of-deformation tensor d_{ij} and <..> represents ensemble-averaging. In case of phase-averaging, e.g. with surface-wave elevation as reference signal, the tensors in (4.14) can be decomposed into mean (written in capitals) and orbital components:

$$r_{ij} = R_{ij} + \tilde{r}_{ij} \quad ; \quad d_{ij} = D_{ij} + \tilde{d}_{ij} \quad . \tag{4.15}$$

For instance, Jiang et al. (1990) applied such a decomposition procedure to turbulence and surface waves.

The application of the well-known eddy-viscosity closure for expressing the deviatoric wave-induced Reynolds stresses into the orbital shear rates then yields for the turbulence production:

$$P_k = 2\upsilon_T \left(D_{ij} D_{ij} + f_{hp} \tilde{d}_{ij} \tilde{d}_{ij} \right) \tag{4.16}$$

and in wave-averaging P_k it is understood that f_{hp} is independent of wave phase i.e. f_{hp} refers to wave-averaged turbulence properties rather than wave-related modulations of the integral time scale.

4.2 Turbulence model

The standard DPM is equipped with the k-ε turbulence model and the quasi-equilibrium level 2.5 Mellor-Yamada model which are the prominent models in large-scale civil engineering simulations. The application of these models in the WCI problem showed no difficulties. For the purpose of comparing the results of the hydrodynamic performance of the adapted DPM with (Groeneweg and Klopman, 1998), the k-L turbulence model they applied is used here as well. For sake of completeness of notation our versions of the k-L and k-ε turbulence models as implemented in the DPM read as follows.

The generic equation for Turbulent Kinetic Energy (TKE) reads:

$$\frac{\partial k}{\partial t} = \frac{\partial}{\partial z}\left\{ \left(\upsilon + \upsilon_T / \sigma_k \right) \frac{\partial k}{\partial z} \right\} + P_k - \varepsilon - B_k \tag{4.17}$$

Table 4.1 presents closure of (4.17) for the k-L and the k-ε turbulence model.

		k-L model	k-ε model
turbulence production	P_k	see (4.16)	see (4.16)
dissipation rate	ε	$\varepsilon = c_D k^{3/2} / L$	see (4.18)
buoyancy flux	B_k	$\upsilon_T / \sigma_\rho N^2$	$\upsilon_T / \sigma_\rho N^2$
eddy viscosity	ν_T	$c_\mu' L\sqrt{k}$	$c_\mu k^2 / \varepsilon$

Table 4.1. Definition and closures for terms in k-L and k-ε turbulence models

The k-ε turbulence model is a two-equation model with the following equation for energy dissipation rate ε:

$$\frac{\partial \varepsilon}{\partial t} = \frac{\partial}{\partial z}\left\{\left(\upsilon + \upsilon_T / \sigma_\varepsilon\right)\frac{\partial \varepsilon}{\partial z}\right\} + \frac{\varepsilon}{k}\left(c_{1\varepsilon} P_k - c_{2\varepsilon}\varepsilon - c_{3\varepsilon} B_k\right) \tag{4.18}$$

Our version of the k-L model is closed with the flow-independent mixing length L:

$$L = \kappa\left(9 z_0 + z\right)\sqrt{1 - \frac{9 z_0 + z}{\bar{\zeta} + z_a}} \tag{4.19}$$

which, in principle, is the Bakhmetev profile but with some correction for the length scale at the mean water level and at the bed. For boundary conditions on a hydraulically rough bed we refer to Appendix C.
The last term B_k in (4.17) the buoyancy flux which represents the conversion of turbulent kinetic energy to mean potential energy or vice versa. In (4.17) appears the so-called buoyancy frequency N^2 (see Table 4.1):

$$N^2 = -\frac{g}{\rho}\frac{\partial \rho}{\partial z} \quad . \tag{4.20}$$

and the turbulence Prandtl/Schmidt number $\sigma_\rho \approx 0.7$ for conversion of eddy viscosity into eddy diffusivity. We refer to Chapter 6 for the formulation of the total, fluid and sediment, density that is assumed to damp turbulence as if the fluid was stably stratified by salt or temperature.

In (4.17) and (4.18) P_k is the turbulence production term that is extended here by wave-turbulence interaction according to (4.16).

κ	0.41
σ_ρ	0.7
σ_k	1.0
σ_ε	1.3
c_μ	0.09
c_μ'	0.54
c_D	0.156
$c_{1\varepsilon}$	1.44
$c_{2\varepsilon}$	1.92
$c_{3\varepsilon}$	0 $N^2>0$
$c_{3\varepsilon}$	1 $N^2<0$
z_a	1 [mm]

Table 4.2. Coefficients used in the k-L and k-ε turbulence models.

In (4.19), κ is the Von Kármán constant ($\kappa \approx 0.41$), z_0 the roughness length, similar to the one used in bed friction (3.45), and z_a is some off-set or surface-roughness length scale that Groeneweg and Klopman (1998) introduced for maintaining a non-zero L at the free surface; they took z_a = 1 mm. In (4.19), z=0 is considered to be the mean bed level and $z=\overline{\zeta}$ the mean level of the water surface. The coefficients σ_k=1.0, $c_\mu' = 0.54$ and $c_D = 0.156$ are adopted from (Groeneweg and Klopman, 1998) but the addition of kinematic viscosity in (4.17) for diffusion is not applied by them.

Presently in the DPM, vertical advection by the mean and orbital flow is neglected but may be implemented in the same conservative approach as for sediment, see Chapter 6. Equation (4.17) is discretized on the same grid as for the momentum and pressure equations but with k and υ_T on cell interfaces. At the bed and mean water surface (without wind forcing) the vertical diffusion of turbulent kinetic energy is zero. On the bed a usual boundary condition for high-Reynolds turbulence models is imposed, see Appendix C, with reference to velocity defined in the centre of the bed cell (*kmax*) at the previous time step.

For the mean velocity, the time reference is the start time of the inner loop of solving orbital motions. The boundary condition for k differs from the one imposed in (Groeneweg and Klopman, 1998) because they applied a no-slip condition for velocity and expressed u_* in the vertical gradient of horizontal velocity. The application by Groeneweg and Klopman (1998) of the no-slip boundary condition is not in accordance with the high-Reynolds turbulence model (4.17). The no-slip condition should be applied with a low-Reynolds turbulence model that accounts for the direct damping of turbulence by molecular viscosity. Another problem of using the no-slip condition as well as low-Reynolds turbulence model for flows near hydraulically-rough bed is the existence of a viscous sublayer with typical thickness a few times larger than the size of the sand grains that form the bed roughness. The neglect of the viscous effects very close to the bed is in accordance with the following procedure. The application of the high-Reynolds turbulence closures, such as (4.17), can be regarded from the viewpoint of asymptotic expansion theory with

$$z^+ = \frac{u_* z}{\upsilon} \tag{4.21}$$

as scaling parameter. Note that z^+ is a local Reynolds number. The inner solution holds for small z^+ and covers the z-interval with dominant viscous effects on turbulence. Conversely, the outer solution is dedicated to large z^+ and this is the range of application of high-Reynolds turbulence models. In this asymptotic expansion, the outer solution should match the inner solution and, as usual in this theory, the matching conditions for the outer solution are imposed on $z^+=0$. Appendix C gives the matching conditions for the (high-Reynolds) outer solution, see e.g. (Van Dyke, 1975, eq. 7.7b).

The diffusion term in the turbulence equation (4.17) Euler-implicit time integrated, P_k is integrated explicit and in the last so-called energy-dissipation term, $k^{3/2}$ is written as a product of old and new time level and it is integrated implicitly. This numerical solution ensures positive k and consequently no truncation on k is applied. The k-L model is solved at each inner-loop time step using the solution of the orbital motions at the new inner-loop time level. All components entering the double contraction $\tilde{d}_{ij}\tilde{d}_{ij}$ in (4.16) of the wave-related strain-rate tensor are evaluated but the horizontal gradients are derived from temporal derivatives, according to (2.4).

5 The mean velocity profile and mean flow rate

After completion of simulating the orbital motions and turbulence properties in the inner loop, the momentum equation (2.1)

$$\frac{\partial U}{\partial t}+\frac{\partial P}{\partial x}=\frac{\partial}{\partial z}\left\{\left(\upsilon+\upsilon_T\right)\frac{\partial U}{\partial z}\right\}-T_x$$

for the mean horizontal velocity is solved with a time step equal to the wave period. The solution procedure is the one employed in the original DPM with WCI force T_x integrated explicitly. The eddy-viscosity in (2.1) equals the eddy viscosity obtained by solving the q^2-L turbulence model (Section 4.2) up to the last time step in the inner loop. The boundary condition on the mean water surface equals (3.20) which is derived from time-averaging the stress-free condition with surface waves. The standard boundary condition on the bed is due to a logarithmic profile using the roughness length scale z_0 without corrections for wave-orbital motions. The DPM, however, is equipped with the Grant&Madsen formulation for increasing z_0 due to orbital motions.

The standard procedure in the DPM is adopted for estimating the horizontal pressure gradient such that the depth-averaged horizontal velocity U_0 is obtained and U_0 is user-prescribed. In the experiments (Klopman, 1994), the total flow rate in the facility is constant and it is determined by a pump recirculating the water in the flume so that U_0 then represents the flow rate averaged, over any cross section of the flume between the flow-inlet and flow-exit sections. In case of waves in the facility, the depth-integrated Stokes drift yields an additional flux in the direction of wave propagation.

In the numerical simulations using the extended DPM, the following three fluxes are involved in obtaining the imposed depth-averaged velocity U_0:

- The depth average of U(z) being the solution of (2.1);
- The depth average of Stokes drift $U_S(z)$;
- The depth average of $\overline{\tilde{u}}(z)$, being $\tilde{u}(z,t)$ averaged over the previous wave period.

At the end of Section 3.3, the role of force T_x is explained in conjunction with the addition of the horizontal orbital momentum equation (3.22) to the mean (wave-averaged) horizontal momentum equation (2.1). Conceptually, the essential point is the elimination of T_x in conjunction with a non-zero wave-averaged horizontal orbital velocity $\overline{\tilde{u}}(z)$, defined by (3.27). The total mean velocity then reads $U(z)+\overline{\tilde{u}}(z)$ rather than just U(z).

For WCI, the procedure for adjusting the horizontal pressure gradient is extended by including the wave-related mass flux, or equivalently depth-integrated Stokes drift, and the new formulation reads as follows:

$$\frac{\partial P}{\partial x} = \frac{\tau_{s,x} - \tau_{b,x}}{\overline{\zeta}} + \frac{U^{(\zeta)} + \overline{\widetilde{u}}^{(\zeta)} + U_S^{(\zeta)} - U_0}{T_{rlx}} \quad , \tag{5.1}$$

with depth-averaged velocity and depth-averaged Stokes drift defined by

$$U^{(\zeta)} = \frac{1}{\overline{\zeta}} \int_0^{\overline{\zeta}} U(z,t)\, dz \quad ; \quad \overline{\zeta} U_S^{(\zeta)} = \overline{\widetilde{\zeta}\, \widetilde{u}(\overline{\zeta})} + \tfrac{1}{2} \overline{\widetilde{\zeta}^2} \left. \frac{\partial U}{\partial z} \right|_{\overline{\zeta}} \quad , \tag{5.2}$$

for the latter see (Van Kester et al, 1996). Likewise, the depth-average of $\overline{\widetilde{u}}(z)$ is defined by

$$\overline{\widetilde{u}}^{(\zeta)} = \frac{1}{\overline{\zeta}} \int_0^{\overline{\zeta}} \overline{\widetilde{u}}(z)\, dz \quad ; \quad \overline{\widetilde{u}}(z) = \frac{1}{T} \int_{lT}^{(l+1)T} \widetilde{u}(z,t)\, dt \quad . \tag{5.3}$$

In (5.1), $\tau_{b,x}$ is the bed shear stress and $\tau_{s,x}$ the surface shear stress, both divided by fluid density. The shear stress $\tau_{s,x}$ is used here for imposing the condition (3.20) for a stress-free boundary with waves. In (5.1), T_{rlx} is a relaxation time which is set to twice the time step of solving (2.1) i.e. twice the wave period and this choice is standard for the original DPM. The RHS of the depth-integrated Stokes drift in (5.2) is due to averaging over the inner-loop solutions of the last wave period. Similarly, force T_x defined by (3.27), is evaluated over the inner-loop solutions in the previous wave period.

The solution of the mean flow profile according to (2.1) is used in the next inner loop for solving the hydrodynamic pressure, vertical and horizontal orbital velocity and q^2-L turbulence model in the inner loop. This closes the set of equations.

6 Sediment distribution model

6.1 Advection-diffusion equation

We apply the following advection-diffusion equation for the mass concentration $c^{(k)}$ of sediment fraction (k=1,2,..):

$$\frac{\partial c^{(k)}}{\partial t} + \nabla \cdot \left(\underline{u}_c^{(k)} c^{(k)} \right) = \frac{\partial}{\partial z} \left[\left(\upsilon + \frac{\upsilon_T}{\sigma_T^{(k)}} \right) \frac{\partial c^{(k)}}{\partial z} \right] \quad , \tag{6.1}$$

using the mean velocity

$$\underline{u}_c^{(k)} = \underline{\tilde{u}} + w_s^{(k)} \frac{\underline{g}}{g} \quad . \tag{6.2}$$

that is the particle velocity averaged over a sufficiently small volume still containing a sufficiently large number of particles for defining this mean velocity vector. The first term in the RHS of (6.3) represents the orbital velocity of all spectral components. The horizontal orbital velocity component in (6.2) is the solution of the horizontal momentum equation (3.30). The vertical orbital velocity component, however, is derived from the incompressibility condition rather than from its momentum equation. This inconsistency is motivated by mass conservation and this argument is clarified in Section 6.3.
By (6.2) we implicitly assume that the mean flow is horizontal and that it does not vary in horizontal direction. The last term in (6.2) is the fall velocity, specified below for sand. The orbital velocity consists of the horizontal as well as vertical orbital component. In (6.1) just the vertical diffusion is included. In (6.1), the eddy diffusivity is defined through the eddy viscosity υ_T divided by σ_T, the turbulence Prandtl/Schmidt number. Typically, $\sigma_T \approx 0.7$ holds and this corresponds to the multiplication factor $\beta \approx 1.4$ used in sand transport literature. The Prandtl/Schmidt number is a user-defined parameter and can be specified per sediment fraction (k).
Implicitly, we assumed in (6.1) that the particle response time (Stokes time) is sufficiently small so that all temporal and spatial variations in eddy diffusivity are transferred to particle diffusion. In other words, in (6.1) we do not apply the high-pass filter function that was introduced in Chapter 4 for the possibly reduced response of turbulent eddies to the straining action of the orbital motions.

Appendix D describes that the user can select more than one sediment fraction e.g. with different grain diameter and mass density. For simplicity in notation in the remaining text, however, we omit the superscript (k) for sediment fraction unless required.

The fall velocity of the sediment w_s is computed according to Van Rijn (1993) but reduced by hindered settling (see Eqs 8.2 and 8.3 in Bosboom et al., 1997, Unibest-TC manual). The fall velocity $w_{s,0}$ of a single particle in infinite fluid, without wall effects, reads (Van Rijn, 1983):

$$\begin{aligned} w_{s,0} &= \frac{\Delta g d_s^2}{18\nu} && , \quad 1\mu m < d_s \le 100\mu m \\ w_{s,0} &= \frac{10\nu}{d_s}\left[\left(1+\frac{0.01\Delta g d_s^3}{\nu^2}\right)^{1/2}-1\right] && , \quad 100\mu m < d_s \le 1000\mu m \\ w_{s,0} &= 1.1\left(\Delta g d_s\right)^{1/2} && , \quad 1000\ \mu m < d_s \end{aligned} \tag{6.4}$$

Here d_s is the diameter of the suspended sediment, which is a user-defined property. Van Rijn (1987) concluded, on the basis of measurements, that d_s should be in the range of 60 to 100% of the diameter of the median bed material size d_{50}. In the current version of the POINT-SAND model, d_s is set equal to d_{50}. A user-defined d_s will be implemented in a later stage.

In high concentration mixtures, the fall velocity of a single particle is reduced by the flow as well as fluid stresses induced by other particles. Following Richardson & Zaki (1954) we use:

$$w_s = \left(1-\frac{\phi}{\phi_s}\right)^5 w_{s,0} \tag{6.5}$$

with $w_{s,0}$ defined by (6.4) and where ϕ is the volume fraction of the all suspended sediment i.e.

$$\phi = \sum_k \frac{c^{(k)}}{\rho_s^{(k)}} \tag{6.6}$$

Further, $\phi_s = 0.65$ is taken as the maximum volume fraction of solids in a non-cohesive porous bed. Notice that (6.6) makes the reduced fall velocity depth and time-dependent.

6.2 Boundary conditions

Equation (6.1) is subjected to the boundary conditions of zero flux at the mean water surface and a specified time-dependent boundary condition at a reference level close to the bottom. Presently, the user can choose between the following two generic forms for the boundary condition based on reference concentration.

The first boundary condition prescribes the sediment concentration at a certain reference level z_a :

$$c(z_a, t) = c_b(t) \quad , \tag{6.7}$$

or reformulated in terms of a pick-up function:

$$w_s c_b(t) + (\nu + \nu_T / \sigma_T) \left. \frac{\partial c}{\partial z} \right|_{z=z_a} = 0 \quad . \tag{6.8}$$

The reference level z_a must correspond to the prescription of the bed-reference concentration c_b. Presently, we implemented the formulation of Zyserman and Fredsøe (1994) for the mass concentration $c_b(t)$:

$$c_b(t) = \frac{0.331(\theta - \theta_c)^{1.75}}{1 + \frac{0.331}{C_m}(\theta - \theta_c)^{1.75}} \quad \text{at} \quad z_a = 2 d_{50} \quad . \tag{6.9}$$

In (6.9), the maximum concentration C_m has a value of 0.32. Further, in (6.9), θ is the Shields parameter defined by

$$\theta = \frac{{u_{*b}}^2}{(s-1) g d_{50}} \quad ; \quad s = \frac{\rho_s}{\rho_w} \quad , \tag{6.10}$$

with s the relative sediment density and u_* the total instantaneous shear velocity

$${u_{*b}}^2 = f_{hp} \nu_T \left. \frac{\partial u}{\partial z} \right|_{z=0} \tag{6.11}$$

as determined by the hydrodynamic module. Note that $f_{hp} = 1$ holds at the bed because of the small and rapid turbulent eddies. The computation of the bed-shear velocity (6.11) is treated in detail in Appendix C.

Finally, in (6.9), θ_c is the critical Shield's parameter and Van Rijn (1993) proposes the following piecewise representation of the Shields curve:

$$\begin{aligned}
\theta_c &= 0.24 \; D_*^{-1} \quad , \quad 1 < D_* \leq 4 \\
\theta_c &= 0.14 \; D_*^{-0.64} \quad , \quad 4 < D_* \leq 10 \\
\theta_c &= 0.04 \; D_*^{-0.1} \quad , \quad 10 < D_* \leq 20 \\
\theta_c &= 0.013 \; D_*^{0.29} \quad , \quad 20 < D_* \leq 150 \\
\theta_c &= 0.055 \quad , \quad 150 < D_*
\end{aligned} \tag{6.12}$$

with the dimensionless grain diameter D_*:

$$D_* = d_{50}\left(\frac{(s-1)g}{\nu^2}\right)^{1/3} \quad . \tag{6.13}$$

Upward mixing of suspended sediment involves the conversion of Turbulent Kinetic Energy of the fluid into an increasing potential energy of the sediment. The latter is subsequently destroyed by viscous drag while the particles settle. The rate of conversion of TKE into the sediment's potential energy is called buoyancy flux. The latter is included in the implemented k-L and k-ε turbulence models by assuming the analogy between sediment-laden flows and flows with density stratification through temperature or salt. Accordingly, the buoyancy flux for the sediment is then estimated by the total fluid-sediment density ρ defined as:

$$\rho = \rho_w + \sum_k \left(1 - \frac{\rho_w}{\rho_s^{(k)}}\right) c^{(k)} \tag{6.14}$$

In (6.14), ρ_w represents the density of pure water and this density is determined by its temperature and salinity, the latter are specified by the user.

Note that in an oscillatory flow and at the instant of zero bed stress (flow reversal), (6.8) may yield a positive concentration $c(z_a)$ whereas (6.7) prescribes a zero concentration. The latter may induce a decreasing concentration towards the bed i.e. an unstable density stratification which then produces TKE rather than consumes TKE.

6.3 Mass conservation and inconsistency with dynamical equations for orbital motions

The horizontal advection by orbital motions in (6.1) needs careful attention for satisfying the conservation of sediment mass in an incompressible fluid. The previous aspect is considered in this section.

We start with (6.1) for a constant sediment mass concentration, whence:

$$\frac{\partial \tilde{u}}{\partial x} + \frac{\partial \tilde{v}}{\partial y} + \frac{\partial \tilde{w}}{\partial z} = 0 \tag{6.15}$$

This well-known requirement is not guaranteed by the solution of the vertical momentum equation (3.21) even though the hydrodynamic pressure solution was formulated using (6.15) in conjunction with the linearized momentum equations, see Section 3.1. Moreover, the free-surface conditions for the momentum equations are prescribed at the (time-averaged) mean-water level rather than at the momentary water level $z=\zeta(t)$.

In other words, there is an inconsistency in the solution of the dynamic equations in Chapter 3 with respect to incompressibility. We regard this inconsistency not serious for the simulation of WCI proper and we refer to the discussion in Section 3.2 about the preference of solving the vertical momentum equation rather than satisfying (6.15).

For correctly modelling horizontal and vertical sediment transport, the incompressibility condition (6.15) and its intimate relation to the advection-diffusion equation (6.1) is essential. Consequently, for satisfying mass conservation we derive the vertical orbital velocity for sediment transport from (6.15) rather than from the vertical momentum equation. This is the inconsistency announced in the title of this section.

We define $\tilde{w}_c$ as the vertical orbital velocity component that satisfies (6.15) formulated now as follows:

$$\frac{\partial \tilde{w}_c}{\partial z} + \sum_n \frac{\partial \tilde{u}(x,y,z,t;\omega_n)}{\partial x} + \frac{\partial \tilde{v}(x,y,z,t;\omega_n)}{\partial y} = 0 \tag{6.16}$$

with summation over all spectral components (n=1,2,3...) related to the user-specified angular frequencies ω_n. The horizontal derivatives in (6.16) are converted to time derivatives through two steps that were introduced with reference to (3.28) and to Appendix B. The latter demonstrates that, by excellent approximation, the orbital velocity vector is in the vertical plane containing the wave number $\underline{k}(\omega_n)$. The latter simplifies (6.16) to

$$\frac{\partial \tilde{w}_c}{\partial z} + \sum_n \frac{\partial \tilde{u}(z,t;\omega_n)}{\partial x_k} = 0 \quad , \tag{6.17}$$

with x_k the horizontal co-ordinate parallel to $\underline{k}(\omega_n)$. Subsequently, we adopted in Section 2.3 the periodicity assumption which converts (6.17) into

$$\frac{\partial \tilde{w}_c}{\partial z} = \sum_n \frac{k(\omega_n)}{\omega_n} \frac{\partial \tilde{u}(z,t;\omega_n)}{\partial t} \quad , \tag{6.18}$$

Integrating (6.18) from the bed level z=0 upwards yields the vertical orbital velocity component in accordance with the incompressibility condition:

$$\tilde{w}_c(z,t) = \sum_n \frac{k(\omega_n)}{\omega_n} \int_{z'=0}^{z} \frac{\partial \tilde{u}(z',t;\omega_n)}{\partial t} dz' \quad . \tag{6.19}$$

The vertical orbital velocity, as defined by (6.19), is used in the advection term of (6.1) and the latter reads now:

$$\frac{\partial c^{(k)}}{\partial t} + \nabla \cdot \left(\underline{u}_c^{(k)} c^{(k)} \right) = \frac{\partial}{\partial t} \left\{ \left(1 - \tilde{u}_a \right) c^{(k)} \right\} + \frac{\partial}{\partial z} \left\{ \left(\tilde{w}_c - w_s^{(k)} \right) c^{(k)} \right\} \tag{6.20}$$

with the dimensionless velocity $\tilde{u}_a$ defined by the summation over all spectral components (n=1,2,3...):

$$\tilde{u}_a = \sum_n \frac{k(\omega_n)}{\omega_n} \tilde{u}(z,t;\omega_n) \tag{6.21}$$

being the sum of the ratio between horizontal orbital velocity and celerity per spectral component.

Finally, all equations are solved up to the mean-water level $z = \bar{\zeta}$ and to ensure depth-integrated mass conservation we must impose the zero flux condition at the mean-water level i.e.

$$z = \bar{\zeta}: \quad \tilde{w}_c - w_s^{(k)} = 0 \quad . \tag{6.22}$$

If the sediment concentration is not zero near the mean water level and if the net vertical velocity is upward than (6.22) creates a blocking of vertical sediment transport and consequently an increase of sediment concentration in the top layer. The latter increase is not realistic, but it is our sacrifice to obey strict mass conservation. However, all sand transport remains in a comparatively thin wave-affected boundary layer so that the artificial blocking imposed by (6.22) is not observed in practice.

The next section presents the numerical implementation that ensures mass conservation.

6.4 Numerical implementation

The advection-diffusion equation (6.1) is discretized in a finite volume and mass conservative formulation. Notice that this equation is solved once in the *inner-time loop* after the solution of all spectral orbital components.

The vertical grid for sediment transport equals the grid for the numerical solution of the hydrodynamic and turbulence equations.

The horizontal mean and orbital velocity component as well as the mass concentration c(z,t) are defined in the centres of the grid boxes. The total vertical velocity component $\tilde{w}_c - w_s^{(k)}$, which includes the fall velocity $w_s^{(k)}$, as well as the turbulence fluxes are defined on the cell interfaces. The numerical integration (6.19) is based on the same spatial discretisation as for the advection diffusion equation and this discretisation guarantees mass conservation at the numerical representation.

The ceiling of the upper grid box corresponds to the mean water level. The definition of the lowest grid box depends on the selected boundary condition (6.7) or (6.8) and this definition is explained below.

For (6.7), the lowest computational grid box is defined as the box with its centre nearest to the level $z=z_a$ as defined by (6.9). For the pick-up formation (6.8), however, the lowest grid box has its bottom nearest to the level $z=z_a$ as defined by (6.9). In the code, the integer pointer to the lowest grid box is defined as KBED and, of course, KBED≤KMAX holds where KMAX is the user-specified number of grid boxes of the hydrodynamic and turbulence-model equations. Note that KBED depends on the grain diameter and KBED may thus vary between sediment fractions.

For extremely fine grids near the bed, it is possible that some grid boxes are excluded. Nevertheless, information on mass concentration must be know for the computation of:

- the horizontal sediment transport; and for
- the buoyancy flux using the total density defined by (6.14).

For these purposes we assume that

$$z \le z_a : \quad c(z,t) = c(z_a,t) \tag{6.23}$$

holds. Consequently, the advection diffusion equation (6.1) is thus solved for the grid boxes 1≤K≤KBED.

The vertical diffusion in (6.1) is formulated by the θ method although we recommend θ=1 i.e. Euler-implicit for avoiding wiggles. The diffusive flux at the upper interface of cell number k is based on the finite difference of c_{k-1} (one cell up) and the sediment concentration c_k of this cell. The eddy viscosity ν_T is defined at the cell interface. The diffusive flux is zero at the mean-water level and guarantees mass conservation in conjunction with (6.22).

The vertical advection in (6.20) reads

$$\frac{\partial}{\partial z}\left\{\left(\widetilde{w}_c - w_s^{(k)}\right)c^{(k)}\right\} \tag{6.24}$$

and there are numerous ways for its discretisation. We implemented the following implicit advection schemes:

- first-order upwind;
- second-order central scheme;
- third-order ADI upwind-central scheme.

For the user we made just the first-order up wind scheme available. This scheme is the single advection scheme that guarantees monotonicity i.e. positive sediment concentration and no internal formation of new maxima or wiggles. The disadvantage is that the first-order upwind scheme introduces numerical diffusion by the amount:

$$\tfrac{1}{2}\left|\widetilde{w}_c - w_s^{(k)}\right|\Delta z \tag{6.25}$$

with local cell height Δz. On the one hand, for large vertical orbital motions this artificial diffusion can be significant. On the other hand, in the wave-affected boundary layer the net vertical velocity in (6.25) remains of the order of the fall velocity.

Numerical experiments with zero fall velocity show that the third-order ADI scheme is the best of the three and creates minor over- and undershoots at very sharp sediment concentration jumps. The latter hardly occur in practice and on sufficiently fine grids. The third-order ADI scheme is computational much more involved than the first-order scheme. Compared to the effort in solving all the other momentum equation for the orbital motions as well as turbulence equations in the *inner-time loop,* the increase in computational effort is modest.

Therefore we recommend the final implementation of the bed-boundary conditions for the third-order ADI scheme in case of accurate estimation of sand transport with orbital motions.

Of course, in case of wave tunnel experiments all orbital velocity components in the previous considerations are set to zero and there is just vertical advection by the fall velocity. The first-order upwind scheme may then be the optimal choice.

7 Preliminary tests

7.1 Introduction

The tests reported in this Chapter were selected for a first diagnosis of the model. First, the full hydrodynamic module was tested against flume experiments. Secondly, the sediment transport model was tested against wave tunnel experiments. In order to do so, the model was run in wave tunnel mode, which means that the vertical velocities and the nonlinear advection terms are not taken into account. Those tests will therefore not yield any information on the importance of these new features of the model to the sediment transport predictions. It does however give information on the behaviour of the model compared to wave boundary layer models (see Davies et al, 1997) which neglect the vertical velocities and the nonlinear advection terms. At this stage in the development of the present model, the aim of the comparison with the wave-tunnel experiments is to test whether the new model is able to give results which are at least of the same quality as the results presented in Davies et al. (1997).

7.2 Wave-current interaction; the Scheldt flume

In order to verify the model a few preliminary tests were selected. A first diagnosis of the hydrodynamic module was performed on the basis of Scheldt flume experiments (Klopman, 1994). Only a short description of this diagnosis is given here.

Klopman performed tests with monochromatic, bi-chromatic and random waves without current, following the current and opposing the current. Also a test series was performed for a steady current without waves. It was found that the mean horizontal current profile under combined wave-current motion is strongly affected by the presence of waves not only inside but also outside the wave bottom boundary layer. In the upper half of the water column the velocity shear is reduced and may even change sign in the case of waves following the current. Waves opposing the current increase the velocity shear in the upper half of the water column.

The comparison between the simulation and the experiments for the monochromatic wave tests is shown in Figures 2 through 5. The results are obtained by simulating the wave-current interaction problem through alternatingly solving the orbital motions (inner-loop solution) and mean flow adjustment (outer-loop solution) as a function of time and depth. For Figure 2, 100 equidistant layers are used to compute the mean horizontal velocity profile. The agreement appears sufficiently close. The simulation converged quickly within maximal 50 wave periods and with 100 equidistant layers it requires 12 seconds on a standard 130 MHz PC in debugging mode of Salford FORTRAN while using 100 equidistant layers, 100 inner loop time steps and for a wave period of 1.44 s. The horizontal velocity amplitude profile for the monochromatic waves is shown in Figures 3 and 4 for the

situation of waves following and opposing the current, respectively. It can be seen that in both situations the velocity amplitude is somewhat underestimated by the model. The computed wave-current interaction force is shown in Figure 5. For the bichromatic wave tests only the results with following current are shown. Figure 6 shows the computed and measured horizontal velocity amplitude profiles for the first (upper right plot) and second component (upper left plot), for the subharmonic (lower left plot) and the mean velocity (lower right plot). The same information is given in Figures 7 through 9b. It can be seen that the results are fairly good, except for the subharmonic component which might be attributed to reflections in the flume.

7.3 Sand transport; the wave tunnel

7.3.1 Test cases

Model results regarding the sediment concentration are discussed for 2 oscillating wave tunnel experiments:

1. case C1: this is a case with asymmetrical waves. The following wave conditions were applied at a level of $z = 0.20$ m from the bed: $U(z = 0.2\text{ m}) = U_0 + U_1 \cos \omega t + U_2 \cos 2\omega t$, where $T = 2\pi/\omega = 6.5$ s and $U_0 = 0.025$ m/s; $U_1 = 0.845$ m/s and $U_2 = 0.265$ m/s. The d_{50} of the applied sediment was 210 μm. This case is comprehensively described in Al-Salem (1993).
2. case E1: this is a case with sinusoidal waves. The following wave conditions were applied at a level of $z = 0.075$ m from the bed: $U(z = 0.075\text{ m}) = U_0 + U_1 \cos \omega t$, where $T = 2\pi/\omega = 7.2$ s and $U_0 = 0.15$ m/s and $U_1 = 1.60$ m/s. The d_{50} of the applied sediment was 210 μm. This case is comprehensively described in Katopodi *et al*. (1994).

7.3.2 Input/output

The input files used for the calculations are INDPM.C1, TUN_C1.LVL, TUN_C1.VEL and WAVSPC.C1 for the C1-case and INDPM.E1, TUN_E1.LVL, TUN_E1.VEL and WAVSPC.E1 for the E1 case. These files can be found on the accompanying diskette. The input files are listed and discussed in Appendix D. The file INDPM.* is the main input file where parameters can be set regarding the grid schematisation, turbulence model, bed roughness and sediment properties, amongst others. In the file *.VEL the wave conditions are specified, whereas in the file *.LVL the water levels (this is a dummy file for the wave tunnel conditions). In WAVESPC.* the frequencies for harmonic analysis are specified. Note that the velocities specified are depth-averaged velocities. If the user wishes to set the velocity at a certain level, the depth-averaged velocity should be chosen such that the required velocity at the required level is realised. In a future version of the program, it will be possible to apply the velocity at a user-defined level.

The output files generated by the computer program are: OUTDPM.C1 and OUTSPC.C1 for the C1-case and OUTDPM.E1 and OUTSPC.E1 for the E1-case. The output file OUTDPM.* consists of the following items: first a copy of the input, subsequently the output at each time step specified. A description of the output files can be found in Appendix D.

Results of the harmonic analysis can be found in the file OUTSPC.*. All input files for the two cases discussed are stored on the accompanying diskette. Also the executable of the 1DV-program is stored there. The output files are not stored on the diskette due to limited disk space, but may easily be generated running the executable using the input files. Answer 'c1' or 'e1' to the question 'Give filename extension for files indpm and outdpm:'. If the program aborts abnormally, an error diagnosis message is written to the file OUTSPC.*.

7.3.3 Results

In Fig. 10 the time-averaged concentration profile is plotted for case E1. Comparison with measurements shows that the calculated concentration profile closely matches the measured one near the bed and at a level of a few centimetres above the bed. At intermediate heights the calculated concentration is too high. This is also the case for the upper part of the water column. The observed curvature of the concentration profile near the bed, which separates two distinct regions, may be attributed to turbulent kinetic energy damping by vertical gradients in suspended sediment concentration. This has to be further examined.

Sediment concentrations as a function of time at several levels for case E1 are plotted in Fig. 11. Moreover, for two levels (z=2.3 and z = 3.7 cm, Figs. 12 and 13) calculated profiles are compared with measured profiles. The calculated concentration at z=2.3 cm is much too high, whereas the concentration at z=3.7 is about right. Calculated and measured peaks during a wave cycle roughly coincide.

For case C1 (irregular waves) the calculated sediment concentration behaves approximately the same. In Fig. 14 the time-averaged concentration profile is plotted for case C1. Comparison with measurements again shows that the calculated concentration profile matches the measured one at a level of a few centimetres above the bed. In the lower and higher parts the calculated concentration is too high. Note that the results depend on the grid resolution: 500 layers result in a lower concentration than 100 layers, which suggest that full convergence has not yet been reached for 100 layers.

Sediment concentrations as a function of time at several levels for case C1 are plotted in Fig. 15. Moreover, for three levels (z=3.2, z=0.7 and z = 0.2 cm, Figs. 16, 17 and 18) calculated profiles are compared with measured profiles. The calculated concentration at z=0.7 cm is much too high, whereas the concentrations at z=3.2 and z=0.2 cm are about right. Calculated and measured peaks during a wave cycle roughly coincide.

In Fig. 19 the sediment flux is plotted as a function of z. Although the 1DV model does not perform worse than other models displayed in this figure, the measured reversal of sediment transport at about 2 cm above the bed is not reproduced. Moreover, the sediment flux near the bed appears to be too high.

7.4 Discussion and conclusions

It is mentioned that the preliminary tests described above are meant to compare the model with other models and experimental results present for wave tunnel conditions, where

vertical velocities are negligible. The full potential of the model is therefore not used here. The model can be applied to a much wider range of parameters than discussed here, but should not be used in the case of breaking waves or strong gradients in the direction of wave or current propagation.

First test results show that at the current level of development, the accuracy of the 1DV model results is comparable with those of other models such as discussed in Davies *et al.* (1997). This is not unexpected since for the idealised wave tunnel conditions, the underlying model equations reduce to equations similar as used in the wave boundary layer models described in Davies et al. (1997). At present the most important drawbacks are that the results are still rather strongly dependent on the chosen grid schematisation and that the near-bed concentrations are too high, which will be addressed during further development and testing.

At a later stage tests also validation tests should be performed which use the model's full potential. Such tests would include a comparison with laboratory measurements in a flume where wave forcing is applied with surface waves, which generate both horizontal and vertical velocities. Comparisons should also be made outside the sheet flow regime, as bed ripples are commonplace both in laboratory tests and in the field. The effect of ripples on bringing and keeping sediment in suspension and the implications for sediment transport model need further research. Strictly speaking, the formulations used in this report are only valid for flat beds. The knowledge of sediment transport above rippled beds is limited such that it is difficult to properly model a rippled bed situation. Due to this lack in knowledge, in coastal engineering practice today, models for flat bed situations are often applied to rippled bed situations, using an increased bed roughness related to the ripple dimensions.

Ideally, comparison should also be made with field experiments, although it may prove to be hard to obtain a data set with sufficiently accurate near-bed velocities and concentrations. The study of sediment transport in coastal conditions (combined waves and current) is rather problematic, especially since an important part of the sediment transport will occur in the near-bed region. No reliable instruments are available for measuring velocities and sediment concentrations in the field below, say 5 cm above the bed.

In the current β-release of the program distributed with this report the sediment transport subroutines do not yet work well with the subroutines solving the vertical velocity components. This may be due to the numerical schematization of the sediment transport formulations, which may also cause the observed dependence of the results on the grid schematization and the too high near bed sediment concentrations. Further model developments will be focussed on improvements regarding these inaccuracies.

References

AL-SALEM, A.A., 1993. Sediment transport in oscillatory boundary layers under sheet-flow conditions. Ph.D. thesis, Delft University of Technology.

BOSBOOM, J. & B. CLOIN, 1998. 1DV transport models. Report Z2529, WL|DELFT HYDRAULICS.

BOSBOOM, J., 1999. Analytical model for wave-related sediment transport. Report Z2733.42, WL|DELFT HYDRAULICS.

BOSBOOM, J., S.G.J. AARNINKHOF, A.J.H.M. RENIERS, J.A. ROELVINK & D.J.R. WALSTRA, 1997. Unibest-TC, Overview of model formulations. Report H2305.42, WL|DELFT HYDRAULICS.

CASULLI, V. & G.S. STELLING 1998 Numerical simulation of 3D quasi-hydrostatic free-surface flows. *J. Hydr. Engng.*, Vol. 124, No. 7, July, pp. 678-686.

DAVIES, A.G., J.S. RIBBERINK, A. TEMPERVILLE, J.A. ZYSERMAN, 1997. Comparisons between sediment transport models and observations made in wave and current flows above plane beds. Coastal Engineering 31 p163-198.

DELEERSNIJDER, E. & P. LUYTEN 1994 On the practical advantages of the quasi-equilibrium version of the Mellor and Yamada level 2.5 turbulence closure applied to marine modelling. *Appl. Math. Modelling*, vol. 18, May, pp. 281-287.

GALPERIN, B., L.H. KANTHA, S. HASID & A. ROSATI 1988 A quasi-equilibrium turbulent energy model for geophysical flows. *J. Atmos. Sc.*, vol. 45, no. 1, Jan., pp. 55-62.

GROENEWEG, J & G. KLOPMAN 1998 Changes of the mean velocity profiles in the combined wave-current motion described in a GLM formulation. *J. Fluid Mech.*, vol. 370, pp. 271-296.

HINZE, J.O. 1975 *Turbulence*. McGraw-Hill Classic Textbook Reissue Series.

JACKSON, P.S. 1981 On the displacement height in the logarithmic velocity profile. *J. Fluid Mech.*, vol. 111, pp. 15-25.

JIANG, J.-H., R.L. STREET & S.P. KLOTZ 1990 A study of wave-turbulence interaction by use of a non-linear water wave decomposition technique. *J. Geoph. Res.*, vol. 95, no. C9, Sept. 15, pp. 16,037-16,054.

KATOPODI, I., J.S. RIBBERINK, P. RUOL, R. KOELEWIJN, C. LODAHL, S. LONGO, A. CROSATO AND H. WALLACE, 1994. Intra-wave sediment transport in an oscillatory flow superimposed on a mean current. Data report H 1684.33, Part III, WL|DELFT HYDRAULICS.

KESTER, J.A.Th.M. Van, R.E. UITTENBOGAARD & M.W. DINGEMANS 1996 *3D wave-current interaction; CL vortex-force, simulation of wave-flume experiments*. WL|DELFT HYDRAULICS, report Z-751, Nov.

KESTER, J.A.Th.M. Van, R.E. UITTENBOGAARD & E.D. de GOEDE 1997 *Onderzoek naar numerieke modellering van thermocliene effecten in de Noordzee.* WL|DELFT HYDRAULICS, report Z2034.30, Ma2.

KITAIGORODSKII, S.A. & J.L. LUMLEY 1983 Wave-turbulence interaction in the upper ocean, I, The energy balance of the interacting fields of surface wind waves and wind-induced three-dimensional turbulence. *J. Phys. Oceanogr.*, vol. 13, pp. 1977-1987.

KLOPMAN, G. 1994 *Vertical structure of the flow due to waves and currents.* Progress rep., DELFT HYDRAULICS, H840.32, Part 2.

KRAICHNAN, R.H. 1956 Pressure fluctuations in turbulent flow over a flat plate. J. Acoustical Soc. America, vol. 28, no. 3, May, pp. 378-390.

MELLOR, G.L. & T. YAMADA 1982 Development of a turbulence closure model for geophysical fluid problems. *Rev. Geophys. Space Phys.*, vol. 20, no. 4, Nov., pp.851-875.

MONIN, A.S. & A.M. YAGLOM 1975 *Statistical fluid mechanics: mechanics of turbulence*. J.L. Lumley (ed.), vol. 2, MIT Press.

NEZU, I. & W. RODI 1986 Open-channel flow measurements with a Laser-Doppler Anemometer. *J. Hydr. Engng.*, vol. 110, no. 11, pp. 1613-1641.

PEYRET, R. & T.D. TAYLOR 1983 *Computational methods for fluid flow*. Springer Verlag.

RICHARDSON, J.F. & W.N. ZAKI 1954 Sedimentation and fluidization. *Trans. Inst.Chem.Engng*, Vol. 32, pp. 35-53.

RODI, W. 1984 *Turbulence models and their application in hydraulics. A state of the art review*. 2nd revised ed. IAHR, Delft.

RUSSELL, R.C.H., & J.D.C. OSORIO 1957 An experimental investigation of drift profiles in a closed channel. *Proc. 6th Conf. Coastal Engng*, Miami, Chapt 10, pp. 171-193.

RIJN, L.C. VAN, 1987. Mathematical Modelling of Morphological Processes in the Case of Suspended Sediment Transport. Thesis, Dep. of Fluid Mechanics, Delft University of Technology, Delft, The Netherlands.

RIJN, L.C. VAN, 1993. Principles of sediment transport in rivers, estuaries and coastal seas. Aqua Publ. (The Netherlands).

SATO, 2. & K. YAMAMOTO 1987 Lagrangian measurement of fluid-particle motion in an isotropic turbulent field. J. Fluid Mech., vol. 175, pp. 183-199.

TENNEKES, H. & J.L. LUMLEY 1983 *A first course in turbulence*. MIT Press (ninth printing).

UITTENBOGAARD, R.E., J.C. WINTERWERP, J.A.Th.M. van KESTER & H. LEEPEL 1996 *3D cohesive sediment transport; part I: text, part II: figures and appendices*. DELFT HYDRAULICS, report Z-1022, March.

VAN DYKE, M. 1975 *Perturbation methods in fluid mechanics*. Parabolic Press, Stanford.

VELTHUIZEN, H.G.M. & L. VAN WIJNGAARDEN 1969 Gravity waves over a non-uniform flow. *J. Fluid Mech.,* vol. 39, part 4, pp. 817-829.

WINTERWERP, J.C. AND R.E. UITTENBOGAARD, 1997, Sediment transport and fluid mud flow. Report Z2005, WL|DELFT HYDRAULICS.

ZYSERMAN, J.A. AND J. FREDSØE, 1994. Data analysis of bed concentration of suspended sediment. Proc. Am. Soc. Civ. Eng., *Journal of Hydraulic Engineering*, 120(9):1021-1042.

Appendix A

A Overview of solution procedure

The names of the most important subroutines are indicated between brackets [..] and in capitals; the most important variable names are written between (..) and in italics.

Initialise the computation

- Initialise arrays [INIARR];
- Read input file named INDPM.ext0 with extension "ext0" [INPUT];
- Initialise mean flow and turbulence according to log profile [INIT];
- The input file allows for solving one or two mean-flow momentum equations, choose between Directional Point Model (DPM), possibly with Coriolis force included, or one-dimensional model (1DV) e.g. for wave-tunnel experiments ;
- The input file refers to other input files with harmonic components or time series for variable water level and depth-averaged mean flow to be solved by the mean-flow momentum equations. The latter also includes the definition of wave-tunnel oscillatory flow superimposed on mean flow;
- The input file refers to a file with harmonic components (angular frequency, phase and surface amplitude) of orbital motions to be simulated as well as other harmonic components for harmonic analysis only such as subharmonics;
- The input file defines the time step (*timest*) for solving the mean momentum equations;
- The input file defines the relaxation time step (*reltim*) for control over depth-averaged mean flow velocity, *reltim* serves as response time to following the prescribed depth-averaged flow and WCI forcing;
- The input file defines the number (*numwav*) of orbital time step per time step (*timest*) of the mean flow;
- If *numwav*=0 then just the mean flow equations are solved e.g. for simulating wave tunnel experiments or tidal flow only;
- The input file allows for selection of the k-ε or k-L turbulence models (*kep* or *k-l*) or just laminar (*lam*) flow. In case of sediment, salt or temperature transport, buoyancy effects are included in the turbulence models;
- The bed friction is by Chezy, Manning or bed roughness (note z_0 not k_s);
- The input file allows for the definition of various sediment fractions (*sand* or *floc*), the type of boundary condition for sand transport (*pickup* or *bedcon*) as well as initial concentration profiles.
- For the time being, the output is limited to just two sediment fractions;
- The output file OUTDPM.ext0 contains a copy of input as understood by the code (please check).

- **Start outer loop for solving mean-flow momentum equations with time step $\Delta t^{(mean)}$.**
  - Define depth-averaged mean flow vector [UPDTS or UPFOU];
  - Define wind vector [UPWIN];
  - Solve mean-flow momentum equations [UVMOM] depending on vector sum of WCI forces, Stokes drift and low-pass filtered eddy viscosity;
  - Solve wave numbers and amplitude profile of hydrodynamic pressure for all wave frequencies for the given mean flow [SOLVEP], note that if mean flow oscillates then wave numbers respond accordingly;
  - **Start inner time loop for solving all orbital momentum equations with time step $\Delta t^{(orbit)}$**
    - Time step $\Delta t^{(orbit)}$ is an integer fraction (*numwav*) of $\Delta t^{(mean)}$ (*timest)* of solving mean-flow equations;
    - **Start frequency loop per frequency $f^{(n)}$ with time step $\Delta t^{(orbit)}$:**
      - Start with longest wave which usually has most energy and prescribe water surface elevation of spectral component [DEFWAV];
      - Project z-dependent mean-flow vector on direction of wave propagation [PROJEC];
      - Update sum of orbital velocities and project it on direction of wave propagation $\underline{k}^{(n)}$ [PROJEC];
      - Compute time dependent pressure [SOLVEP] with amplitude profile defined outside loop;
      - Define high-pass filtered eddy viscosity [TURCLO];
        - Solve orbital momentum equation for $\underline{u}^{(n)}$ in direction of wave propagation [WWAV;UWAV];
      - Compute double-contracted strain rate $d_{ij}d_{ij}$ induced by $\underline{u}^{(n)}$ [INCOMP];
      - Add frequency-weighted strain rates $f_{hp}d_{ij}d_{ij}$ for turbulence production [ALLDIJ];
      - Add contribution to vertical orbital velocity w_{inc} according to incompressibility [INCOMP];
      - Stop averaging operation at every second zero crossing of free-surface elevation and
      - compute Stokes drift and WCI force in direction of wave propagation [AVERAG];
    - **End frequency loop**
    - Define fall velocity [FALLVE] for sand, hindered settling included;
    - Low-pass filter bed friction for mean flow [USTAR];
    - Harmonic analysis of velocity, TKE, eddy viscosity, sediment concentration and horizontal sediment transport [ORBIT];
    - Define total density by salt, temperature and sediment [DENS];
    - Solve turbulence model [TRATUR (k-ε); KLMOD] including buoyancy;
    - Define fall velocity [FALLVE] for sand, hindered settling included;
    - Define bed condition for sand transport [REFCON];
    - Solve sediment transport with advection and mixing due to all orbital motions [SEDWAV 1st upwind], built-in options are [SEDCEN central advection] and [DIFU1D 3rd order upwind ADI];
  - **End inner time loop**
  - Apply vector summation of all frequency-dependent WCI forces and Stokes drift;
- **End outer time loop**
- Summarize all temporary output files [OUTMAP] and write to OUTDPM.ext0;
- Write results of harmonic analysis [SPCTRL] to OUTSPC.ext0.
- **End simulation**

Appendix B

B Direction of orbital velocity and wave number vectors

Consider a mean flow U(z) in x-direction and possible with a vertical profile; this flow is without friction, viscosity and turbulence. Superimposed on this flow are infinitesimal waves propagating with horizontal wave number $\underline{k}=(k, \ell)$ and we define the orbital velocity as

$$\underline{\tilde{u}} = \underline{\hat{u}}(z)\exp\left[i(kx+\ell y)-i\omega t\right] \tag{B.1}$$

with angular frequency ω. In this appendix we investigate under what conditions and how much the direction of the velocity amplitude $\underline{\hat{u}}(z)$ deviates from the wave number direction $\underline{k}$. Consider therefore the two horizontal momentum equations for these waves:

$$\frac{\partial \tilde{u}}{\partial t} + U\frac{\partial \tilde{u}}{\partial x} + \tilde{w}\frac{dU}{dz} + \frac{\partial \tilde{p}}{\partial x} = 0 \tag{B.2a}$$

$$\frac{\partial \tilde{v}}{\partial t} + U\frac{\partial \tilde{v}}{\partial x} + \frac{\partial \tilde{p}}{\partial y} = 0 \tag{B.2b}$$

The direction of $\underline{\hat{u}}(z)$ is obtained by eliminating the pressure from (B.2) and this proceeds by using (B.1) also for the wave-induced pressure. Equation (B.2a) then yields

$$-ik\hat{p} = i(kU-\omega)\hat{u} + \hat{w}\frac{dU}{dz} \quad . \tag{B.3a}$$

Likewise, (B.2b) is converted into

$$-i\ell\hat{p} = i(kU-\omega)\hat{v} \tag{B.3b}$$

Multiplication of (B.3a) with (ik) and (B.3b) with (iℓ) and adding the two equations provides

$$\left(k^2+\ell^2\right)\hat{p} = i(kU-\omega)(ik\hat{u}+i\ell\hat{v}) + i\,k\,\hat{w}\frac{dU}{dz} \tag{B.4}$$

From incompressibility follows

$$ik\hat{u} + i\ell\hat{v} + \frac{d\hat{w}}{dz} = 0 \tag{B.5}$$

and substitution of this relation in (B.4) yields:

$$\hat{p} = -\frac{i(kU-\omega)}{k^2+\ell^2}\frac{d\hat{w}}{dz} + \frac{ik\hat{w}}{k^2+\ell^2}\frac{dU}{dz} \tag{B.6}$$

This expression for the pressure amplitude is substituted into (B.3) and provides the desired relations from which follows the direction of the velocity amplitude.

$$i(k^2+\ell^2)\hat{u} = -k\frac{d\hat{w}}{dz} + \frac{\ell^2\hat{w}}{\omega-kU}\frac{dU}{dz} \tag{B.7a}$$

$$i(k^2+\ell^2)\hat{v} = -\ell\frac{d\hat{w}}{dz} - \frac{k\ell\hat{w}}{\omega-kU}\frac{dU}{dz} \tag{B.7b}$$

The last terms in (A7a+b) is responsible for the deviation between the direction of the horizontal vector of the wave velocity amplitude $\underline{\hat{u}}(z)$ and the wave number $\underline{k}$. For waves perpendicular to the mean flow k=0 holds and then

$$i\hat{u} = \frac{\hat{w}}{\omega}\frac{dU}{dz} \quad ; \quad i\hat{v} = -\frac{1}{|\underline{k}|}\frac{d\hat{w}}{dz}$$

Consequently, the angle difference between horizontal wave velocity vector and wave number vector follows from

$$\frac{\hat{u}}{\hat{v}} = \frac{|\underline{k}|}{\omega}\frac{\hat{w}}{\frac{d\hat{w}}{dz}}\frac{dU}{dz} \approx \frac{\tanh(|\underline{k}|z)}{\omega}\frac{dU}{dz} \tag{B.8}$$

where in the last approximation the potential theory solution $\hat{w} \propto \sinh(|\underline{k}z|)$ for infinitesimal waves without shear is implemented. We estimate this angle difference due to a logarithmic velocity profile with

$$\frac{dU}{dz} = \frac{u_*}{\kappa z}$$

This ratio is large near the bed and there we can approximate $\tanh(|\underline{k}|z) \approx |\underline{k}|z$ whence

$$\frac{\hat{u}}{\hat{v}} \approx \frac{\tanh(|\underline{k}|z)}{\omega}\frac{dU}{dz} \approx \frac{|\underline{k}|u_*}{\kappa\omega} \tag{B.9}$$

The angle is thus proportional to the ratio between bed shear velocity u_* and the wave's celerity and this ratio is negligible because u_* is a small fraction, typically 1/10, of the mean flow and the Froude number for the waves is also significantly less then unity.

More generally, the order-of-magnitude of the ratio between the last terms in (B.7a+b) and the first terms reads:

$$\frac{\text{shear terms}}{\text{without shear}} = O\left\{\frac{1}{c_p - kU/|\underline{k}|}\frac{\tanh(|\underline{k}|z)}{|\underline{k}|}\frac{dU}{dz}\right\} \approx O\left\{\frac{u_*}{c_p - kU/|\underline{k}|}\right\} \quad ; \quad c_p = \frac{\omega}{|\underline{k}|} \tag{B.10}$$

and the same order of magnitude appears. The ration (B.10) shows that it becomes significant if the wave's celerity approach the mean flow velocity U and this occurs first for waves propagating with the current. However, then there is no change in wave direction.

We conclude, therefore, that the orbital velocity amplitude $\hat{\underline{u}}(z)$ *is practically parallel with the wave number vector* $\underline{k}$*, the deviation being of the order of the ratio between shear stress velocity and the wave's phase speed relative to the mean flow.*

Appendix C

C Partial slip condition

In this appendix we present details of the implementation of the partial slip condition for the turbulent flow along a bed in the fully-rough regime. We follow closely (Hinze, 1975) and (Jackson, 1981).

Hinze (1975, p. 636) defines the condition of a fully-rough bed by:

$$\frac{u_* k_s}{\upsilon} \geq 55 \tag{C.1}$$

with k_s the Nikuradse length scale which is of the order of the geometrical height of the roughness forming elements that create the fluid-bed interface. Note, however, that condition (C.1) is satisfied only for long and high waves or strong currents. The implementation of the transitional roughness regime is recommended.

The essential and very subtle problem is the definition of reference level normal to the bed, here the z-direction, and z is positive away from the bed. Hinze (1975, eq. 7-76) defines the plane z=0 as the average of the top levels of the roughness forming elements. Subsequently, Hinze defines the logarithmic profile above a rough bed by

$$\frac{U(z)}{u_*} = \frac{1}{\kappa} \ln\left\{\frac{u_*(z + k_e)}{\upsilon}\right\} + B - \frac{\Delta U(z)}{u_*} \quad ; \quad \kappa = 0.41 \quad , \quad B = 4.9 \quad , \tag{C.2}$$

and, based on various observations (Hinze, 1975, fig. 7-16),. Hinze (1975, eq. 7-76) estimates the apparent origin of the logarithmic velocity profiles at $z=-k_e$ and $k_e=0.25\ k_s$. The latter conclusion is substantiated by Jackson (1981) who derives the meaning of this origin and shows for various roughness elements that

$$k_e = 0.3 k_s \tag{C.3}$$

holds. In the following, we adopt (C.3).

For $\Delta U=0$, the formulation (C.2) is equivalent to the turbulent layer flow along a hydraulically smooth wall but with the origin $0.3k_s$ below the mean top levels of the fluid-bed interface. For a rough bed, there occurs a velocity shift ΔU and Hinze (1975, p. 637) concludes from his figure 7-16:

$$\frac{\Delta U(z)}{u_*} = \frac{1}{\kappa} \ln\left\{\frac{u_* k_e}{\upsilon}\right\} + C \quad ; \quad C \approx -0.4 \quad , \tag{C.4}$$

where C is given an average value for various type of roughness elements. Combining (C.2), (C.3) and (C.4) yields

$$\frac{U(z)}{u_*} = \frac{1}{\kappa}\ln\left\{8.78 + \frac{29.3z}{k_s}\right\} \quad ; \quad \kappa = 0.41 \tag{C.5}$$

Given the customary relation $z_0=k_s/30$ between roughness length scale z_0 and geometrical scale k_s as well as the uncertainty range in the various parameters (κ, B and C), we simplify (C.5) as:

$$\frac{U(z)}{u_*} = \frac{1}{\kappa}\ln\left\{\frac{9z_0 + z}{z_0}\right\} \quad . \tag{C.6}$$

We apply formulation (C.6) in conjunction with the precise definition of the plane z=0. It is this plane z=0 that equals the bottom of the first computational grid box above the bed. We believe the concept (C.6) should be followed strictly. For instance when using the mean shear rate at the level z=0 of the bed-grid box:

$$\left.\frac{\partial U}{\partial z}\right|_{z=0} = \frac{u_*}{9\kappa\, z_0} \quad . \tag{C.7}$$

The equally strict consequence of (C.7) is that the eddy viscosity at the bed level z=0 follows from the definition u_*^2 i.e.

$$u_*^2 = \left\{\upsilon_T(z)\frac{\partial U}{\partial z}\right\}\Bigg|_{z=0} : \qquad \upsilon_T(z=0) = 9\kappa\, u_*\, z_0 \tag{C.8}$$

Note that in the first expression of (C.8) the kinematic viscosity is excluded in accordance with the hydraulically rough regime (C.1) for which (C.6) has been derived. On the other hand, if the kinematic were included in (C.8) is would be negligible provided (C.1) is satisfied but this not always the actual application of the previous formulation. Therefore, we exclude the kinematic viscosity in (C.8).

The bed boundary conditions for the k-L as well as k-ε model should match the eddy viscosity defined by (C.8) and at z=0.

In our k-L model the closure for eddy viscosity reads:

$$\upsilon_T(z) = c_\mu' L(z)\sqrt{k(z)} \tag{C.8}$$

and at the bed we define the Turbulent Kinetic Energy by:

$$k(z=0) = \left(\frac{u_*}{c_\mu'}\right)^2 \tag{C.9}$$

Consequently, given (C.8), the mixing length scale must be defined as:

$$L(z=0)=9\kappa\, z_0 \tag{C.10}$$

This completes the boundary conditions for the k-L model. The Bakmetev length scale profile is then defined with $z=-9z_0$ as virtual origin for L(z).

Next we continue with the appropriate bed boundary conditions for the k-ε model. Near the bed under high-Reynolds turbulence conditions and a logarithmic boundary layer must hold:

$$\varepsilon=\upsilon_T\left(\frac{\partial U}{\partial z}\right)^2\equiv\frac{u_*^3}{\kappa(z+9z_0)} \tag{C.11}$$

Appendix D

D Description of program in- and output

As an illustration, the format of the input and output files is discussed using the C1-case of the wave tunnel calculations. Only the input files are listed, as the length of the output files is too large. Instead, the output files are schematically discussed.

The main input file is the file indpm.id, where id stands for the identification string of the calculation (i.e. c1 in our case). The input of this file is typeset in Courier, whereas the explanation is typeset in Times.

```
*******General               input********
1DV         DIMENS: choose 1DV or DPM
```

If 1DV is chosen, only one velocity component is solved. If DPM (directional point model) is chosen, two velocity components (u and v) are solved. In the β-release distributed with this report, the DPM-variant does not work properly with the sediment subroutines.

```
0.0         FCORIO: Coriolis parameter
```

Coriolis parameter (0 in the wave tunnel and flume experiments, 1 in the field)

```
0.          DP    : depth
```

Depth of the water column below the ζ (zeta) = 0 plane. For the present calculations the plane ζ = 0 is defined at the bottom of the wave tunnel, therefore DP = 0.

```
0.0         ZETA  : water-level (or)
            FILTSZ: file time series ZETA (or)
tun_c1.lvl  FILFOZ: file fourier comp. ZETA (or)
```

Surface elevation, in the current case specified in fourier components in the file tun_c1.lvl. The value of ZETA in the first line is neglected if a file is specified in the second or third line.

```
0.0         UMEAN : West-to-East depth-averaged velocity (or)
            FILTSU: file time series UMEAN (or)
tun_c1.vel  FILFOU: file fourier comp. UMEAN (or)
```

Horizontal velocity, in the current case specified in fourier components in the file tun_c1.vel. The value of UMEAN in the first line is neglected if a file is specified in the second or third line. Note that the depth-averaged velocity is specified, not the velocity at a certain level.

```
sec         TUNIT : time unit (SEC/MIN)
```

Chose time unit: seconds or minutes.

```
0.05        TIMEST: time step (in TUNIT)
15600       NUMTIM: number of timestep simulation
0           NUMWAV: number of timestep orbital motion per TIMEST
```

In order to solve orbital motions accurately at a large time step (compared with the wave period), the orbital motion can be solved using a smaller time step, being the wave period divided by NUMWAV.

```
0.05        RELTIM: relaxationtime (in TUNIT)
```

The relaxation time should not be chosen smaller than the time step!

```
65 0.20  78 TIMEWR: STRT-INC-STOP time frame writing output (TUNIT)
```

The first number is the start time, the second number the time increment and the third number the stop time with regard to writing to the output file.

```
1.0         TETA  : par. theta-method(rec. theta =1)
```

This is a input parameter for the integration method used. It is recommended to set θ at 1.

```
KEP         MODEL : choice between LAM (laminar flow) or KEP (k-epsilon turb. model)
```

Chose turbulence model: lam (laminar flow), k-l or kep (k-epsilon model).

```
1e-6        VISCOU: kinematic viscosity [m^2/s]
Z0          ROUMET: roughness meth. MANN/CHEZ/Z0
```

Chose roughness method: Manning, Chézy or z_0.

```
3.2e-5      ROUCOF: roughness height (ROUMET)
1           IRO   : IRO=0: hydr.smooth, IRO=1: hydr.rough

            FLTWIN: file time series (directional) wind and surface waves (or)
0.          DIRWI : direction from which the wind blows
0.          WIND  : wind speed, 10 m above free surface
```

The three lines here are intended for wind-generated waves and are not used in the wave tunnel case.

```
wavspc.c1   FLTSPC: file with directional spectrum of surface waves (or)
0.          DIRWA : direction from which the surface waves come
0.          HSIG  : significant wave height
0.          PERIO : significant wave period
1000.0      RHOM  : reference density
*******Layer       Input********
VARIA       LAYDIS: choose EQUIDistant or VARIAble
```

If VARIA is selected, the layer distribution is logarithmic with a power specified below; with EQUID a equidistant distribution is selected.

```
500         KMAX  : number of layers
```

Here the number of layers is specified. The maximum is 1000.

```
1.5         ALFA : >1 power in layer distribution, ALFA ignored for equidistant
layers

*******Constituent Input********
0           LMAX  : number of constituents
0           LSAL  : index nr for salinity
0           LTEM  : index nr for temperature
10.0        SALEQS: eq. of state salinity (always input)
5.0         TEMEQS: eq. of state temperature (always input)
```

The constituent input is not used for the wave tunnel calculations.

```
*******Sediment    Input********
1           LSED     : number of sediment
```

The number of sediment types can be specified here, each to be assigned a name label and sediment properties.

```
sand        SEDTYP(L): type of sediment
0.7         SIGSED(L): prandtl schmidt number
2650        RHOSOL(L): density sediment
0.21e-3     SEDDIA(L): D_50 [m] of sand

bedcon      EROTYP(L): PICKUP or BEDCON for type of bed condition
```

Two types of bed boundary conditions can be selected: PICKUP or BEDCON.

```
step        SEDDIS   : "step" or "linear"
```

An initial sediment concentration distribution may be applied, either a ‘step’or a linear distribution.

```
0.0         SEDTOP(L): sediment concentration above step
0.0         SEDBED(L): sediment concentration below step
100         KSTEP    : k-value of sediment step position
*******End         Input********
```

The files to which is referred in the input file indpm.c1 are: tun_c1.lvl, tunc1.vel and wavespc.c1. These are discussed below.

tun_c1.lvl

```
2       O1      K1      nfc [number of harmonic component]
```

Specify number of harmonic components and their label.

```
      199385  398769   frequency(n=2:nfc) [degrees/hour] must equal those in zeta-
file
```

Specify frequencies in degrees per hour!

```
1.1     0.0     0.0     ampl (n=1:nfc)  [m]
```

The first number is the constant component of the water level, i.e. the height of the wave tunnel section (1.1 m).

```
        0.0     0.0     phase(n=1:nfc)
```

tunc1.vel

```
2    1                  nfc ; ksec
```
Specify number of harmonic components and number of velocity components to be weighed.
```
1.0                     weight(k=1:ksec)
```
Specify the time unit (k=1: ksec).
```
     199385   398769   frequency(n=2:nfc) [degrees/hour] must equal those in zeta-
file
```
Specify frequencies in degrees per hour!
```
 0.042  0.844  0.265   U_ampl (k=1;n=1:nfc)
```
Specify the velocity amplitudes in m/s; the first number is the constant component.
```
        0.0     0.0    U-phase(k=1;n=1:nfc)
 0.000  0.000   0.0    V_ampl (k=1;n=1:nfc)
        0.0     0.0    V-phase(k=1;n=1:nfc)
```

wavespc.c1:

```
0     NSPC  : number of spectral components for solving orbital motions
```
With this parameter the number of spectral components for solving orbital motions can be specified, i.e. the spectrum of ζ (surface elevation). For the wave tunnel case NSPC is set at 0. If flume experiments with surface waves are to be modelled, NSPC should be given a value equal to or larger than one.
```
3     NSPCAD: in addition to NSPC other spectral components for harmonic analysis
only
** remark: if NSPC > 1, specify here nr. of spectral component; angular freq.;
** amplitude; phase; direction from which the waves come
** Additional spectral components for harmonic analysis only, angular frequency is
essential:
1  0.0      0.0    0.0    0.
2  0.96665  0.0    0.0    0.
3  1.93329  0.0    0.0    0.
nr.;angular freq.;amplitude;phase;direction from which the waves come; number of
spectral components
```

Description of output files

Results are written to two output files: outdpm.id and outspc.id, where id stands for the identification string of the calculation (i.e. c1 in the case described here). The file outdpm.id first lists the values of the input parameters as specified in the input files, including the specified layer thickness and the initial sediment concentration distribution. Subsequently, the following information is written:

At each time step specified for output three tables are displayed. The first table consists of 8 columns listing for each layer:

1. z-coordinate layer interface
2. turbulent energy
3. turbulent dissipation
4. eddy viscosity
5. du/dz
6. dv/dz
7. dρ/dz
8. Richardson number

The second table consists of 6 columns listing for each layer:

1. *z*-coordinate concentration point
2. *u*-velocity
3. *v*-velocity
4. *uv*-magnitude
5. *uv*-direction
6. density

The third table consists of 2 (or 3 if two types of sediment have been specified: the current program supports 2 sediment types) columns listing for each layer:

1. *z*-coordinate
2. sediment concentration

After the last time step, three tables are displayed containing the same information as the tables specified above, but each of them containing information for all time steps. In one additional column (the first one) the time information is displayed.

The last table in the file outdpm.id contains 12 colums (or more if more than one type of sediment has been specified) displaying for each time step specified for output the following parameters:

1. time (seconds)
2. depth value
3. free surface
4. depth-averaged *u*-velocity
5. calculated depth-averaged velocity
6. difference UREAL-UMEAN for depth-averaged velocity
7. depth-averaged *v*-velocity
8. calculated depth-averaged velocity
9. difference VREAL-VMEAN for depth-averaged velocity
10. Shields parameter sediment fraction 1
11. critical Shields parameter sediment fraction 1
12. prescribed bed conc. sediment fraction 1

The file outspc.id contains the following information:

- the period of each spectral component;
- tables for the parameters *tke* (turbulent kinetic energy), *vicw* (eddy viscosity), *uw*, *utot*, *vtot*, *fwci* (force wave current interaction), sed*i* (sediment concentration fraction *i*), uc_i and vc_i containing 7 columns:
  1. *z*-coordinate *w*-point
  2. amplitude component NF= 1
  3. phase component NF= 1
  4. amplitude component NF= 2
  5. phase component NF= 2
  6. amplitude component NF= 3
  7. phase component NF= 3

In this example 3 components are specified, of which the first is the steady flow component.

Figures

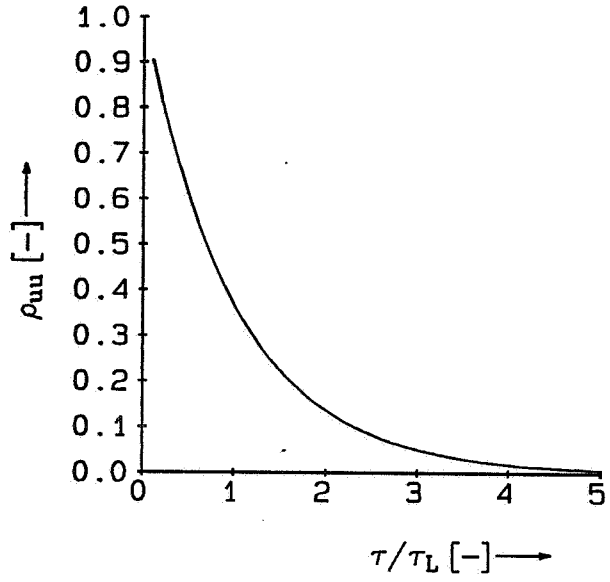

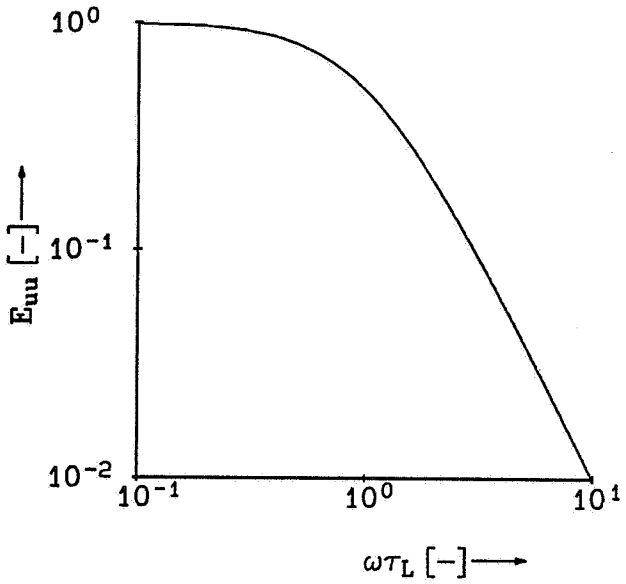

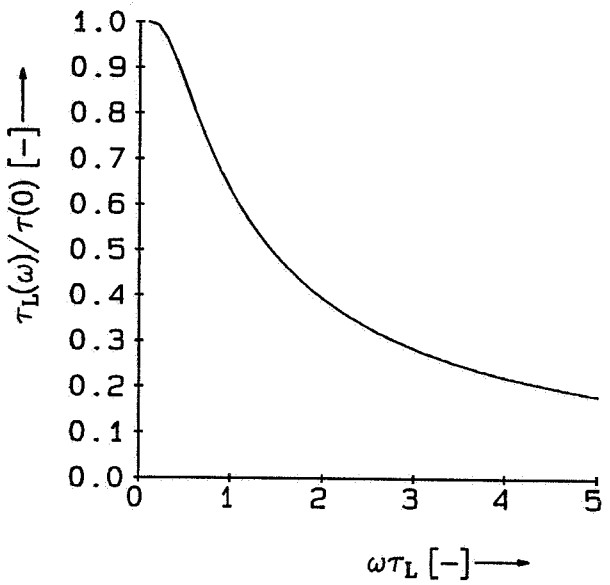

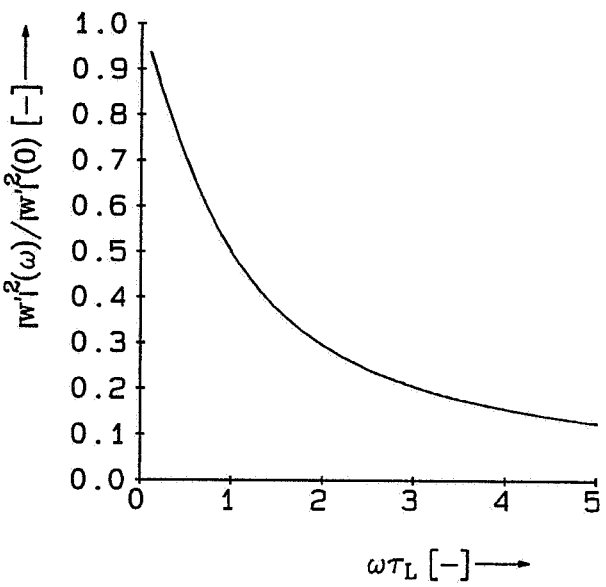

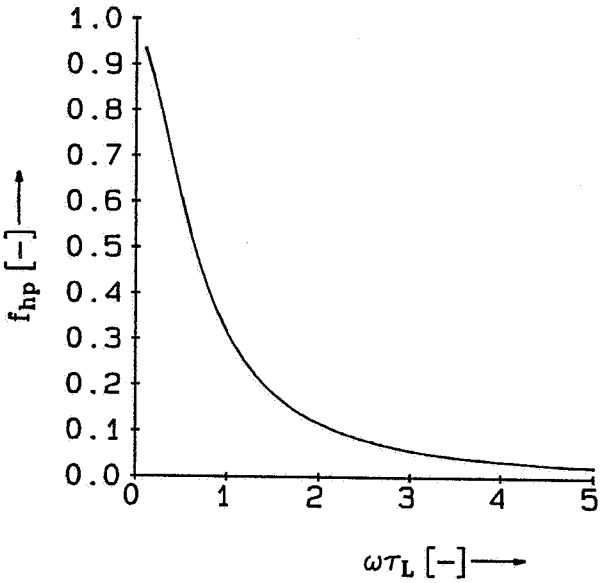

Terms for wave-turbulence interaction.

c:\dpm\surwav\sub.inv

WL|DELFT HYDRAULICS

Z 2733.41

Fig. 1

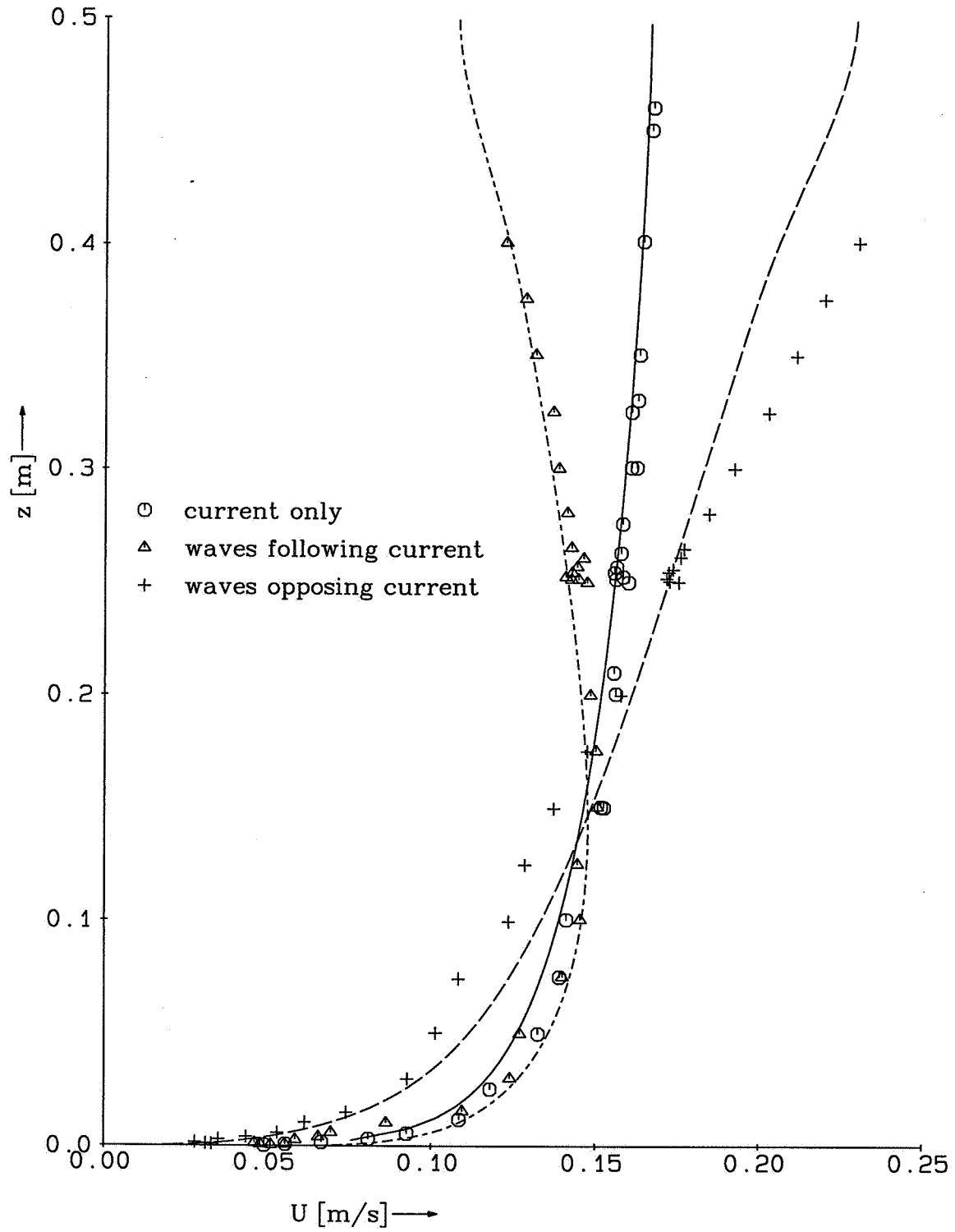

DPM with inner time loop resolving orbital motions and outer loop for mean current affected by net wave forces.
Poisson solver and k–L model with high–pass filtered d_{ij}
Comparison with wave–current experiments of Klopman (1994).

100 layers

c:\dpm\sedmoc\pltf1.clr

WL|DELFT HYDRAULICS

Z 2733.41

Fig. 2

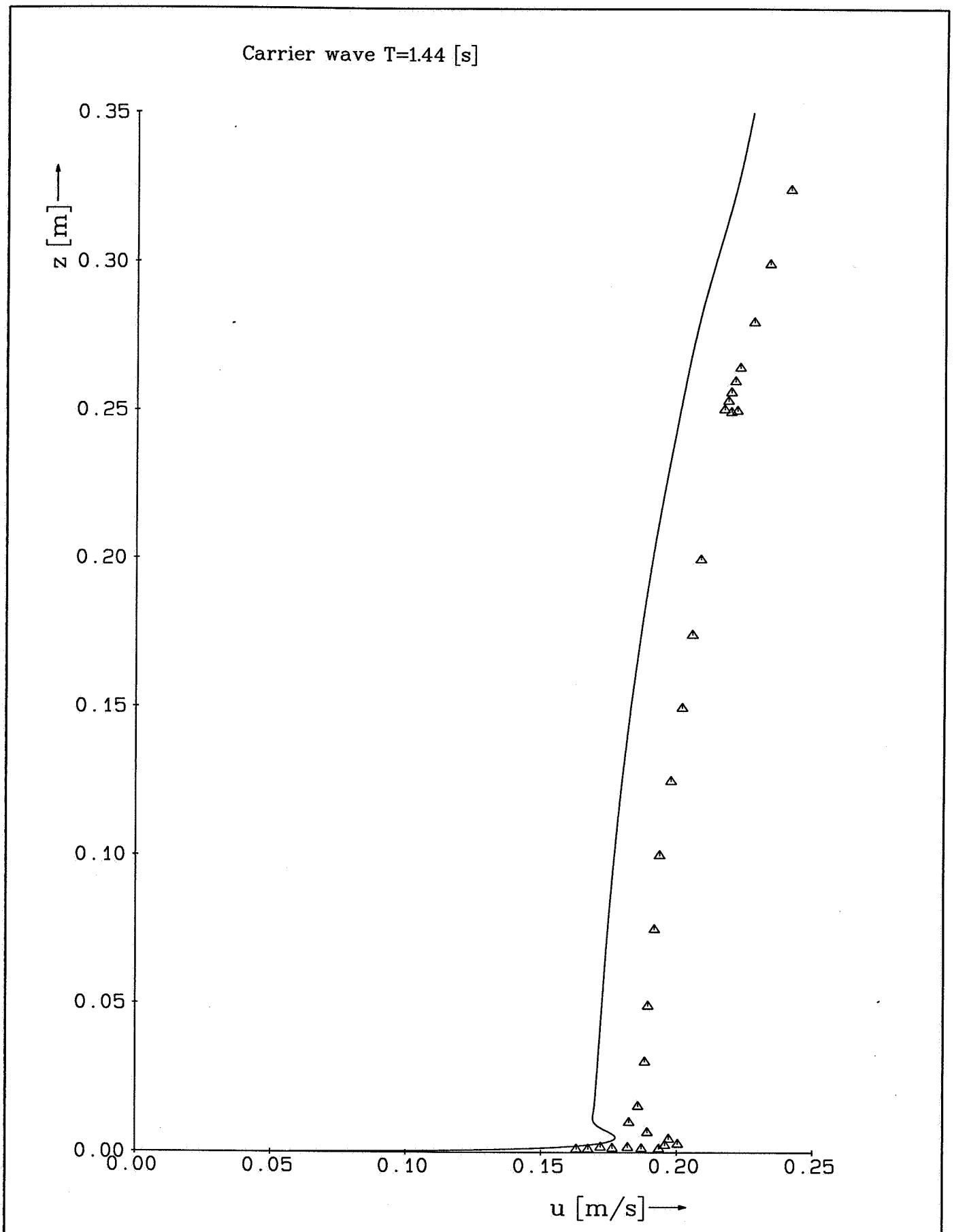

Wave–current with spectral DPM model (Uittenbogaard,1999). Simulation of monochromatic waves propagating with a mean current; compared to experiments of Klopman (1994).

500 non–equidistant points
k–L turb. mod. with h.p. filter

d:\dpm\sedmoc\mon144.mee

DELFT HYDRAULICS

Z 2733.41

Fig. 3

Carrier wave T=1.44 [s]

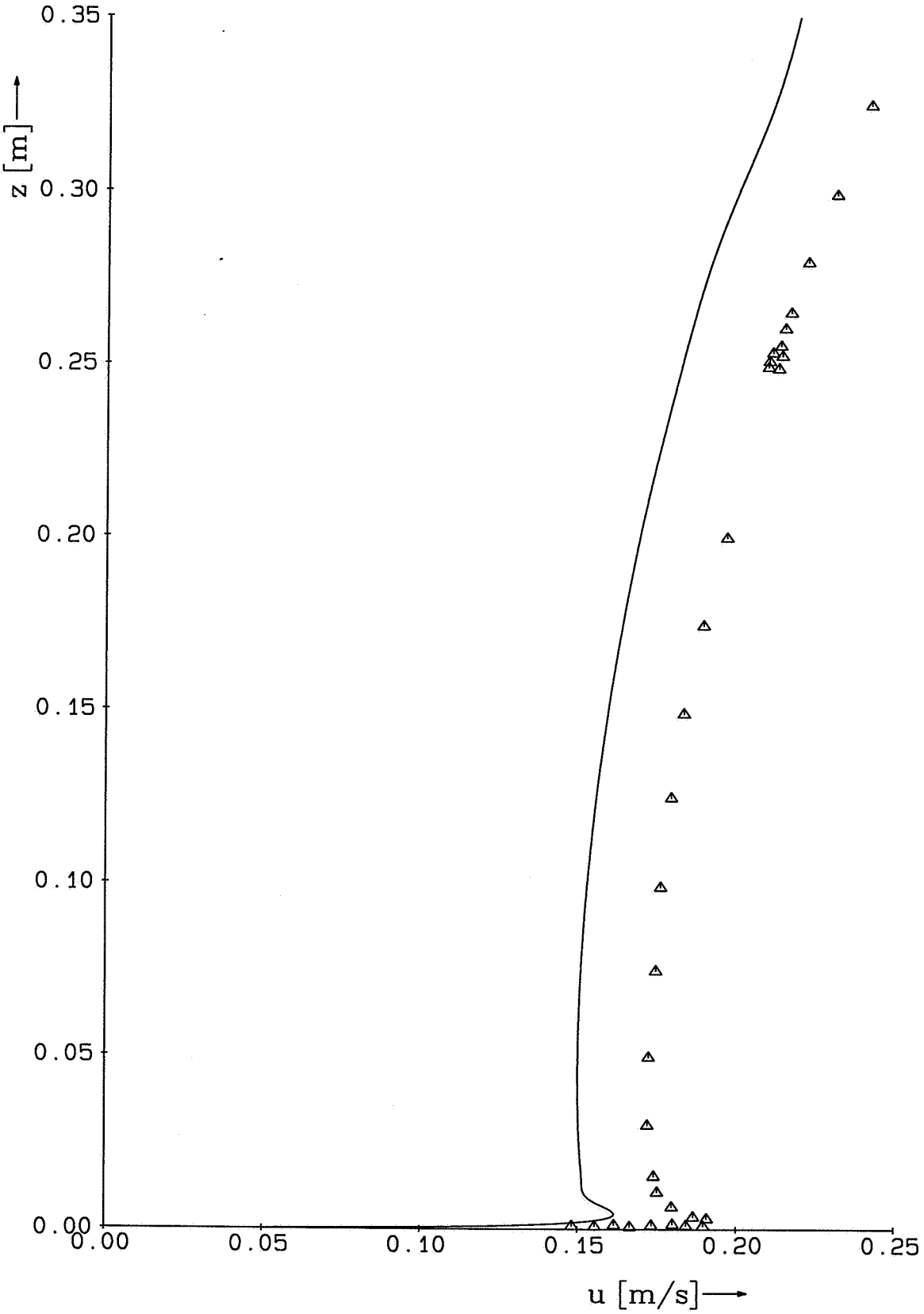

Wave–current with spectral DPM model (Uittenbogaard,1999).
Simulation of monochromatic waves propagating against a mean current; compared to experiments of Klopman (1994).

500 non–equidistant points
k–L turb. mod. with h.p. filter

d:\dpm\sedmoc\mon144.teg

DELFT HYDRAULICS

Z–2733.41

Fig. 4

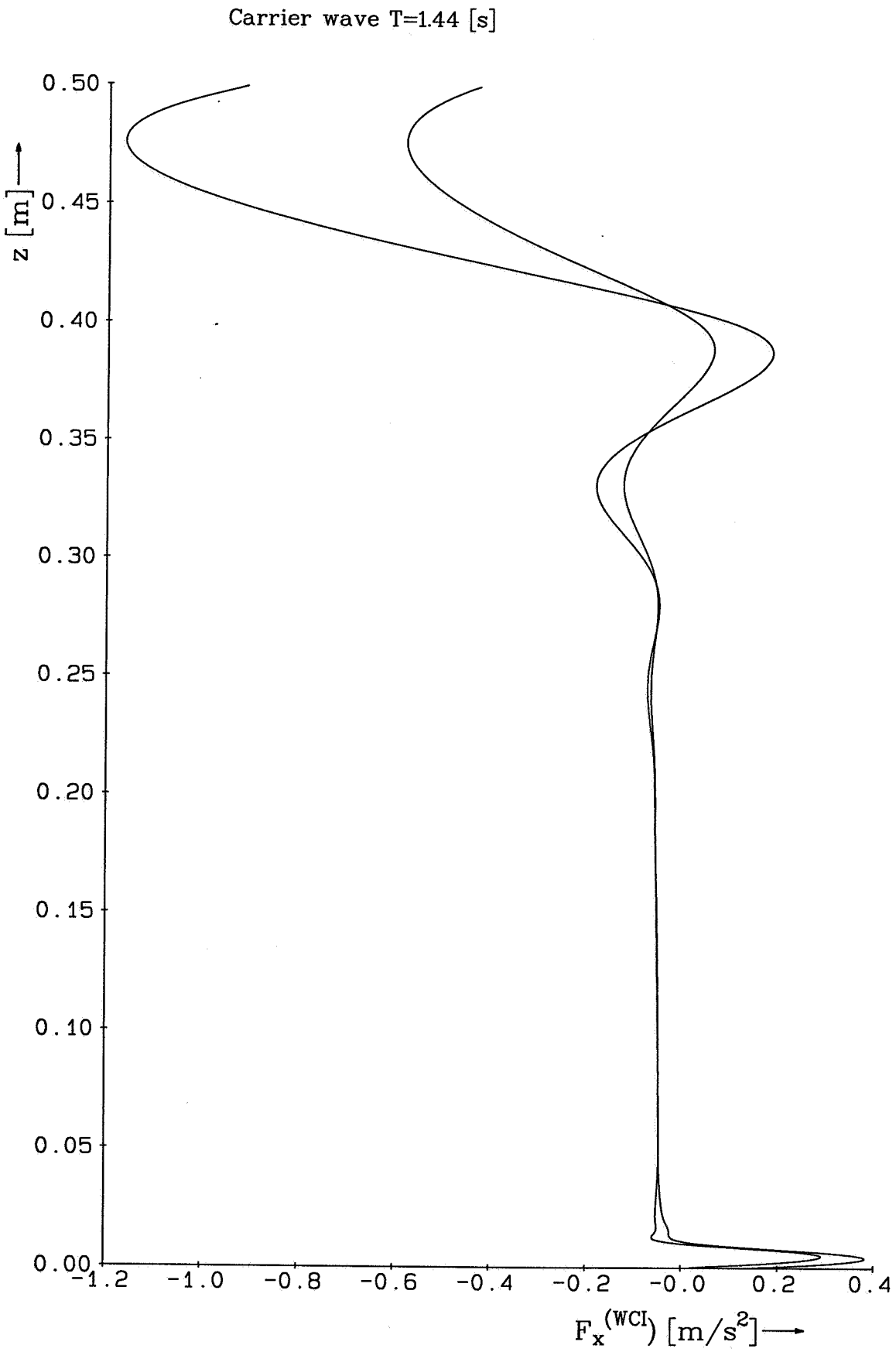

Wave–current with spectral DPM model (Uittenbogaard,1999).
Simulation of monochromatic waves propagating with and against a mean current; compared to experiments of Klopman (1994).

500 non–equidistant points
k–L turb. mod. with h.p. filter

d:\dpm\sedmoc\monwci.mee

DELFT HYDRAULICS

Z– 2733.41

Fig. 5

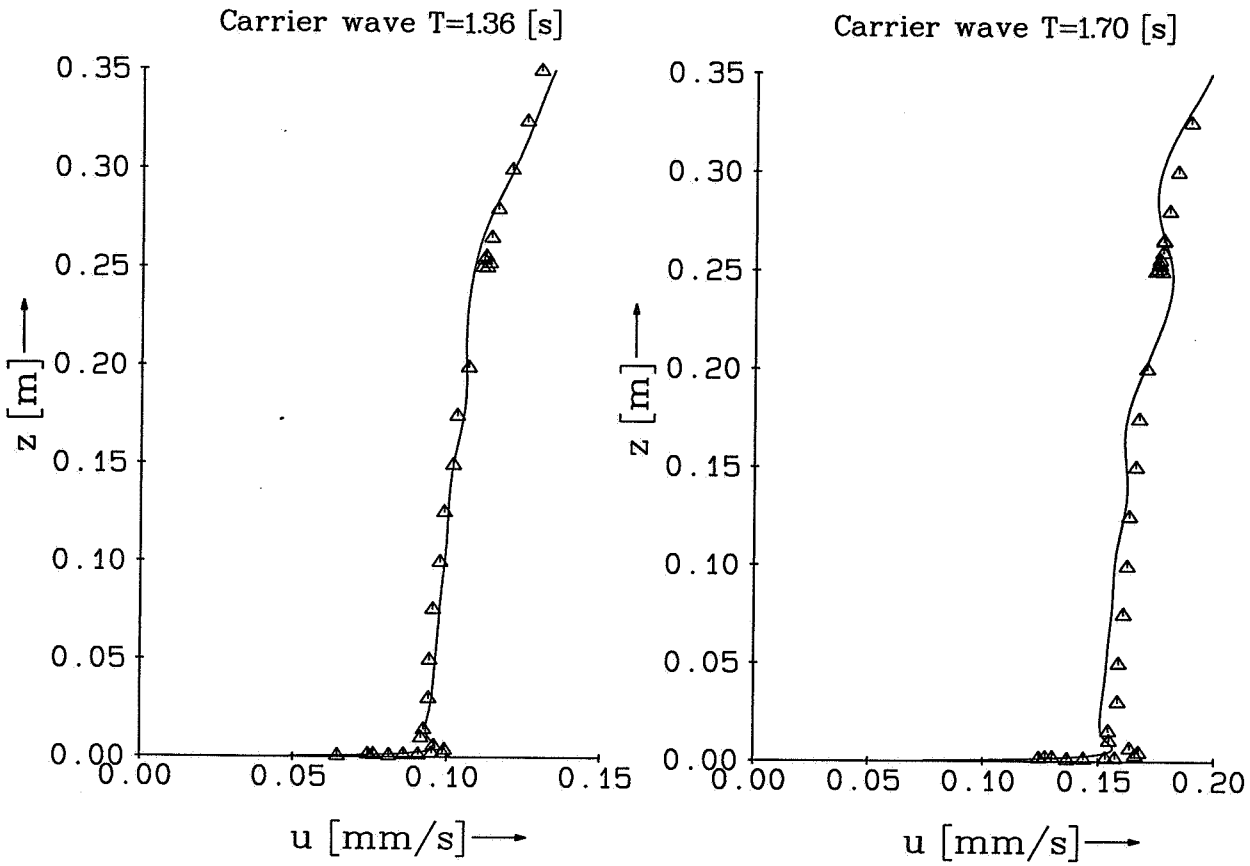

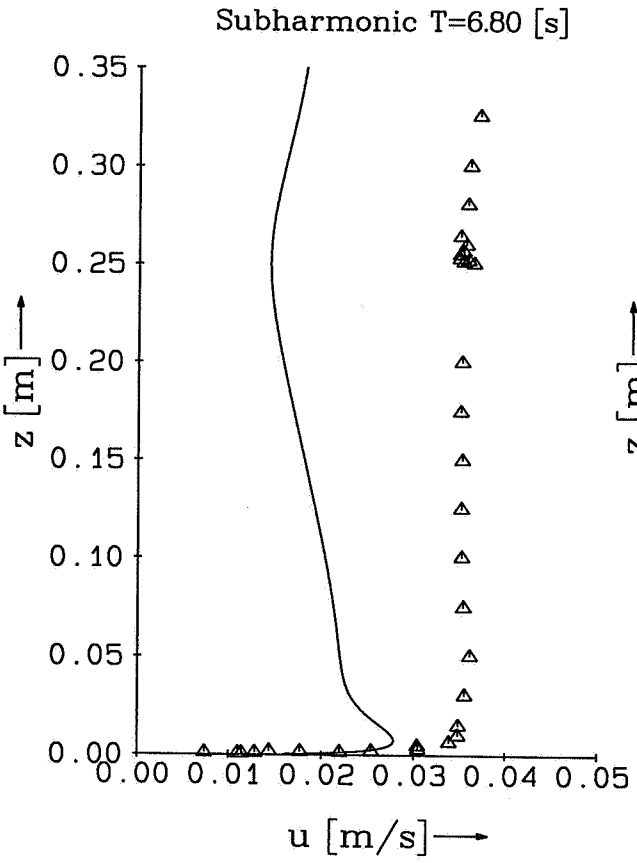

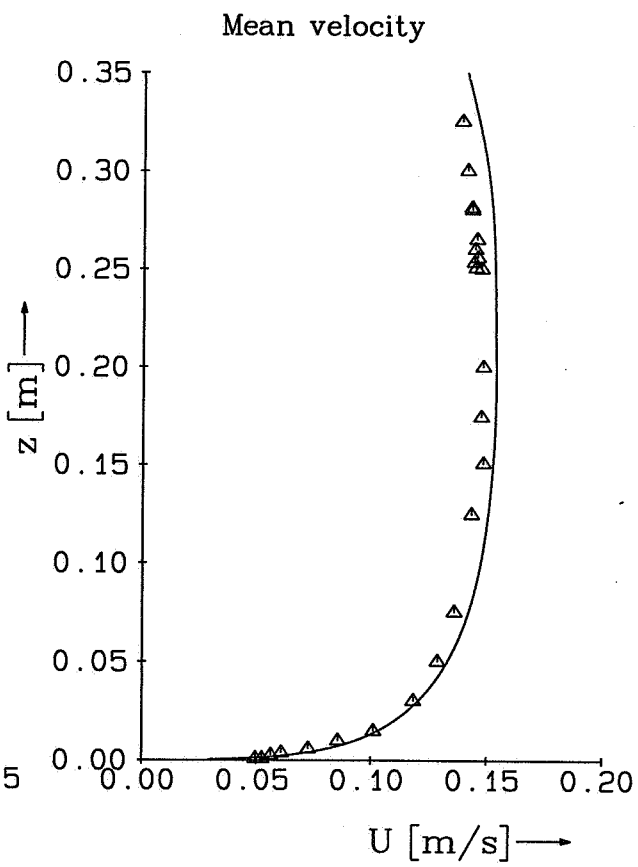

Wave–current with spectral DPM model (Uittenbogaard,1999).
Simulation of biharmonic waves propagating with a mean current; compared to experiments of Klopman (1994).

500 non–equidistant points
k–L turb. mod. with h.p. filter

d:\dpm\sedmoc\bihar.inv

DELFT HYDRAULICS

Z– 2733.41

Fig. 6

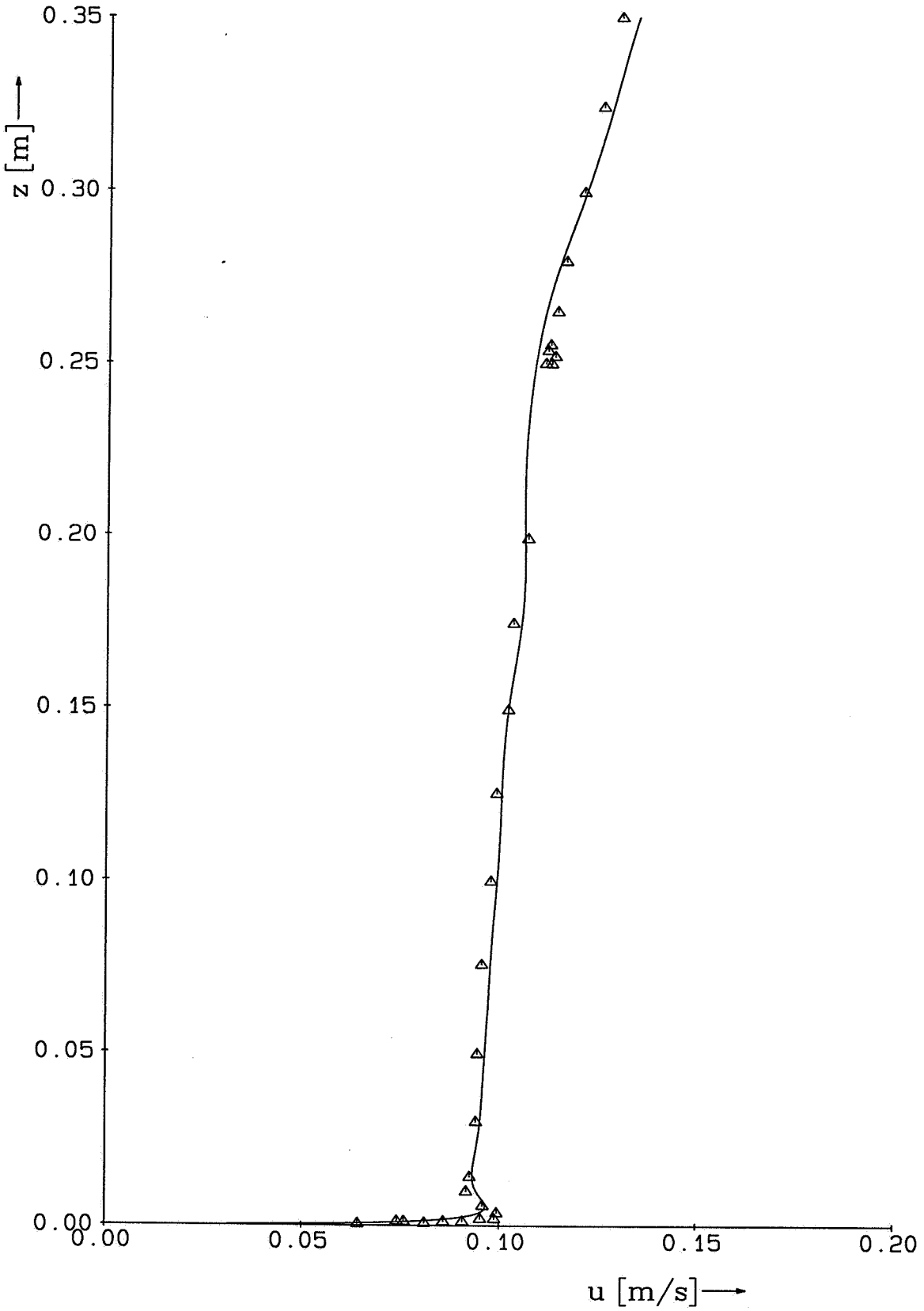

Wave–current with spectral DPM model (Uittenbogaard,1999).
Simulation of biharmonic waves propagating with a mean current; compared to experiments of Klopman (1994).

500 non–equidistant points
k–L turb. mod. with h.p. filter

d:\dpm\sedmoc\bih136.inv

DELFT HYDRAULICS

Z– 2733.41

Fig. 7

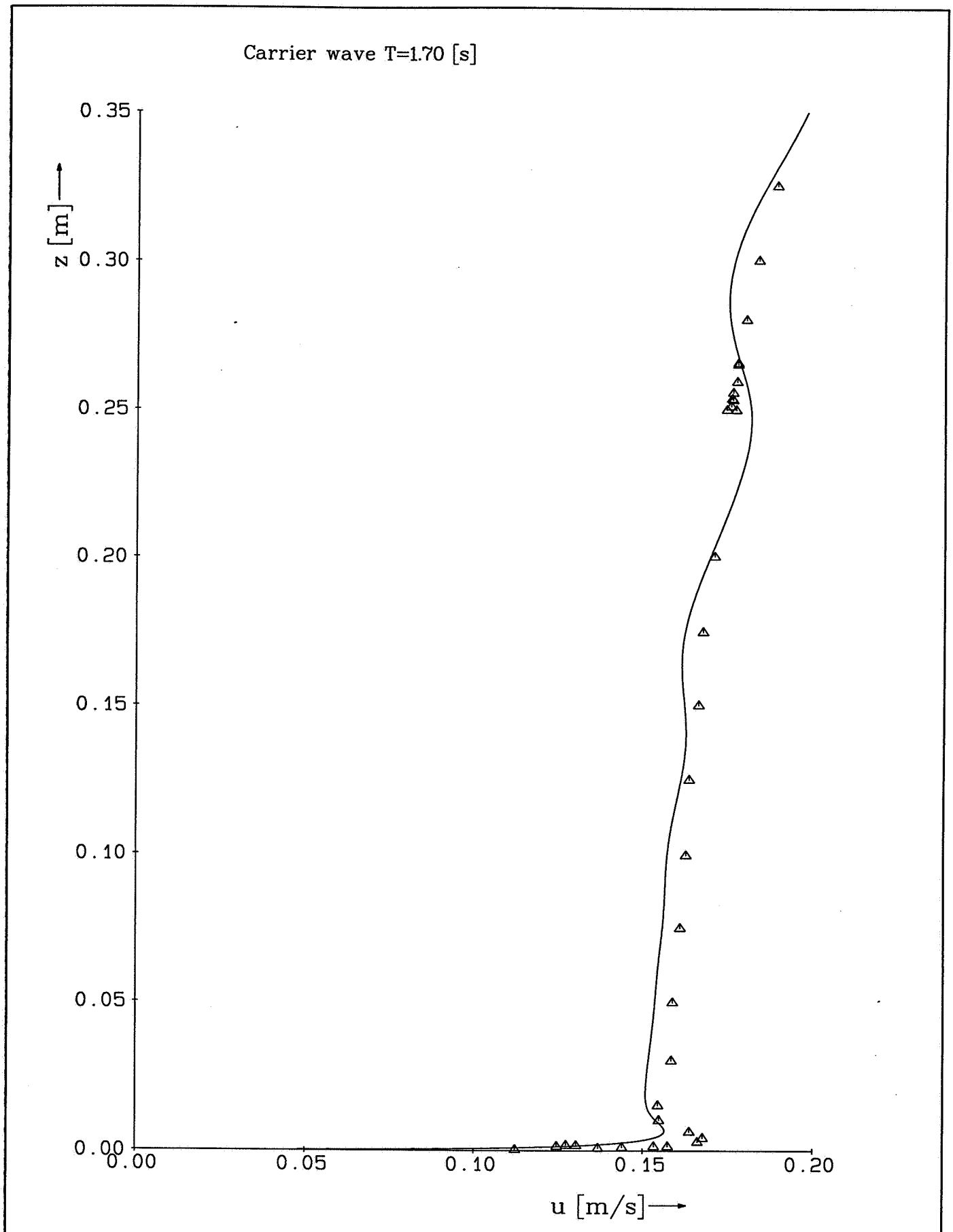

Wave–current with spectral DPM model (Uittenbogaard,1999). Simulation of biharmonic waves propagating with a mean current; compared to experiments of Klopman (1994).

500 non–equidistant points
k–L turb. mod. with h.p. filter

d:\dpm\sedmoc\bih170.inv

DELFT HYDRAULICS

Z–2733.41

Fig. 8

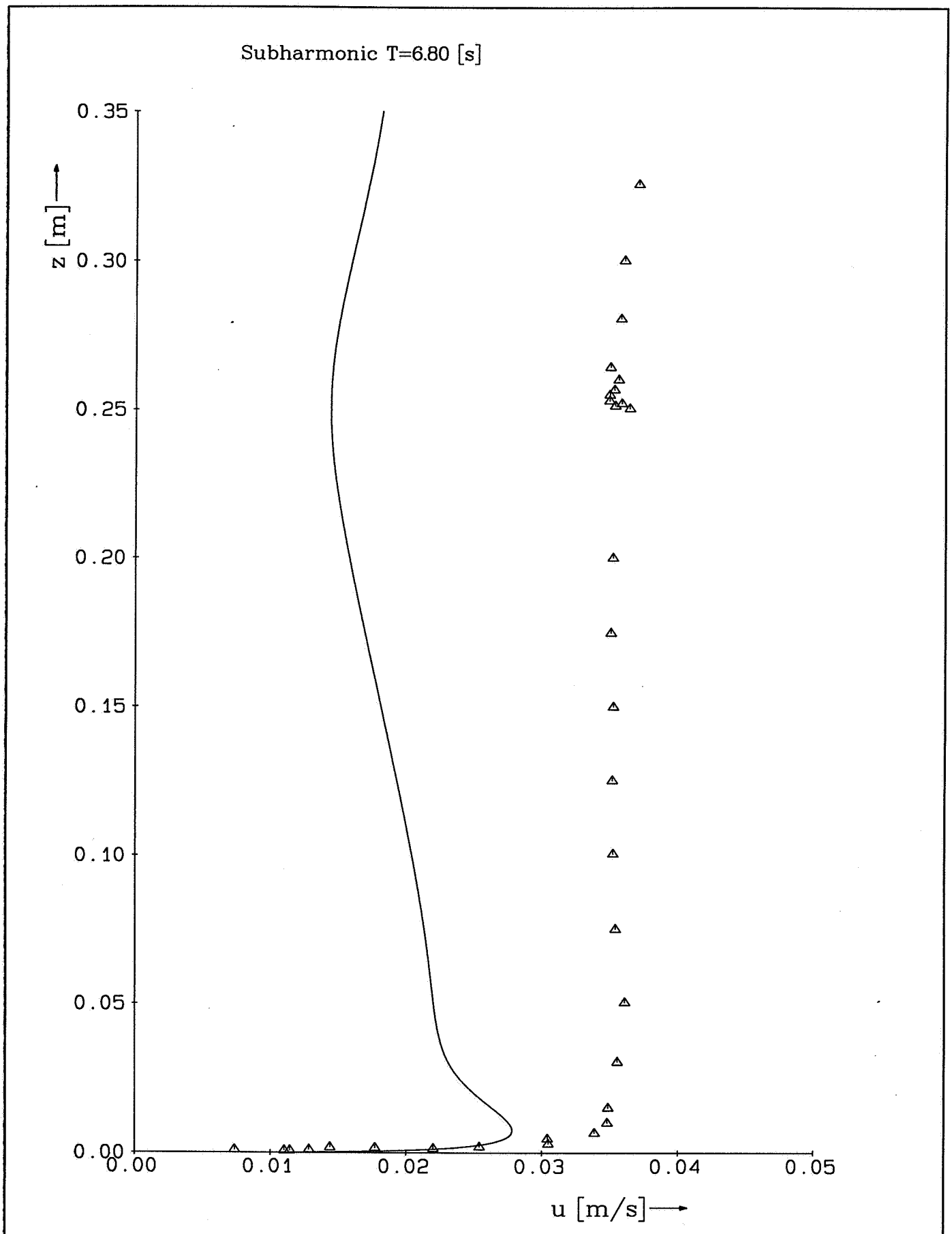

Wave–current with spectral DPM model (Uittenbogaard,1999). Simulation of biharmonic waves propagating with a mean current; compared to experiments of Klopman (1994).	500 non–equidistant points k–L turb. mod. with h.p. filter	
	d:\dpm\sedmoc\bih680.inv	
DELFT HYDRAULICS	Z–2733.41	Fig. 9

Mean velocity

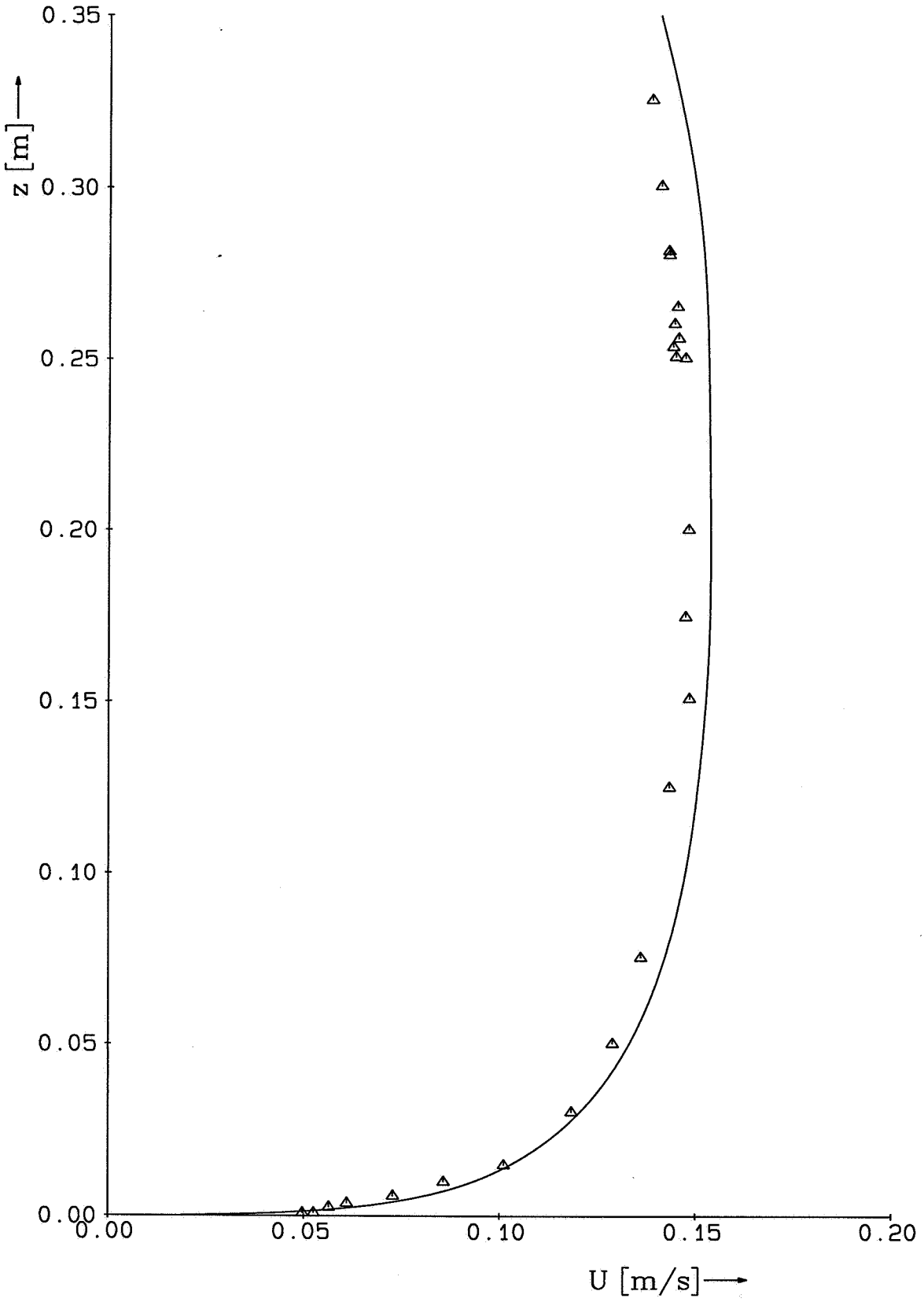

Wave–current with spectral DPM model (Uittenbogaard,1999).
Simulation of biharmonic waves propagating with a mean current; compared to experiments of Klopman (1994).

500 non–equidistant points
k–L turb. mod. with h.p. filter

d:\dpm\sedmoc\bihav.inv

DELFT HYDRAULICS

Z–2733.41

Fig. 9b

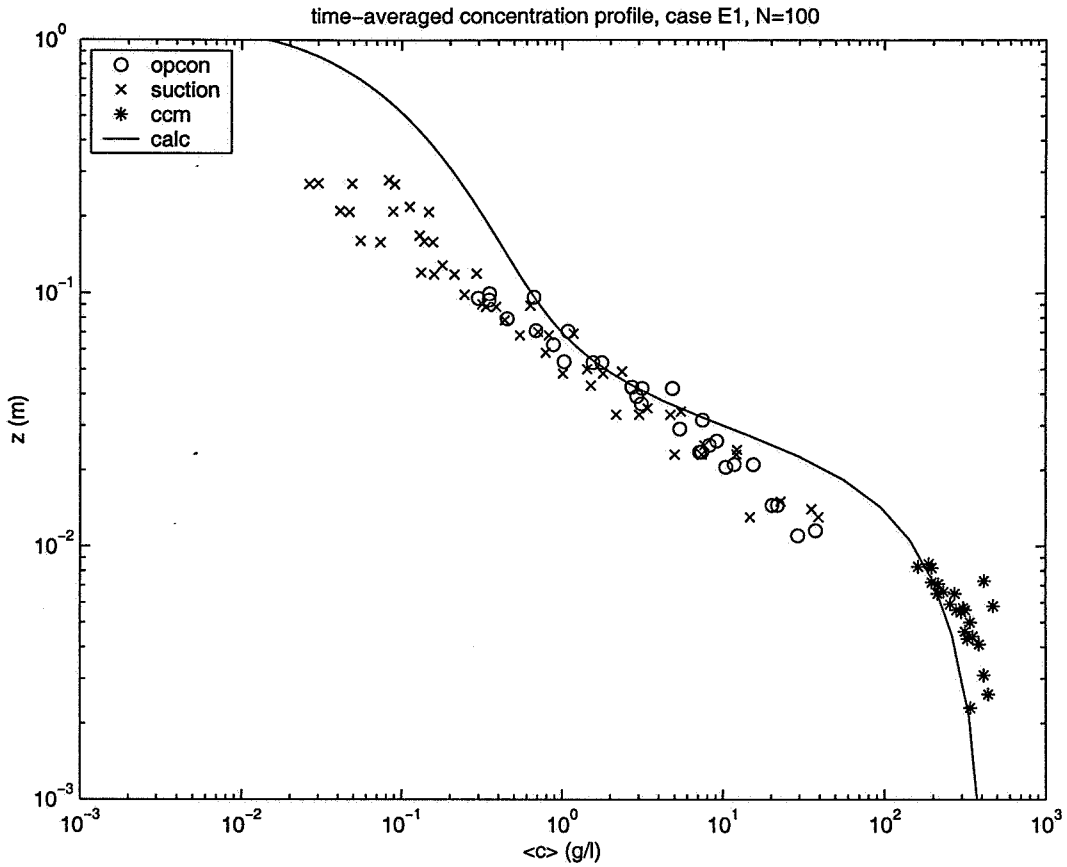

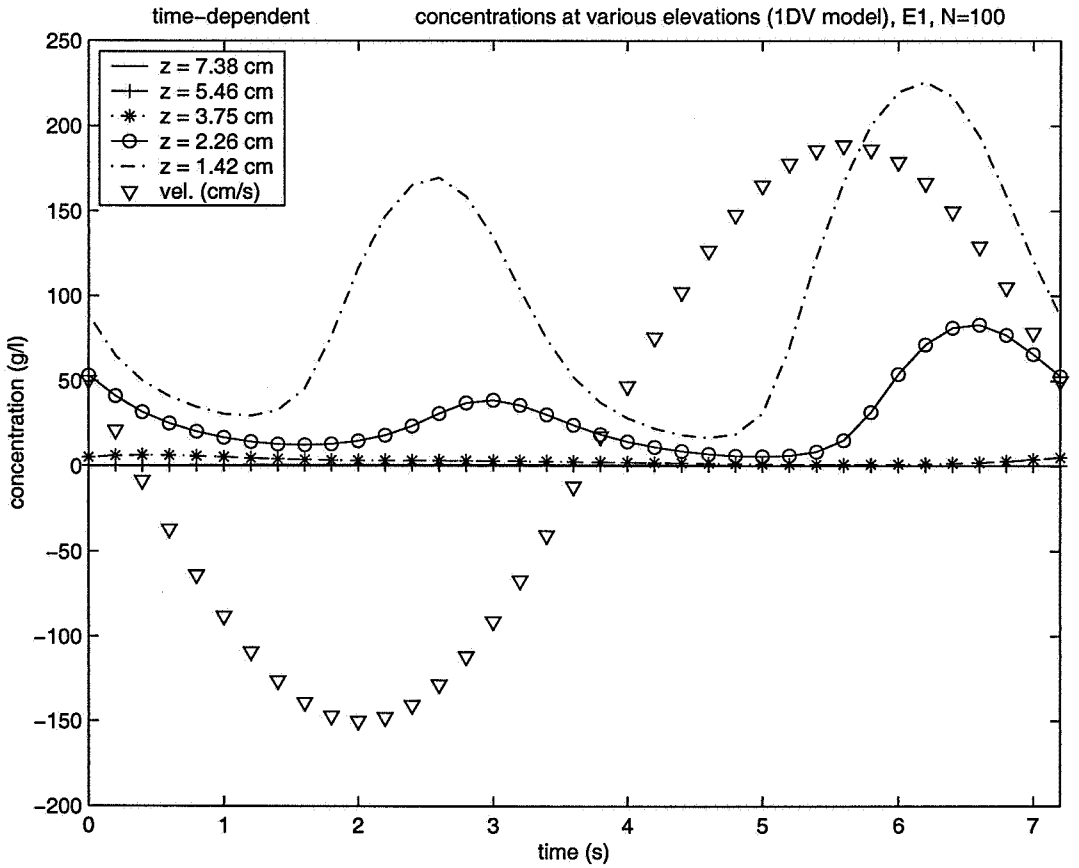

Fig. 10: Time-averaged concentration profile; case E1.
Fig. 11: Time-dependent concentrations at various elevations.

WL|DELFT HYDRAULICS	Z 2733.41	FIG. 10-11

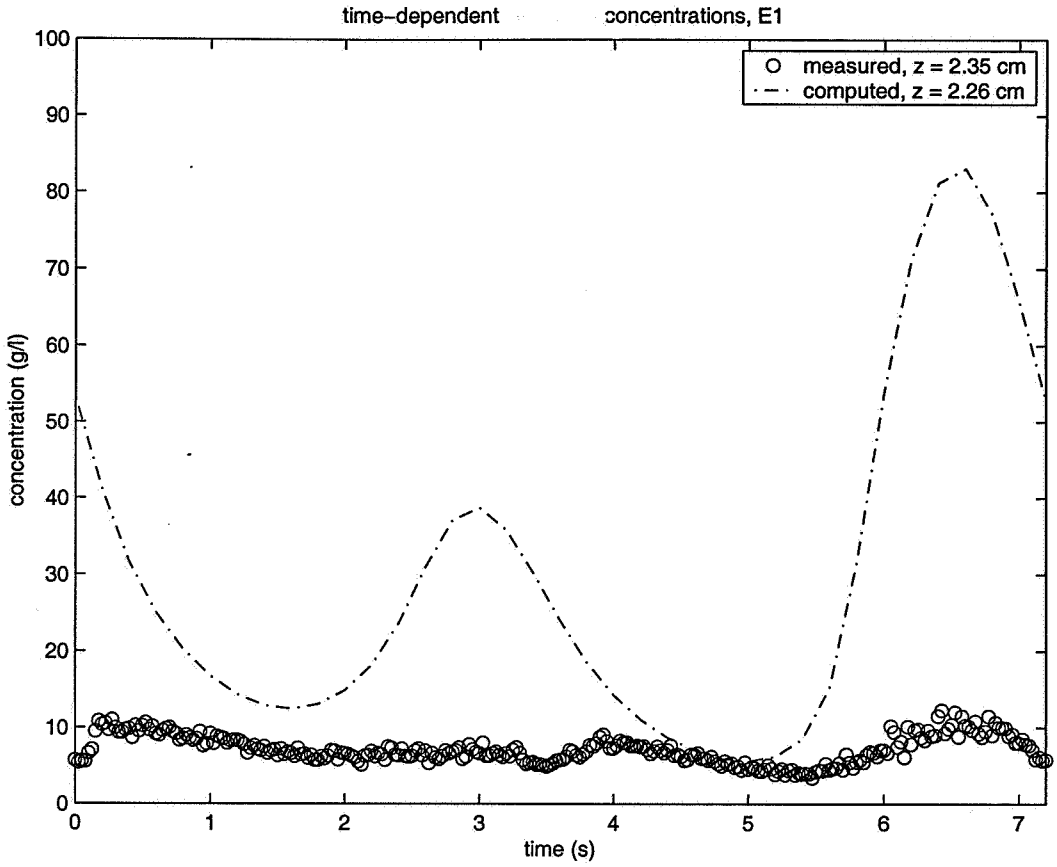

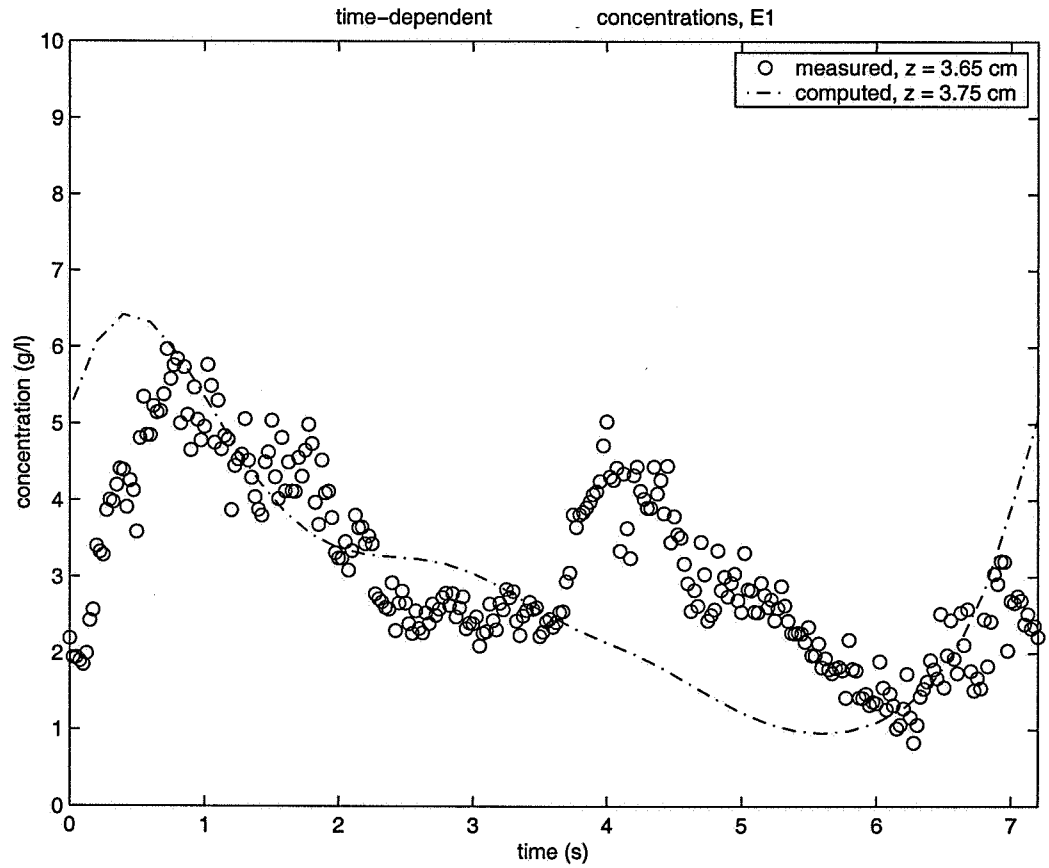

Fig. 12: Time-dependent concentrations, z = 2.3 cm case E1
Fig. 13: Time-dependent concentrations, z = 3.7 cm case E1

WL|DELFT HYDRAULICS	Z 2733.41	FIG. 12-13

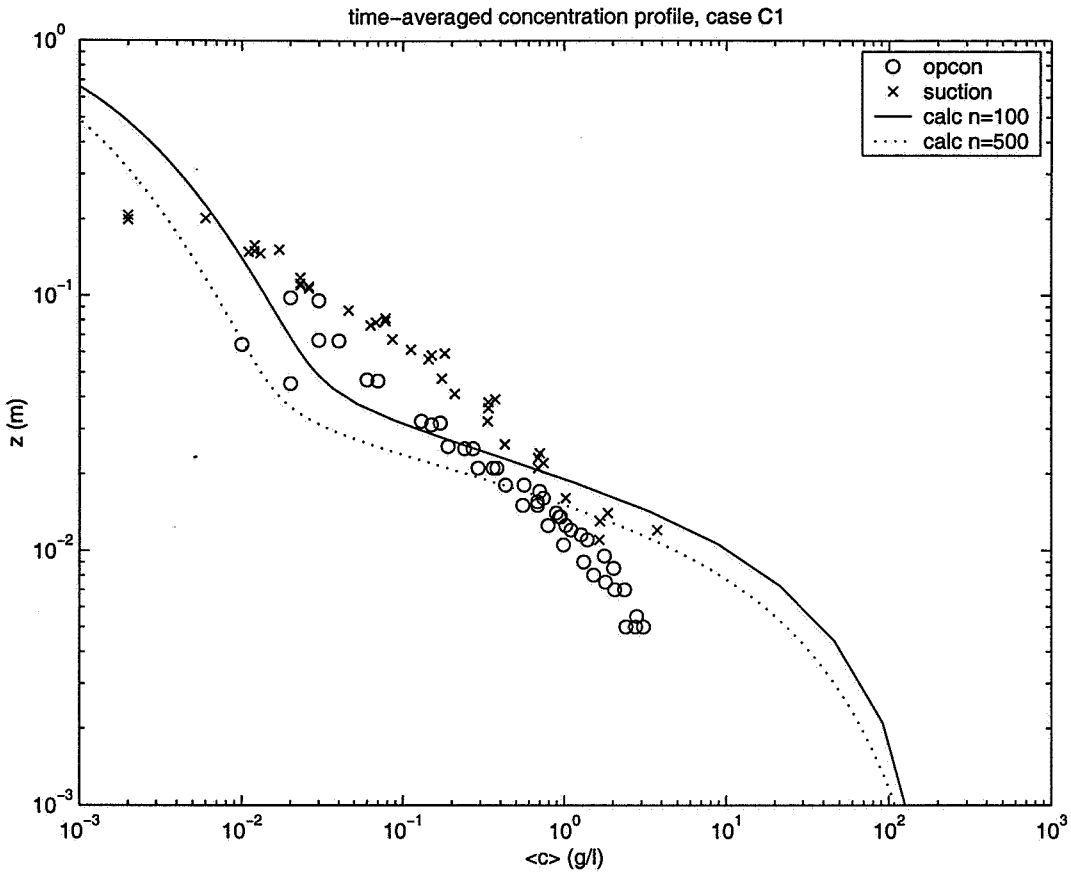

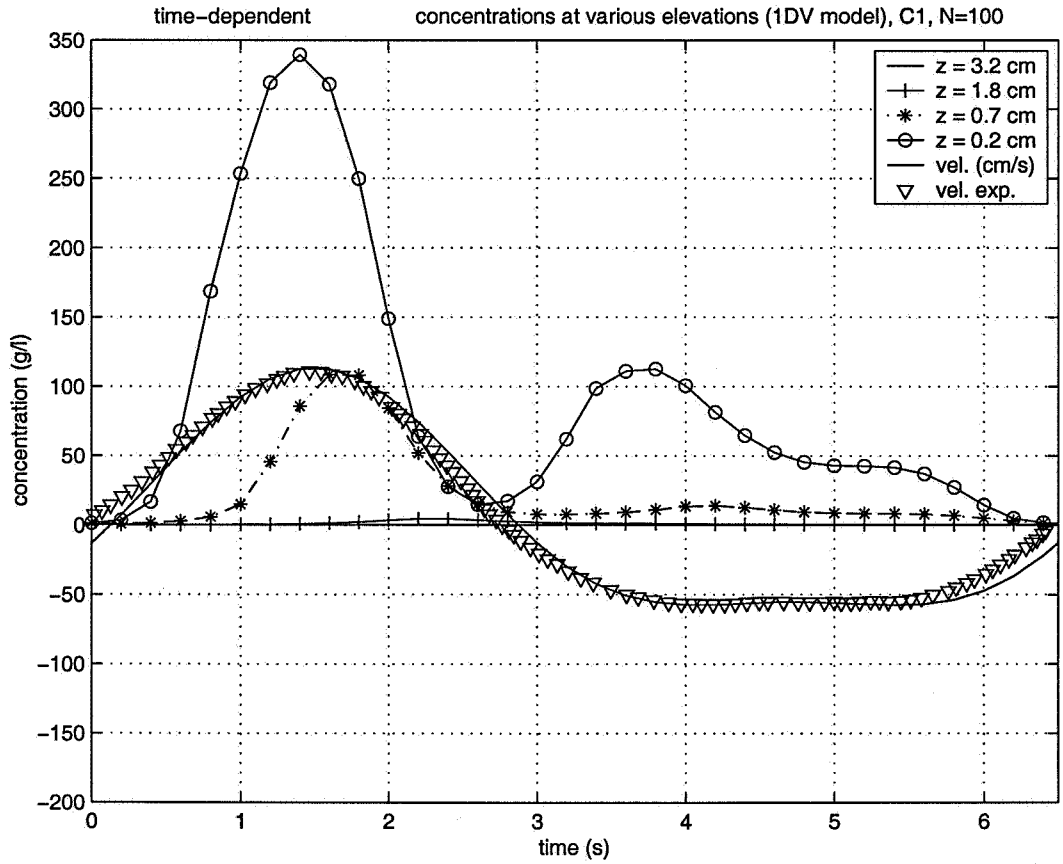

Fig. 14: Time-averaged concentration profile, case C1
Fig. 15: Time-dependent concentrations at various elevations.

WL|DELFT HYDRAULICS	Z 2733.41	FIG 14-15

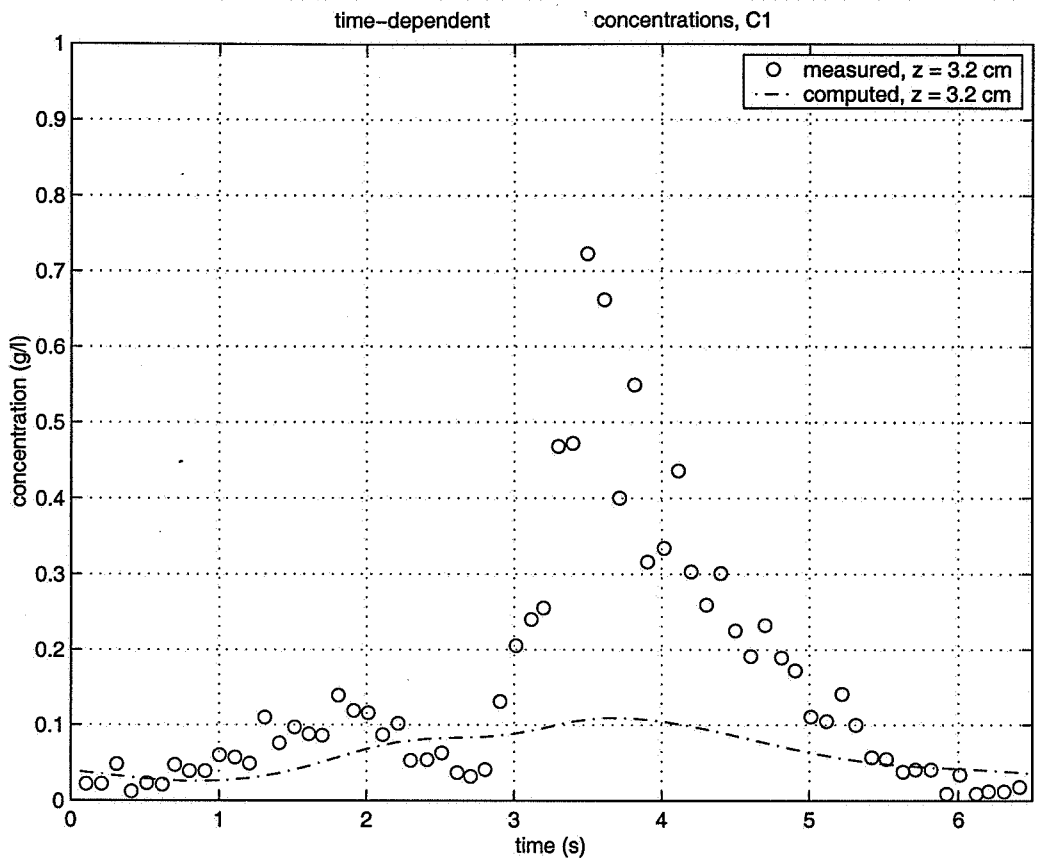

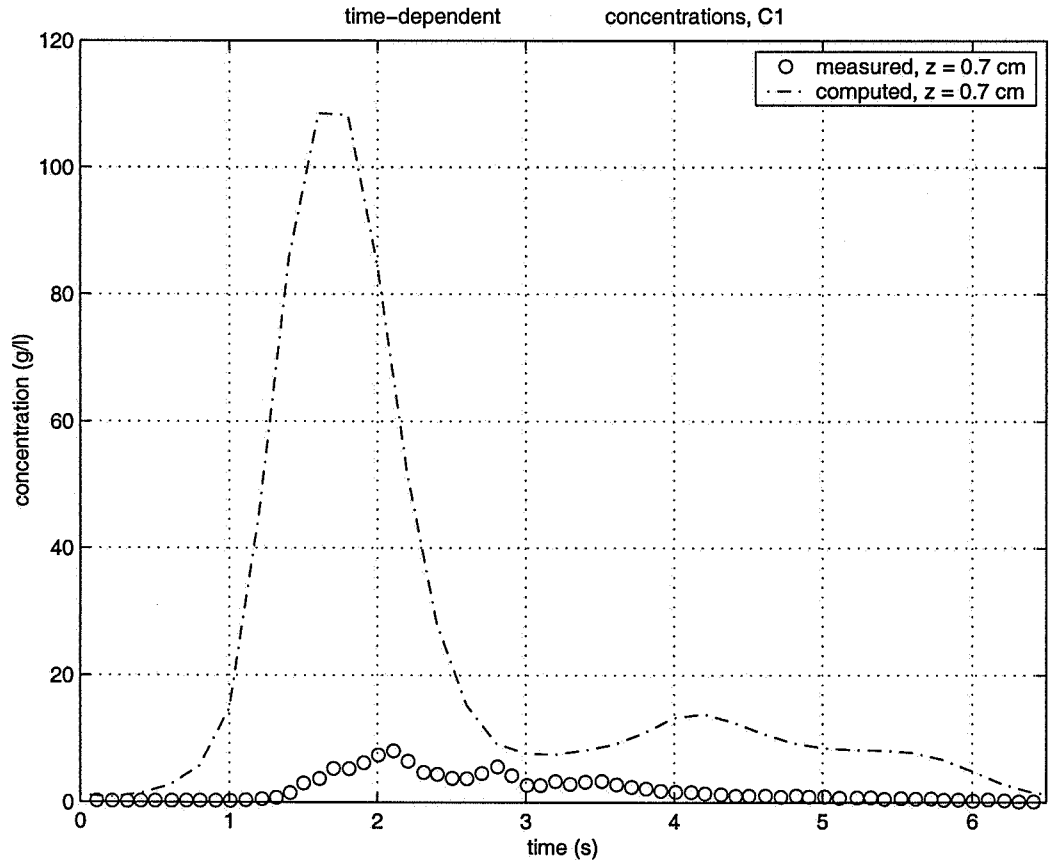

Fig. 16: Time-dependent concentration, z=3.2 cm, case C1
Fig. 17: Time-dependent concentration, z=0.7 cm, case C1

WL|DELFT HYDRAULICS	Z 2733.41	FIG. 16-17

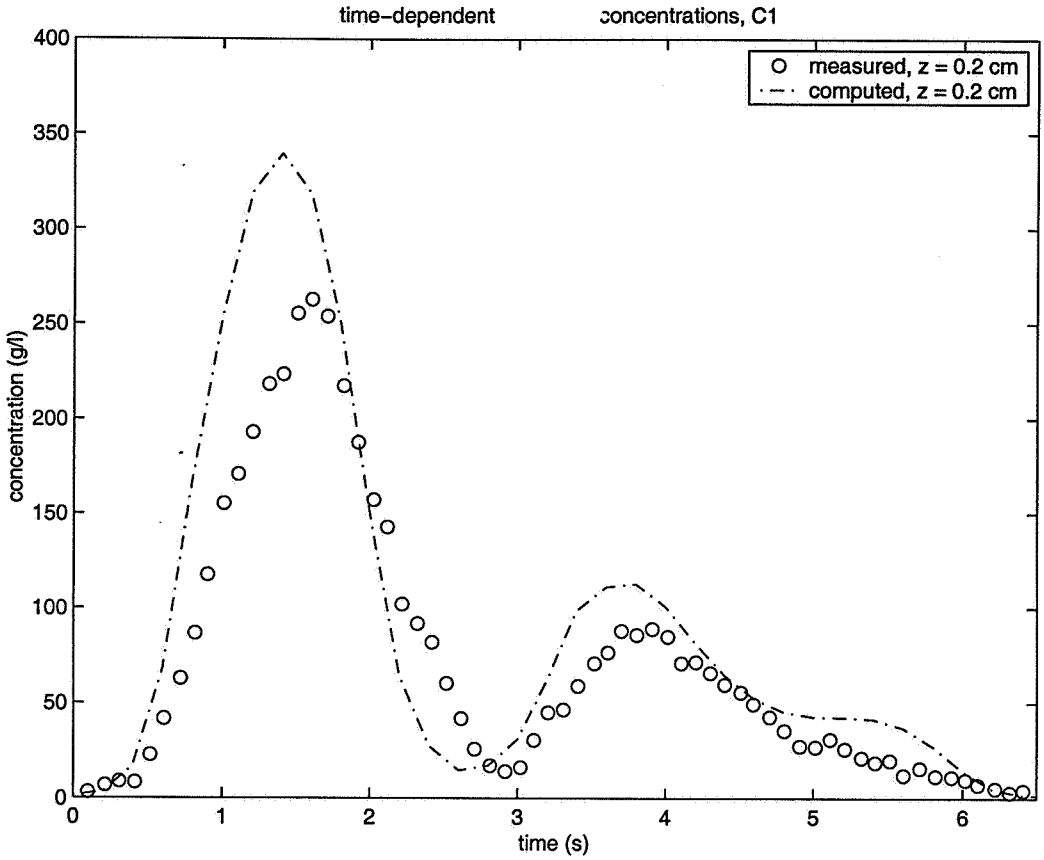

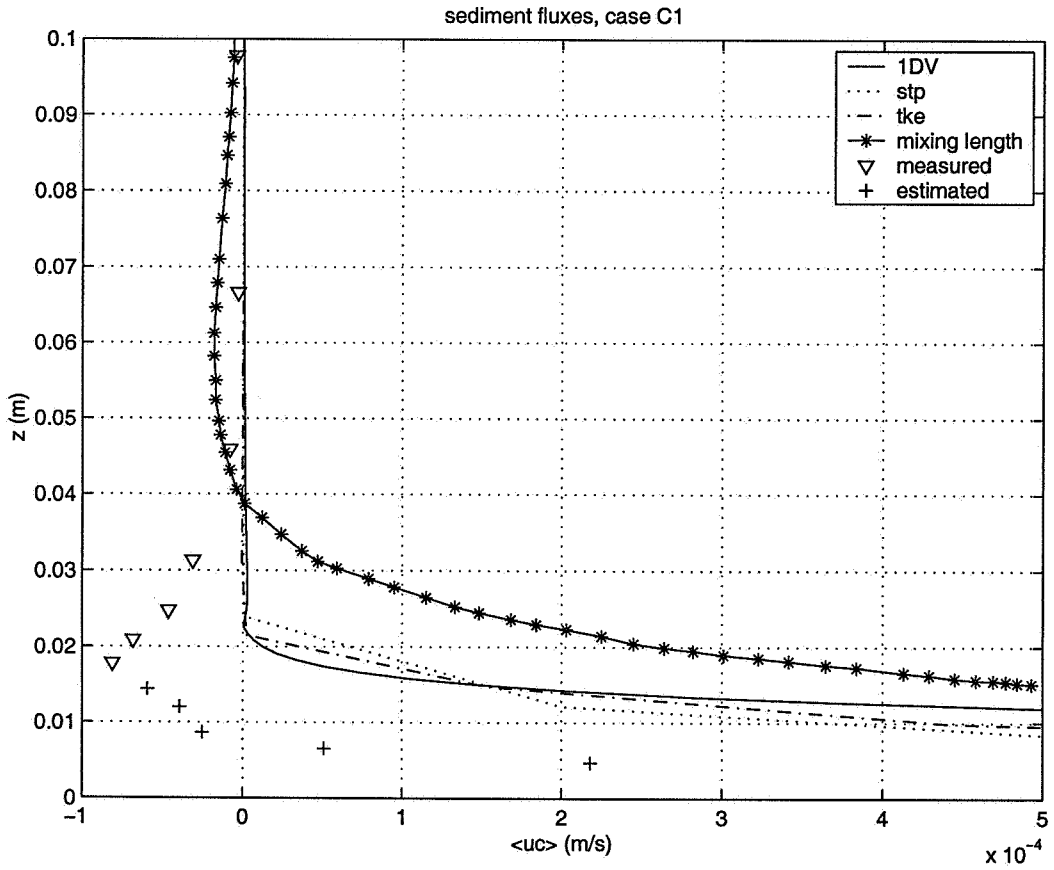

Fig. 18: Time-dependent concentration, z=0.c cm, case C1
Fig. 19: Sediment fluxes, case C1

WL|DELFT HYDRAULICS	Z 2733.41	FIG. 18-19

WL | delft hydraulics

Rotterdamseweg 185
postbus 177
2600 MH Delft
telefoon 015 285 85 85
telefax 015 285 85 82
e-mail info@wldelft.nl
internet www.wldelft.nl

Rotterdamseweg 185
p.o. box 177
2600 MH Delft
The Netherlands
telephone +31 15 285 85 85
telefax +31 15 285 85 82
e-mail info@wldelft.nl
internet www.wldelft.nl